A Measurement of the Top Quark Mass in the Dilepton Decay Channel at CDF II

by

Bodhitha A. Jayatilaka

A dissertation submitted in partial fulfillment
of the requirements for the degree of
Doctor of Philosophy
(Physics)
in The University of Michigan
2006

Doctoral Committee:

    Associate Professor David W. Gerdes, Chair
    Professor Mario L. Mateo
    Professor Timothy A. McKay
    Professor Jianming Qian
    Associate Professor James T. Liu

DEDICATION

To *Amma* and *Thaththa*.

ACKNOWLEDGEMENTS

There are many people who helped make this work possible and who I am honored to have worked with and know.

My advisor Dave Gerdes, who proposed such an interesting research topic and who stood by me in difficult circumstances. Monica Tecchio, who was never hesitant to share with me her vast expanse of knowledge. I've also been lucky to work with our collaborators from Penn who are some of the smartest and most talented physicists I know. Daniel Whiteson, who drove this analysis effort from day one and was always willing to offer advice, even if not about physics. Andrew Kovalev, who laid so much groundwork and led by example with his mathematical rigor. And Brig Williams for advice and invaluable words of encouragement.

Many people help make the Michigan CDF group feel more like family than anything else. The faculty: Dan Amidei, who not only ran a tight ship, but also was always there to share advice and his enthusiasm for physics; and Myron Campbell, who showed great trust in giving me the opportunity to get my feet wet in the electronics shop. My former housemates: Kathy Copic, Clark Cully, Nate Goldschmidt and Mitch Soderberg, who helped make living on-site bearable. And everyone else in the group during my time with it who offered advice, assistance and camaraderie: Ken Bloom, Claudio Ferretti, Stephen Miller, Fred Niell, Tom Schwarz, Tom Wright and Alexei Varganov.

The top group and top mass group conveners at CDF helped bring this analysis, in

TABLE OF CONTENTS

LIST OF FIGURES

LIST OF TABLES

ABSTRACT

A Measurement of the Top Quark Mass in the Dilepton Decay Channel at CDF II

by
Bodhitha A. Jayatilaka

Chair: David W. Gerdes

The top quark, the most recently discovered quark, is the most massive known fundamental fermion. Precision measurements of its mass, a free parameter in the Standard Model of particle physics, can be used to constrain the mass of the Higgs Boson. In addition, deviations in the mass as measured in different channels can provide possible evidence for new physics. We describe a measurement of the top quark mass in the decay channel with two charged leptons, known as the dilepton channel, using data collected by the CDF II detector from $p\bar{p}$ collisions with $\sqrt{s} = 1.96$ TeV at the Fermilab Tevatron. The likelihood in top mass is calculated for each event by convolving the leading order matrix element describing $q\bar{q} \rightarrow t\bar{t} \rightarrow b\ell\nu_\ell\bar{b}\ell'\nu_{\ell'}$ with detector resolution functions. The presence of background events in the data sample is modeled using similar calculations involving the matrix elements for major background processes. In a data sample with integrated luminosity of 1.0 fb^{-1}, we observe 78 candidate events and measure $M_t = 164.5 \pm 3.9(\text{stat.}) \pm 3.9(\text{syst.})$ GeV/c^2, the most precise measurement of the top quark mass in this channel to date.

CHAPTER 1

Introduction

At the heart of the field of particle physics lies the pursuit of studying the smallest elements of the universe. Far from small, the energies required to study these smallest elements requires the construction of the some of the largest scientific apparatuses ever built by mankind. A similar dichotomy is associated with the top quark, the focus of the research described in this dissertation. The top quark is the most massive of known fundamental particles. It is more massive than a gold nucleus, and nearly 200 times more massive than the protons and neutrons (themselves composite particles) that make up the gold nucleus and the majority of the rest of the matter that we see every day. The top quark is the most recently discovered of the fundamental particles called quarks and its measured properties hint strongly to clues about the nature of yet undiscovered physics, such as the Higgs boson. A brief introduction to the standard model and to top quark physics is presented in Chapter 2.

The study the top quark has been one of the primary focuses of the CDF and DØ collaborations at Fermilab. The Tevatron accelerator and CDF detector are described in Chapter 3. At the time of this writing, CDF and DØ remain the only experiments capable of directly studying the top quark and have provided several precise measurements of the top quark mass.

This dissertation describes a measurement of the mass of the top quark in the top quark pair decay channel with the smallest branching fraction, the dilepton channel. The measurement described uses a statistically powerful technique, known as a "matrix-element method" for its usage of a leading-order matrix element to describe a likelihood. The method is described in Chapters 5–9. We applied this method to the dilepton channel for the first time in 2005 [1] using 340 pb^{-1} of data[1] collected at CDF; the resulting measurement has been published in Ref. [2]. Since then, we have applied it to successively larger datasets and made further refinements to the method. The method described here was applied to 1.0 fb^{-1} of CDF data yielding the single most precise measurement of the top quark mass in the dilepton channel to date. This result is described in Chapter 11.

---

[1]Integrated luminosity, a measured of accumulated data at collider detectors, is described in Chapter 3

CHAPTER 2

The Standard Model and Top Quark Physics

This chapter provides a brief overview of the standard model of particle physics and of top quark phenomenology.

2.1   The Standard Model

The standard model of particle physics describes all known fundamental particles and their interactions in the strong, electromagnetic and weak nuclear forces. The model itself is a combination of the theory of quantum chromodynamics (QCD) [3, 4] and the Glashow–Salam–Weinberg (GSW) theory of electroweak interactions [5, 6, 7]. The former describes the strong nuclear force and is represented by the $SU(3)_C$ gauge group, while the latter describes weak and electromagnetic forces and is represented by the $SU(2)_L \times U(1)_Y$ gauge group. Thus, the standard model is locally invariant under transformations of the group

$$G = SU(3)_C \times SU(2)_L \times U(1)_Y. \tag{2.1}$$

The standard model accounts for three generations of fundamental fermions (spin-$\frac{1}{2}$ particles). Each generation consists of a pair of leptons, whose interactions are mediated

by the electroweak forces,

$$\begin{pmatrix} e \\ \nu_e \end{pmatrix} \begin{pmatrix} \mu \\ \nu_\mu \end{pmatrix} \begin{pmatrix} \tau \\ \nu_\tau \end{pmatrix},$$

and a pair of quarks, whose interactions are mediated by electroweak and strong (QCD) forces,

$$\begin{pmatrix} u \\ d \end{pmatrix} \begin{pmatrix} c \\ s \end{pmatrix} \begin{pmatrix} t \\ b \end{pmatrix}.$$

The vast majority of stable matter we observe is made up of particles entirely in the first generation.[1] Bosons (spin-1 particles) mediate each of the forces described by the standard model: the photon (γ) for the electromagnetic force, the $W^\pm$ and Z^0 bosons for the weak force, and the gluon (g) for the strong force.

The standard model has been successful at describing interactions of the particles described above, all of which have been discovered experimentally). In addition, many of the predicted properties of these particles have been confirmed, some to a high degree of precision. However, in order for the symmetry described in Equation 2.1 to be exact, the fermions and the W and Z bosons would have to be massless. In order for the standard model to be compatible with the large observed masses of the W and Z bosons[2], spontaneous symmetry breaking must occur. This symmetry breaking would additionally be responsible for the mass hierarchy observed in the fermions. This Electroweak Symmetry Breaking (EWSB) is accomplished by the introduction of a scalar field known as the Higgs Field [9]. The existence of a massive boson, the Higgs boson, would be associated with the Higgs field.

The existence of the Higgs boson has yet to be confirmed experimentally, and remains one of the most important tasks for the field of high energy physics. Direct searches for the

---

[1]Incidentally, cosmological studies have shown that this matter, known as "baryonic matter" (since by mass it is mostly made up of protons and neutrons which are bound states of three quarks, or "baryons") comprises less than 5% of known Universe.

[2]$M_W = 80.425 \pm 0.038$ GeV/c^2 and $M_Z = 91.1876 \pm 0.0021$ GeV/c^2[8]
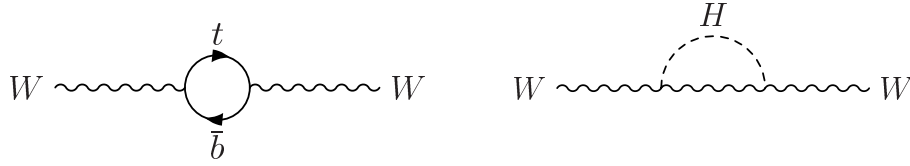
Figure 2.1: Corrections to the W boson observed mass via loop diagrams. *Left*: A fermion loop involving top and bottom quarks. The large top quark mass dominates this correction, which is proportional to M_t^2. *Right*: A Higgs boson loop which contributes a correction proportional to $\ln M_H$.

standard model Higgs boson at the CERN Large Electron Positron (LEP) collider have set a lower bound on its mass of $M_H > 114.4$ GeV/c^2 at the 95% confidence level [10]. In addition, indirect bounds on the mass of the Higgs boson can be set from precision measurements of the top quark and W boson masses [11], as these quantities are sensitive to $\ln M_H$ through radiative corrections as shown in Figure 2.1. Using measurements of the top quark mass made up to March 2006 and precision electroweak measurements made at LEP (as shown in Figure 2.2), the constraints on the standard model Higgs boson are

$$M_H = 89^{+42}_{-30} \text{ GeV}/c^2 \tag{2.2}$$

$$M_H < 175 \text{ GeV}/c^2 \text{ at 95\% CL} \tag{2.3}$$

Obtaining a more precise estimate of where a standard model Higgs boson mass should lie is one of several reasons to pursue a precision measurement of the top quark mass at the Tevatron.

2.2 The Top Quark

Following the discovery of the bottom (b) quark in 1977, the existence of its doublet partner, the top (t) quark, could be inferred for several reasons. For one, the renormalizability of the standard model requires that the sum of electric charges of all left-handed fermions must equal zero. This condition is only satisfied with the existence of a sixth quark with an electric charge of $+2/3$. In addition, precision measurements involving the
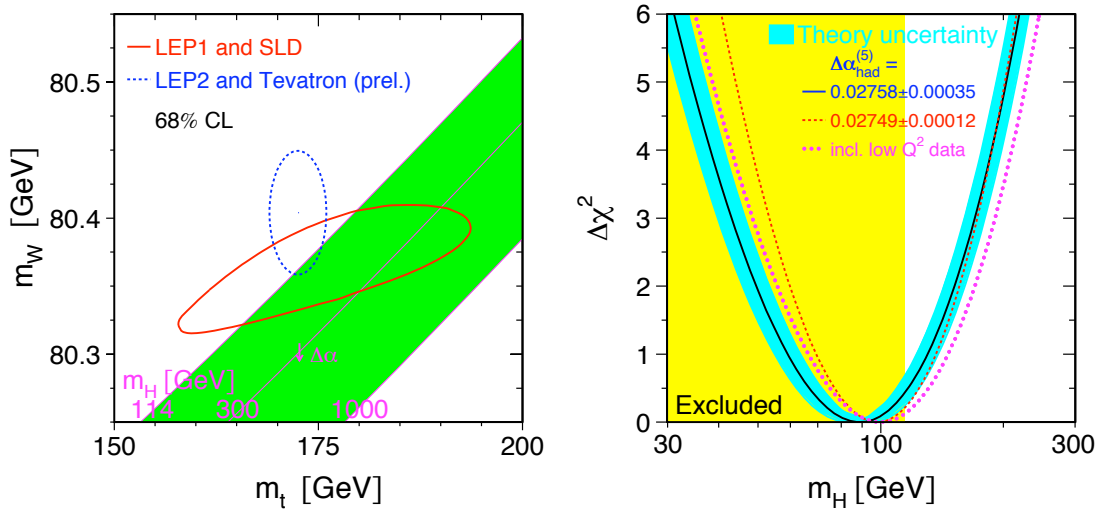
Figure 2.2: *Left*: Constraints on the standard model Higgs boson mass as a function of top quark mass and W boson mass as of March 2006. The red curve shows the 68% CL constraint obtained from studies at the Z pole made at SLD and LEP. The dashed blue curve shows the 68% CL constraint obtained from direct measurements of M_W and M_t made at LEP and the Tevatron. *Right*: The $\Delta\chi^2$ (black curve) to a global fit of standard model parameters to a standard model Higgs boson mass. The yellow band shows the region excluded by direct searches at LEP. Courtesy of the LEP Electroweak Working Group [11].

isospin of the b-quark can be made at e^+e^- colliders which can be used to exclude the possibility of the b quark being a member of a singlet [12]. The discovery of the top quark was accomplished in 1995 at the CDF and DØ experiments[13, 14]. By the end of the 1992-1996 collider run (Run I), combined measurements from both experiments' datasets of $\sim$100 pb^{-1} provided a measurement of the top quark mass of $M_t = 178 \pm 4.3$ GeV/c^2.

2.2.1 Top Quark Production

In $p\bar{p}$ collisions, top quarks are predominantly produced in pair form via the strong force. While single top quark production via the electroweak force is predicted in the standard model, it has not been observed with statistical significance. At the current Tevatron center-of-mass energy of $\sqrt{s} = 1.96$ TeV, top-antitop pair ($t\bar{t}$) production occurs via the channel $q\bar{q} \rightarrow t\bar{t}$ approximately 85% of the time while occurring via the channel
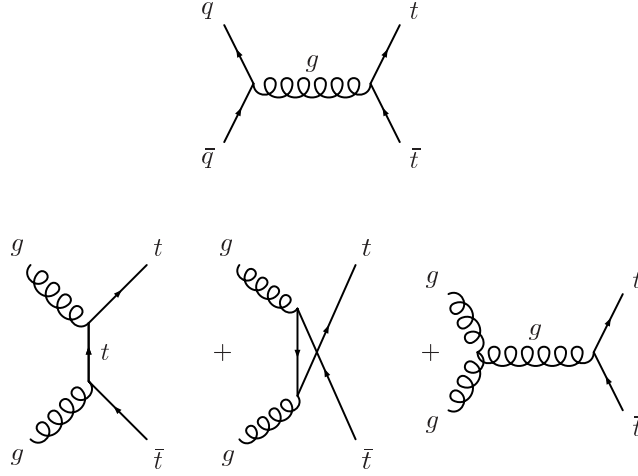
Figure 2.3: *Top*: Leading-order production diagram for $q\bar{q} \rightarrow t\bar{t}$. *Bottom*: Leading-order production diagrams for $gg \rightarrow t\bar{t}$.

$gg \rightarrow t\bar{t}$ the remaining 15% of the time [15]. The leading order diagrams for these production channels are shown in Figure 2.3.

The theoretical prediction of the $t\bar{t}$ production cross-section at Next-to-Leading Order (NLO) is $\sigma_{t\bar{t}}^{NLO} = 6.7^{+0.7}_{-0.9}$ pb for $M_t = 175$ GeV/c^2 [15]. Figure 2.4 shows the NLO calculation of $\sigma_{t\bar{t}}$ for $p\bar{p}$ collisions at $\sqrt{s} = 1.96$ TeV as a function M_t. A combination of current measurements of $\sigma_{t\bar{t}}$ made at CDF during the current collider run, Run II ($\sqrt{s}$=1.96 TeV) [16] are also shown, and is in good agreement with the predicted value.

2.2.2   Top Quark Decay

Nearly 100% of top quarks are expected to decay via the channel $t \rightarrow Wb$. Other decay channels are permitted in the standard model, but are heavily suppressed by factors of $|V_{ts}|^2/|V_{tb}|^2 \approx 10^{-3}$ and $|V_{td}|^2/|V_{tb}|^2 \approx 5 \times 10^{-4}$, where V_{ij} is the Cabibbo-Kobayashi-Maskawa (CKM) weak–mixing matrix [17]. For the purposes of this analysis, we will assume that top quark decay occurs exclusively via the channel $t \rightarrow Wb$. The large mass of the top quark results in a very rapid decay with a mean lifetime of $\tau_t \sim 10^{-24}$ s. As this
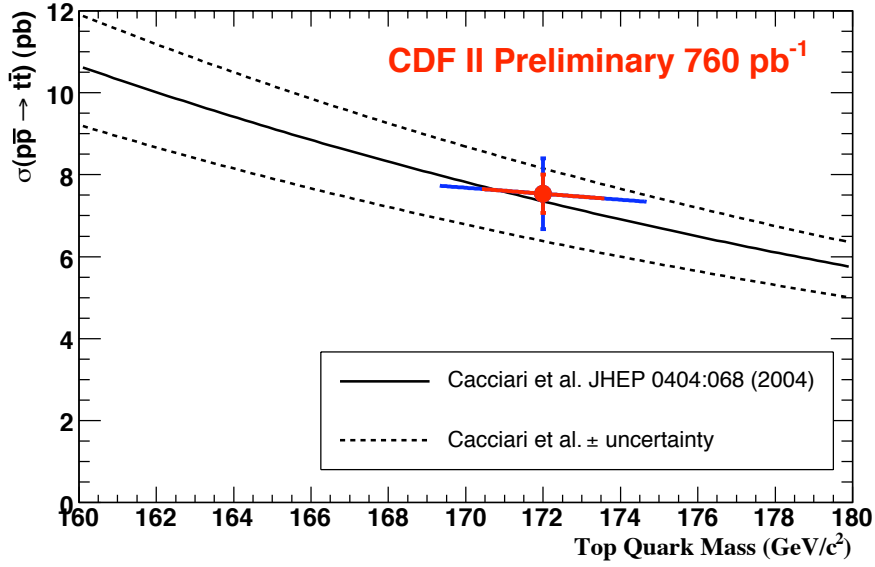
Figure 2.4: NLO calculations of $\sigma_{t\bar{t}}$ [15] for $p\bar{p}$ collisions at $\sqrt{s} = 1.96$ TeV as a function of M_t. Also shown are experimental measurements of $\sigma_{t\bar{t}}$ made at CDF using Run II [16] data.

is shorter than the timescale required for quarks to form bound states (or "hadronize"), the top quark essentially decays as a "free" quark. The b-quark resulting from the decay will then proceed to hadronize and manifest itself in the detector as a jet, or a collimated stream of hadrons (jets are described further in Chapter 4). The W boson will decay rapidly into either a pair of quarks or a charged lepton and a neutrino. Thus, for the case of a $t\bar{t}$ pair decay, we have six particles in the final state: two b-quarks and two decay products from each of the W bosons.

It is the decay mode of the W bosons that defines the decay channels of the $t\bar{t}$ system used in its experimental study. These decay channels are classified as:

- The *all-hadronic channel*, where both W bosons decay to quarks, resulting in a final state having an experimental signature of six jets. This decay mode carries the largest branching ratio, of 46%, but suffers from the largest amount of irreducible background due to its high jet count.

- The *lepton+jets channel*, where one W decays to a lepton and the other to quarks, resulting in an experimental signature of a high momentum lepton, four jets, and missing transverse energy[3] associated with the neutrino. Due to the difficulty of identifying τ leptons at a hadron collider, only leptonic states with an electron or muon in the final state are considered. While the multi-jet background is still large in this channel, it is far less than in the all-hadronic channel. This channel carries a branching ratio of 30%.

- The *dilepton channel*, where both W bosons decay to leptons, resulting in an experimental signature of two high momentum leptons, two jets, and large missing transverse energy associated with two neutrinos. As with the lepton+jets channel, only leptonic states with an electron or muon on the final state are considered. A diagram showing this decay channel is in Figure 2.5. This channel carries a branching ratio of 5%. The analysis described in this dissertation is performed in the dilepton channel.

The remaining 20% of $t\bar{t}$ decays involve the production of a τ lepton that does not decay to an e or μ. While measurements in this so-called "$\tau + X$" channel are possible, they does not afford nearly the same precision that any of the other three channels do.

2.3   Top Quark Mass in the Dilepton Channel

Traditionally, the lepton+jets channel has offered the most precise measurements of the top quark mass due to its higher statistics than the dilepton channel and lower background than the all-hadronic channel. However, the dilepton channel, while offering the least amount of statistics, has some unique advantages. Since it has the least amount of jets, the dilepton channel, in principle, offers the least reliance on the jet energy scale (the

---

[3]Assuming the transverse energy of the initial system is zero, an imbalance in final state transverse energy, or "missing transverse energy" ($\not{E}_T$) can be attributed to undetected objects, such as neutrinos. $\not{E}_T$ is described further in Chapter 4.
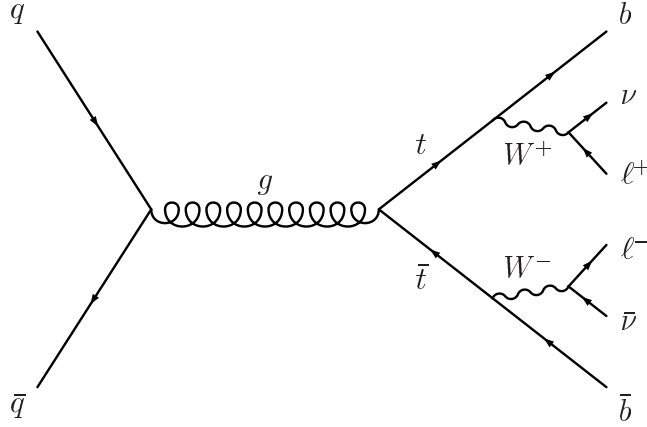
Figure 2.5: Decay of $t\bar{t}$ in the dilepton channel.

estimation of underlying parton energy from measured jet energy– described further in Chapter 4). The jet energy scale is the single largest source of systematic uncertainty in most top mass measurements. The lower number of jets also results in fewer possible jet-parton combinations in each event. In addition, the dilepton channel has the highest sample purity without the usage of explicit b-jet identification.[4]

The difficulty in measuring the top quark mass in the dilepton channel results arises from the presence of two neutrinos in each event. As neutrinos cannot be directly detected in our detector, their presence must be inferred from $\not{E}_T$ in an event. As there is only one $\not{E}_T$ measurement per event, the amount of energy imparted from each individual neutrino can never be known in dilepton events. Therefore, the kinematic final state of the $t\bar{t}$ cannot be fully reconstructed using measured quantities in dilepton events.

Despite the lower statistical precision of top quark mass measurements in the dilepton channel, these measurements are still able to provide significant contributions to the

---

[4]B-jet identification methods such as secondary vertex tagging (the measurement of displaced secondary vertices in an event resulting from the decay of a b-jet) greatly reduce the amount of background in all $t\bar{t}$ channels at the cost of approximately 50% of the signal statistics. Such methods are used in nearly all precision measurements of the top quark mass in the lepton+jets and all hadronic channels.

overall precision of our knowledge of the top quark mass. At the time of this writing, the most recent combination of measurements of the top quark mass utilizes measurements made with Run I data and up to 750 pb^{-1} of Run II data from both CDF and DØ [18]. This average and the individual measurements contributing to it are shown in Figure 2.6. The single most precise measurement in the dilepton channel used for this combination, a prior iteration of the analysis described in this dissertation, provides a weight of 11%.

A striking feature of Figure 2.6 is the relatively low value that precision measurements of the top quark mass in the dilepton channel have relative to the most precise measurements in the lepton+jets channel. While these deviations are certainly not inconsistent with statistical fluctuations, a measurement of the mass of the top quark, assuming the standard model, should yield the same value in all decay channels. A significant deviation between decay channels could indicate the presence of non-standard model contributions in one or more of the decay channels.
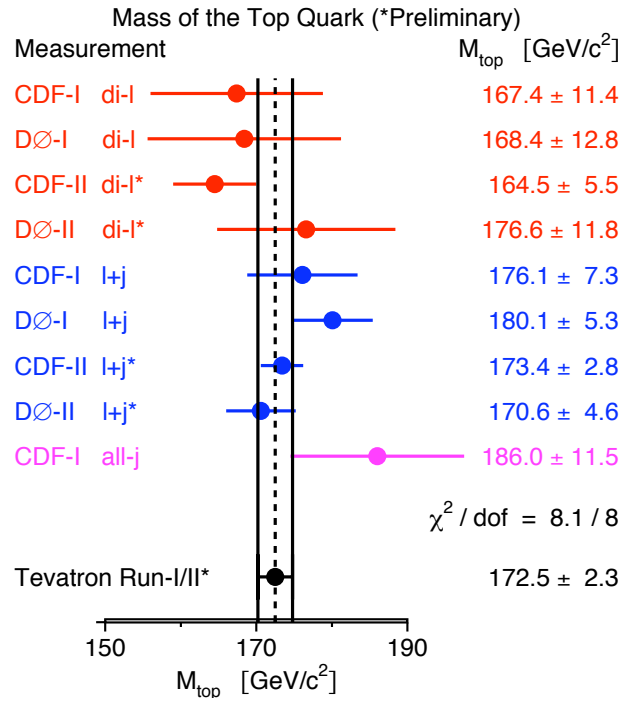
Figure 2.6: World average of the top quark mass along with the individual measurements used to calculate it as of March 2006 [18].

CHAPTER 3

Experimental Apparatus

The large mass of the top quark makes it necessary to rely on high-energy collisions to produce them. At the time of this writing, the Tevatron synchrotron at the Fermi National Accelerator Laboratory (Fermilab) in Batavia, Illinois, is the only facility with sufficient energy for direct top quark production. Once produced, a device capable of observing the resulting events is necessary. The CDF II detector is one of the two detectors built on the Tevatron capable of performing this task. In this chapter, both the collider and the detector are described.

3.1 The Collider

The collider complex at Fermilab consists of a chain of eight accelerators that are necessary to take protons and not only accelerate them to a high energy, but also produce antiprotons, accelerate them to the same energy, and collide them with protons at a center-of-mass energy of $\sqrt{s} = 1.96$ TeV. A schematic view of the Fermilab accelerator complex is shown in Figure 3.1.

3.1.1 The Proton Source and Pre-Acceleration

The protons that are used in collisions and to produce antiprotons all begin in a small bottle of hydrogen gas. Hydrogen atoms drawn from this bottle are ionized to form H^-
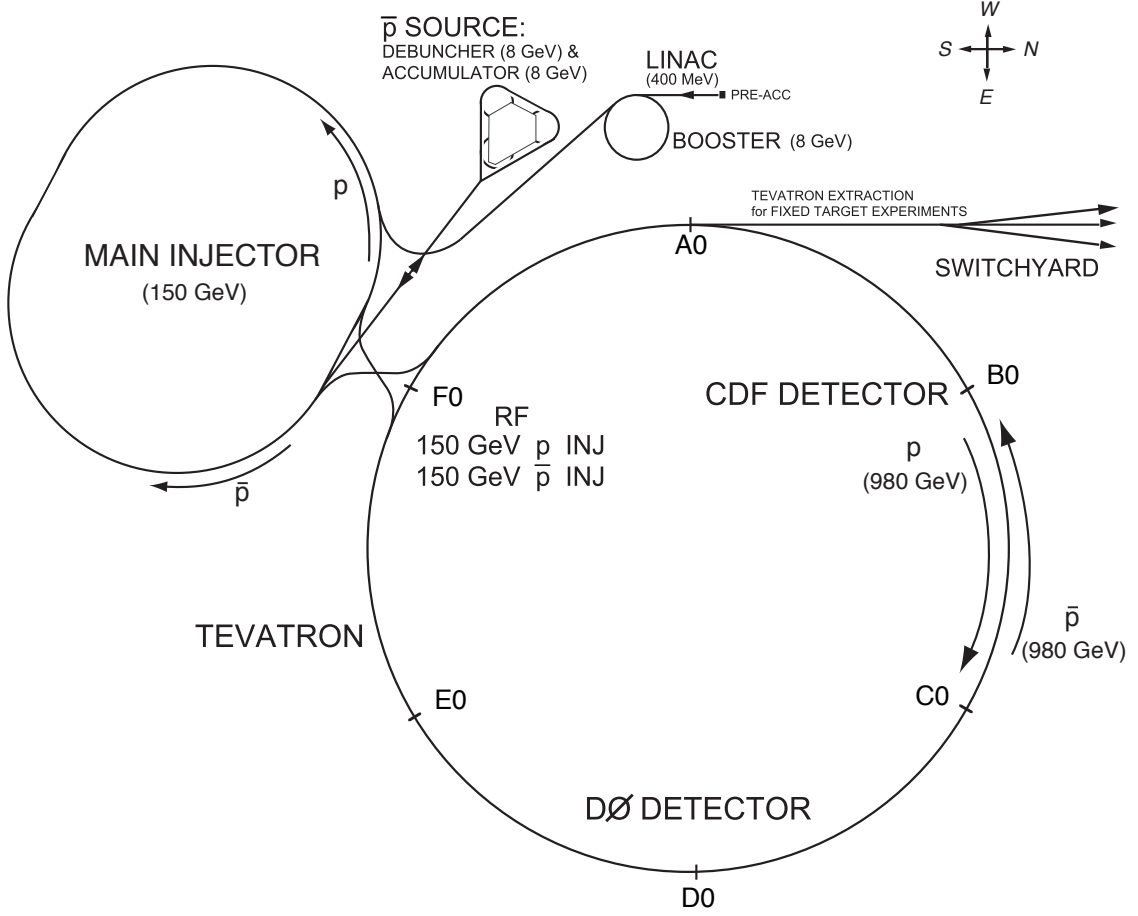
Figure 3.1: A schematic view of the Fermilab accelerator complex. Figure courtesy of Fermilab Accelerator Division.

ions. The H$^-$ ions are accelerated from rest to an energy of 750 keV by a Cockroft-Walton device– an electrostatic generator that applies an electric field to the ions.

The H$^-$ ions are then injected into the Linac, a linear RF accelerator, which further accelerates them to an energy of 400 MeV. At this point, the electrons are removed from the H$^-$ ions, leaving behind bare protons.

The protons then enter the Booster, a synchrotron with a circumference of 474 m. The Booster utilizes magnets to bend the protons along a circular path while RF cavities accelerate them to an energy of 8 GeV.

At this point, the protons enter the Main Injector, a synchrotron 3 km in circumference.

The Main Injector can accelerate the protons either to 150 GeV for injection into the Tevatron, or to 120 GeV for usage in antiproton production. The Main Injector can also stack antiprotons produced in the antiproton source and accelerate them to 150 GeV prior to usage in the Tevatron.

3.1.2 The Antiproton Source

One of the most technically daunting tasks in the collider operations at Fermilab is the production and storage of antiprotons. Because of its difficulty, the production of antiprotons remains the limiting factor in the luminosity of colliding beams at the Tevatron. The antiproton source at Fermilab consists of a target for production and three accelerators used to cool and store: the Debuncher, the Accumulator and the Recycler.

Antiprotons are produced by striking 120 GeV protons from the Main Injector upon a nickel target. These collisions yield a shower of particles from which antiprotons are separated using magnetic spectroscopy.[1] Approximately 100,000 protons are needed to successfully produce and store one antiproton. The resulting antiprotons have an average energy of 8 GeV.

The antiprotons produced at the target are then sent to the Debuncher, a triangular synchrotron with a mean radius of 90 m. The beam of antiprotons sent into the Debuncher has a large spread of momenta. The Debuncher is tasked with reducing this spread in momenta, forming a continuous beam.

The antiprotons are sent to the Accumulator, another triangular synchrotron that shares a tunnel with the Debuncher. Here, the antiprotons are stored, or "stacked", as more are produced. In addition, a process known as stochastic cooling is used to further reduce the spread in momenta of the antiprotons. When a sufficient number of antiprotons

---

[1]The particles are subject to a magnetic field causing particles of different mass and charge to take paths of different radii. This allows antiprotons to be separated out.

for colliding beam operations have been stacked at the Accumulator, they can then be sent to the Main Injector for further acceleration.

The Recycler

The Recycler is a 3 km synchrotron housed in the same tunnel as the Main Injector. It utilizes permanent magnets, making it the largest particle accelerator ever built that solely uses permanent magnets. The original design of the Recycler called for it to store antiprotons that were unused in a colliding physics run in the Tevatron and use them in a future colliding run. In practice, this mode of operation proved difficult to implement practically and efficiently. However, since 2004, the Recycler has been used to store additional antiprotons prior to a colliding physics run. Antiprotons are now stored in both the Accumulator and Recycler for nearly all colliding beam runs, greatly increasing the amount of available antiprotons for collisions in the Tevatron.

Electron Cooling

Electron cooling is a technique which uses a beam of electrons run alongside a beam of antiprotons to reduce the longitudinal momentum of the antiprotons. While the method was first proposed in 1966 and has been utilized for low-energy beams, its implementation at Fermilab in 2005 is the first successful application of electron cooling to a relativistic beam. The electron cooling system in use utilizes a 4.3 MeV beam of electrons that is run alongside a 20 m length of the Recycler. This system has been in operation since late 2005 and is expected to help increase luminosities for the colliding beams by up to 100% from pre-electron cooling peak luminosity.

3.1.3   The Tevatron

The final stage of acceleration occurs in the Tevatron. A synchrotron with a circumference of 6.3 km, the Tevatron utilizes superconducting magnets with field strengths up

to 4.2 T. Both the protons and antiprotons are injected into the Tevatron from the Main Injector in bunches, at an energy of 150 GeV. For colliding physics runs, 36 bunches each of protons and antiprotons are injected in the Tevatron. The bunches are spaced such that they cross every 396 ns. Once in place, the Tevatron accelerates these bunches to an energy of 980 GeV. The Tevatron is divided into 6 sectors lettered "A" through "F" and each sector is further subdivided into 5 segments numbered 0-4 (the locations of A0 through F0 are shown in Figure 3.1). Each 0 segment contains a long straight section of the accelerator. Both the B0 segment (where the CDF detector sits) and the D0 segment (where the aptly named DØ detector sits) have quadrupole magnets that focus the beams and steer the proton and antiproton bunches into one another for collisions. The focusing reduces the beam spot size and thus increases the instantaneous luminosity of the beam. The instantaneous luminosity is given by

$$\mathcal{L} = \frac{N_B N_p N_{\bar{p}} f}{2\pi \sigma_p^2 \sigma_{\bar{p}}^2},$$ (3.1)

where N_B is the number of bunches present in the accelerator, N_p and $N_{\bar{p}}$ are the number of protons and antiprotons per bunch, f is the bunch revolution frequency, and σ_p and $\sigma_{\bar{p}}$ are the effective widths of the proton and antiproton bunches. Integrated luminosity, $\int \mathcal{L} dt$, when combined with the cross-section for $p\bar{p}$ collisions, gives a measure of the number of collisions in a given period of time. Figure 3.2 shows the total integrated luminosity at CDF as of February 2006. The analysis presented in this document was performed using an integrated luminosity of $\int \mathcal{L} dt = 1.0$ fb^{-1}. For comparison, the total integrated luminosity in Run I was $\int \mathcal{L} dt = 125$ pb^{-1}.

3.2   The CDF Detector

The CDF detector is an azimuthally and forward-backward symmetric detector designed to study $p\bar{p}$ collisions at the Tevatron. A schematic overview of the CDF detector
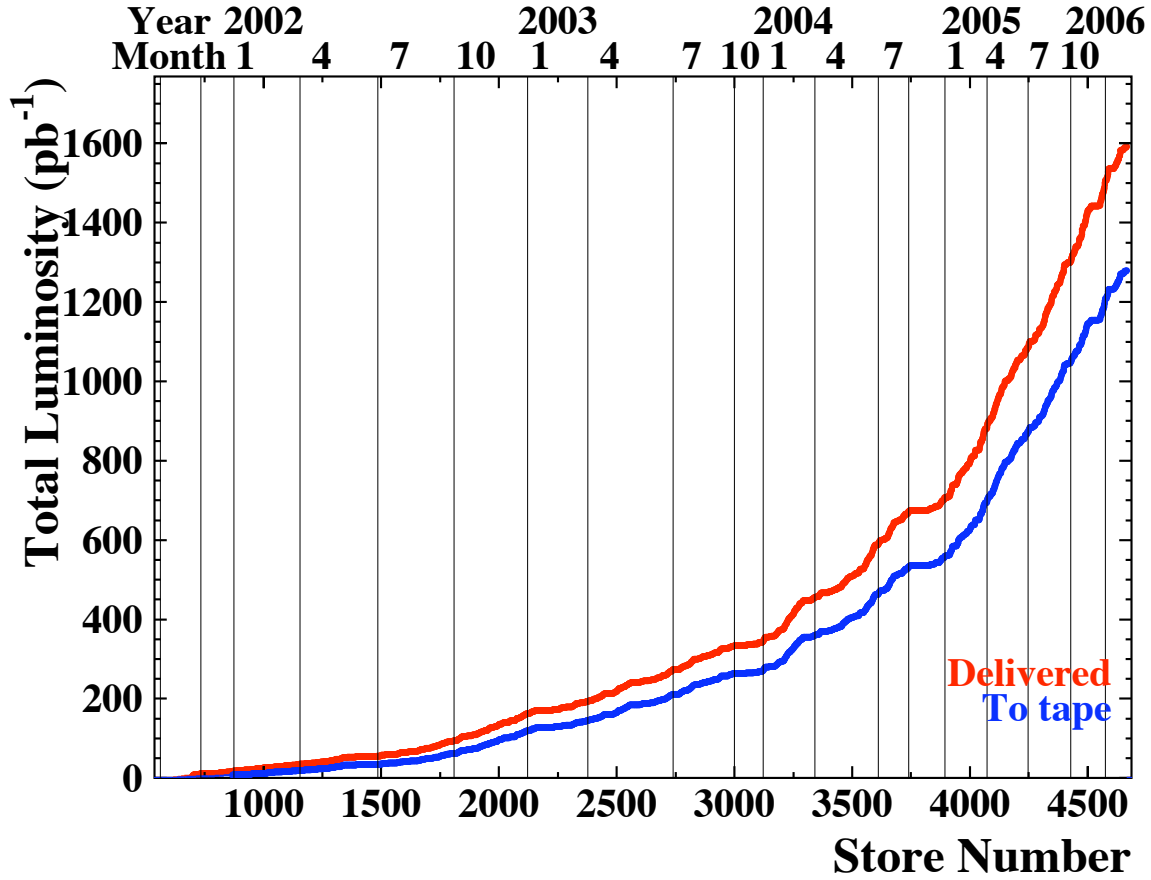
Figure 3.2: The total integrated luminosity at CDF as of February 2006. The red curve shows the total integrated luminosity delivered to CDF while the blue curve shows the total integrated luminosity written to tape at CDF.

is shown in Figure 3.3.

The CDF coordinate system is right-handed, with the z-axis pointing along a tangent to the Tevatron ring along the proton direction. The remaining rectangular coordinates x and y are defined pointing outward and upward from the Tevatron ring respectively. Often, it is more convenient to work in polar coordinates (which are facilitated by the symmetry of the CDF detector in the xy-plane), where $r \equiv \sqrt{x^2 + y^2 + z^2}$ and $\phi \equiv \tan^{-1}(y/x)$. The canonical third variable in the polar coordinate system is $\theta \equiv \cos^{-1}(z/r)$. However, θ is not invariant under longitudinal boosts. Since the constituent particles of the proton and the antiproton will not have an initial energy of 980 GeV, the production
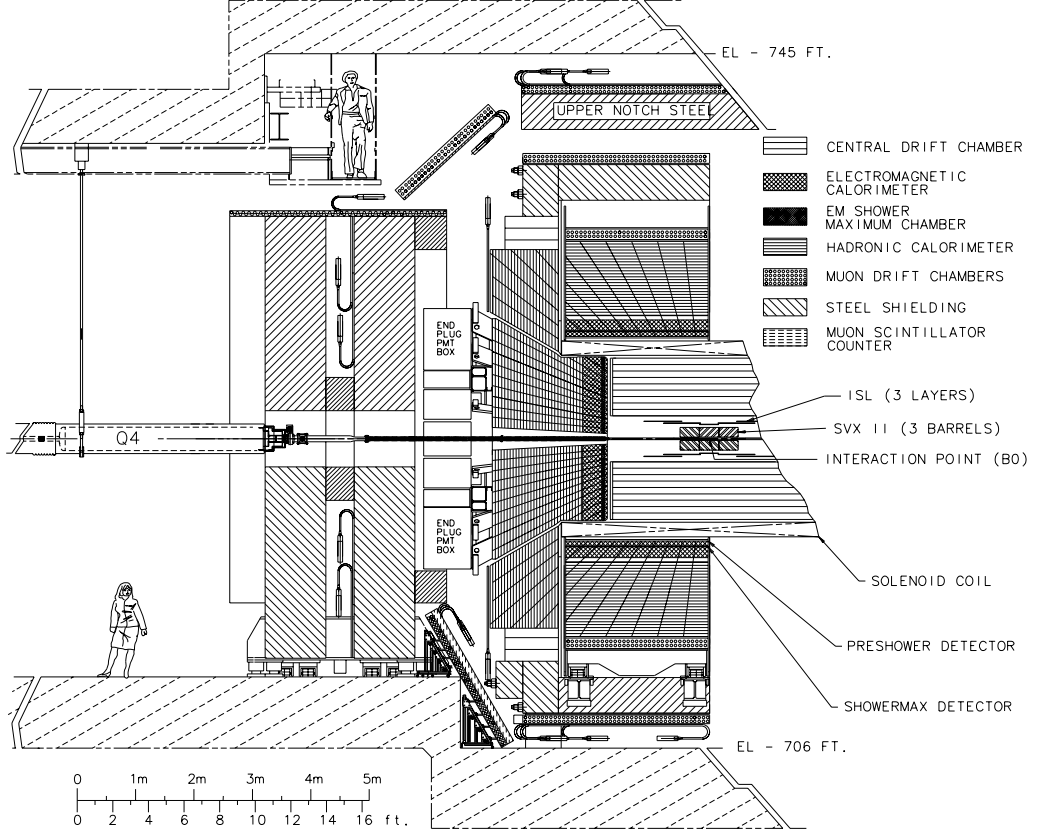
Figure 3.3: A cross-sectional view of the CDF detector [19].

of particles as a function of angle will depend on the initial velocities of the constituent particles. The rapidity, defined as:

$$\zeta \equiv \frac{1}{2} \ln \frac{E + p_z}{E - p_z} \tag{3.2}$$

is invariant under boosts along the z-axis. For the massless case ($p \gg m$), the rapidity can be approximated as the pseudo-rapidity, defined as:

$$\eta \equiv -\ln \tan \frac{\theta}{2}. \tag{3.3}$$

This coordinate is invariant under Lorentz transformation and is used as the third coordinate in the CDF coordinate system.

The basic structure of the CDF detector can be subdivided from the inside (starting

at the beampipe) out into: the tracking system (responsible for measuring momenta of charged particles), the calorimeters (responsible for measuring the energy of interacting particles), and the muon system (responsible for identifying muons).

3.2.1 The Tracking System

The CDF tracking system consists of a silicon microstrip tracker and an open-cell drift chamber. The silicon tracker consists of three subdetectors, listed in order of distance from the beampipe: Layer 00 (L00), the Silicon VerteX detector (SVX), and the Intermediate Silicon Layers (ISL). The drift chamber, known as the Central Outer Tracker (COT), surrounds the silicon tracking system.

The entire CDF tracking system is immersed in a 1.4 T magnetic field that is generated by a superconducting solenoid magnet. The solenoid has a radius of 1.5 m, is 5 m in length and has a stored energy of 30 MJ when at full field strength. The magnetic field produced by the solenoid is uniform along the direction of the z-axis. Charged particles within the magnetic field follow helical trajectories. The radius of curvature and the orientation of the helix can be used to determin the momentum and charge of a charged particle. A schematic overview of the CDF tracking system is shown in Figure 3.4.

Silicon Detector

The silicon detector, which provides high-resolution position measurements of charged particles close to the interaction region, consists of three subdetectors. The main subdetector is the SVXII [20] detector, a five layer, double-sided silicon detector that covers the radial region between 2.5 cm and 10.6 cm. The SVXII detector is composed of three cylindrical barrels, each 16 cm long in the z-direction (see Figure 3.5). Each barrel is divided into 12 azimuthal wedges of 30° each. Each of the five layers in a wedge is further divided into electrically independent modules called ladders. There are a total of
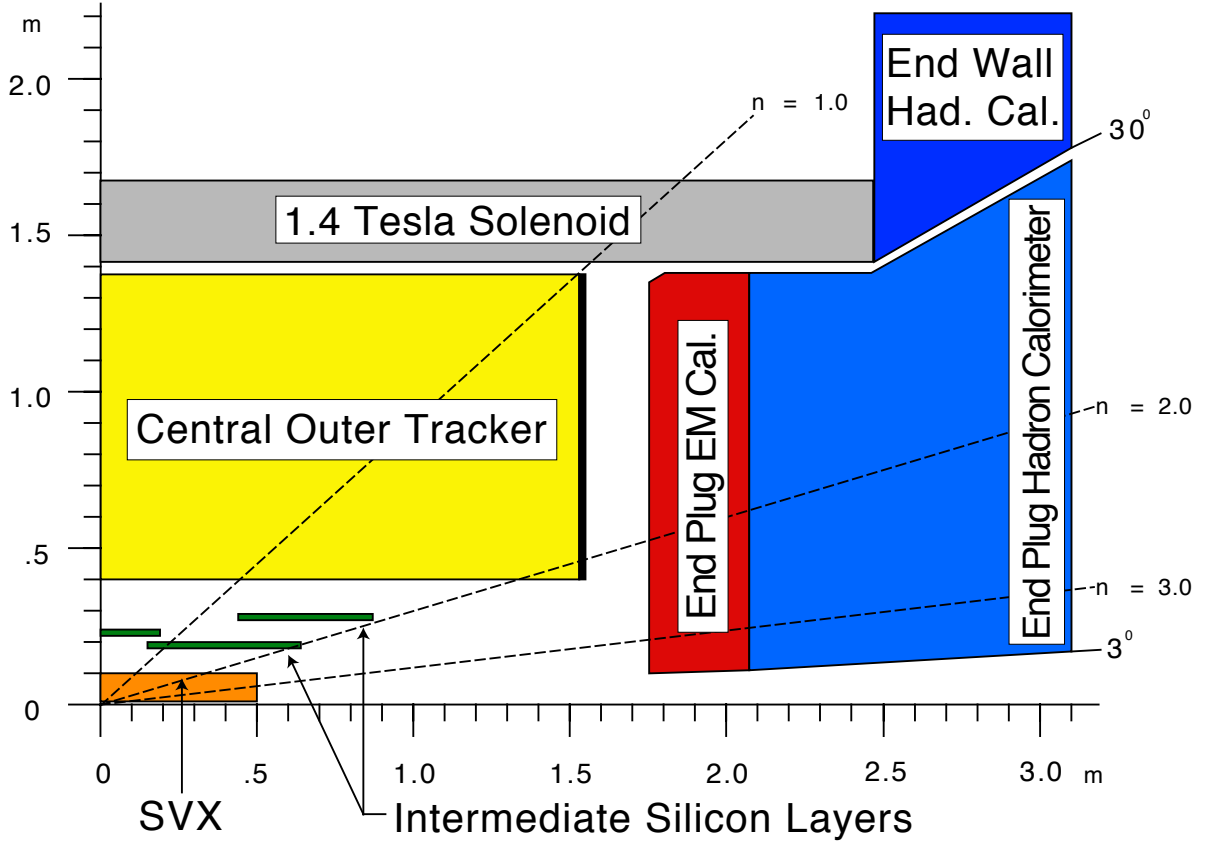
Figure 3.4: A schematic overview of the CDF tracking system. The region of the detector with $|\eta| < 1.0$ is referred to as the "central" region.

360 ladders in the SVXII detector. The double-sided silicon microstrips of the SVXII detector are arranged so that one side is aligned with the z-axis (known as "axial" strips) and the other side is either at an angle of 90° or 1.2° with respect to the axial layer. These arrangements make it possible to make three-dimensional position measurements by combining the $(r - \phi)$ and $(r - z)$ measurements.

The innermost subdetector of the silicon detector, Layer 00 (L00) [21], is a single-sided layer of silicon wafers mounted directly on the beampipe at a radius of 1.6 cm and provides measurements closest to the interaction point. The outermost subdetector, the Intermediate Silicon Layers (ISL) [22], is comprised of one or two additional layers of
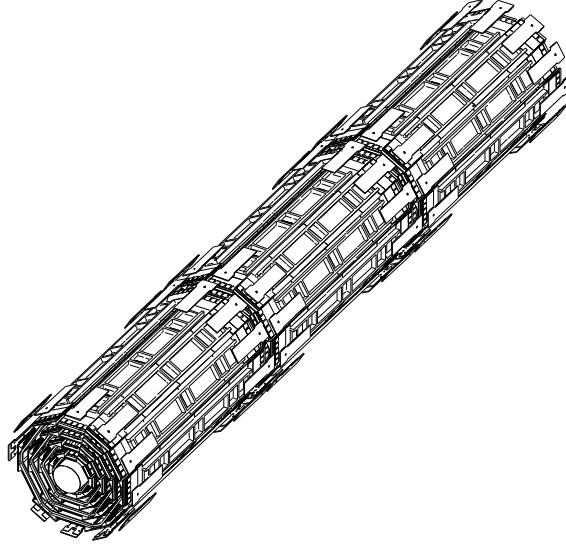
Figure 3.5: The SVX barrel structure [19].

double-sided silicon, depending on the polar angle, at radii from 20 cm to 28 cm. The ISL serves to extend silicon tracking coverage up to $|\eta| < 2$. Combined, the CDF silicon detector has a total of 722,432 channels.

COT

The Central Outer Tracker (COT) [23], a large open-cell drift chamber, is positioned outside the silicon detector from radii of 0.43 m to 1.32 m. The COT contains 8 "superlayers" each containing 12 wire layers for a total of 96 layers. Four of the superlayers provide $R - \phi$ measurements (axial superlayers) while the other four provide 2° measurements (stereo superlayers). The drift chambers are filled with a 1:1 mixture of argon and ethane. This mixture provides for a maximum drift time of 177 ns with a drift velocity of 100 μm/ns, which prevents pileup of events in the drift chamber from previous events. The resulting transverse momentum resolution of the COT is $\sigma_{p_T}/p_T \approx 0.15\% \times p_T$.

System	Coverage in η	Thickness	Energy Resolution
CEM	$|\eta| < 1.1$	$18X_0, 1\lambda$	$13.5\%/\sqrt{E_T} \oplus 2\%$
PEM	$1.1 < |\eta| < 3.6$	$21X_0, 1\lambda$	$16\%/\sqrt{E} \oplus 1\%$
CHA	$|\eta| < 0.9$	4.5λ	$50\%/\sqrt{E_T} \oplus 2\%$
WHA	$0.7 < |\eta| < 1.2$	4.5λ	$75\%/\sqrt{E} \oplus 4\%$
PHA	$1.2 < |\eta| < 3.6$	7λ	$80\%/\sqrt{E} \oplus 5\%$

Table 3.1: Properties of the CDF II calorimeter systems. The energy resolutions for the electromagnetic calorimeters are for electrons and photons; the resolutions for the hadronic calorimeters are for isolated pions.

In combination the Silicon and COT detectors provide excellent tracking up to $|\eta| \leq 1.1$ with decreasing coverage to $|\eta| \leq 2.0$.

3.2.2 Calorimeters

The CDF calorimetry system sits outside the solenoid and is responsible for measuring particle energies. The calorimeters comprising it sample electromagnetic and hadronic showers produced as particles traversing them interact with dense material. The system covers a full 2π in azimuth and is subdivided into a "central" region ($|\eta| < 1.1$) and a "plug" region ($1.1 < |\eta| < 3.6$). Each calorimeter is segmented into "towers", containing alternating layers of scintillator and inert material. Each calorimeter system described below consists of an electromagnetic component and a hadronic component. The electromagnetic component measures the energy of electrons and photons by sampling electromagnetic showers caused by bremsstrahlung of the electron or e^+e^- pair production of the photon. The hadronic component measures the energy of hadrons and jets by sampling electromagnetic showers due to neutral meson production and their subsequent electromagnetic decay and hadronic showers due to strong interactions of hadrons with heavy atomic nuclei. A summary of the CDF calorimeter systems is shown in Table 3.1

The Central Calorimeter

In the central region of $|\eta| < 1.1$, the calorimeter towers subtend $15°$ in ϕ and 0.1 in η. The central electromagnetic calorimeter (CEM) [24] constitutes the front of the wedges in the central region. The CEM consists of alternating layers of lead and scintillator, amounting to 18 radiation lengths[2] of material. Embedded in the CEM is the shower maximum detector (CES). The CES provides position measurements of the electromagnetic showers at a depth of 5 radiation lengths and is used in electron identification. Behind the CEM is the central hadronic calorimeter (CHA) [25], which provides energy measurements of hadronic jets. The CHA consists of 4.7 interaction lengths[3] of alternating steel and scintillator. The CHA covers the region up to $|\eta| < 0.9$.

The End-Wall and Plug Calorimeter

Since the CHA covers only the region up to $|\eta| < 0.9$, the end-wall hadronic calorimeter (WHA) was constructed to cover the region from $0.7 < |\eta| < 1.2$. Its construction is otherwise very similar to the CHA. The plug electromagnetic calorimeter (PEM) [26] consists of alternating lead absorber and scintillating tile readout with wavelength shifting fibers; the total thickness is 23.2 radiation lengths of material. A plug shower maximum detector (PES) [27] provides position measurement of electron and photon showers. The plug hadronic calorimeter (PHA) has alternating layers of iron and scintillating tile for a total of 6.8 interaction lengths.

3.2.3 The Muon Detector

As muons are 200 times more massive than electrons, they lose considerably less energy due to bremsstrahlung in the calorimeter and thus are effectively not detectable by the

---

[2]The radiation length, X_0, is defined as the distance over which a high-energy electron loses all but $1/e$ of its energy by bremsstrahlung.

[3]The interaction length, λ, is defined as the mean free path of a particle before undergoing an inelastic nuclear interaction.
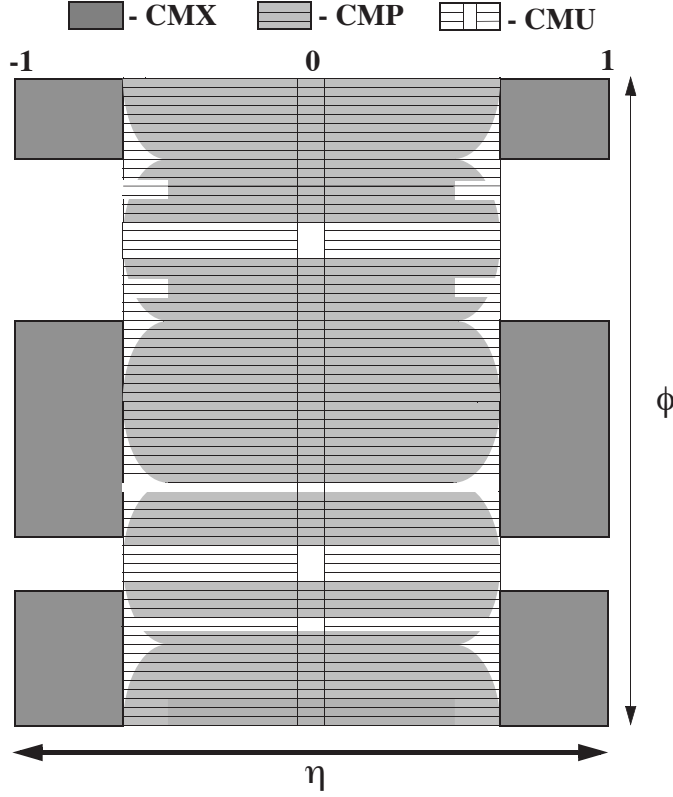
Figure 3.6: Coverage of the CDF muon systems.

calorimeter. Thus, the muon detectors sit on the very outside of the CDF detector, and are separated from the calorimeter by a layer of steel shielding. This layer of shielding serves to absorb charged pions which can traverse the whole of the calorimeter and could incorrectly be interpreted as muons. Unlike the tracking and calorimetry systems, the muon system is incomplete in ϕ, due to space constraints. Its coverage is shown in Figure 3.6.

The muon detection system consists of three sandwiched drift tube layers, each utilizing single wire drift cells four layers deep. Directly behind the central hadronic calorimeter and the layer of steel shielding is the central muon detector (CMU) [28] which can detect muons with $p_T > 1.4$ GeV/c in the region of $|\eta| < 0.6$. Additional muon coverage in this region is provided by the central muon upgrade (CMP) which is separated from the CMU

by 60 cm of steel. The CMP detects muons with $p_T > 2.0$ GeV/c. The central muon extension (CMX) provides further coverage in the region of $0.6 < |\eta| < 1.0$.

3.2.4   Trigger System

Of the over 2 million $p\bar{p}$ collisions that occur every second during operation of the Tevatron collider, the vast majority are not interesting in the study of high energy physics. CDF employs a three-level trigger system to select events involving physically relevant phenomena and record them, while rejecting uninteresting events. Due to the physical limitations involved in physical storage and the rate at which data can be stored, the trigger system must reduce the data acquisition rate from the approximately 2 MHz collision rate to approximately 75 Hz. An overview of the CDF Trigger system is presented in Figure 3.7.

Level 1 Trigger

The level 1 trigger utilizes custom designed hardware to make decisions based on simple physics quantities within events. Raw information from the detector from every beam crossing is stored in a pipeline capable of buffering data from 42 beam crossings. Processing of this data takes place in one of three streams. One analyzes calorimeter information to identify objects that may further be reconstructed into electrons, photons or jets. Another stream searches for track segments in the muon detector, or "stubs", which may be used in conjunction with tracks in the tracking system to reconstruct muons. The third stream utilizes tracking data to identify tracks that can be linked to objects in the calorimeter or muon detector. The level one trigger decision takes place 5.5 μs after a collision and reduces the event rate to approximately 50 kHz.
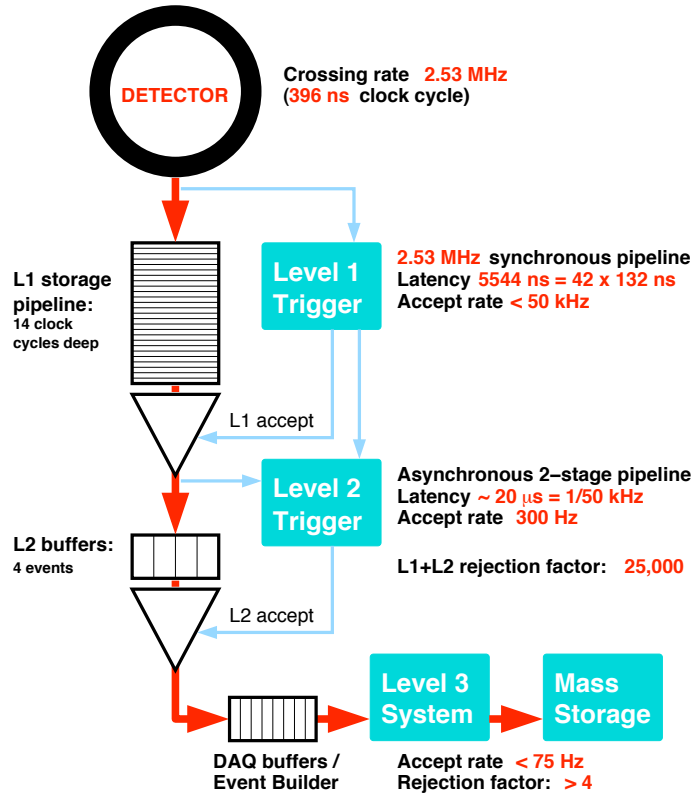
Figure 3.7: The CDF Trigger and Data Acquisition System.

Level 2 Trigger

The level 2 trigger utilizes programmable processors to perform limited event reconstruction on events accepted by the level 1 trigger. These events are then stored in one of four asynchronous buffers and a decision is made as to whether the events pass one of the pre-defined level 2 trigger criteria. The decision time for the level 2 trigger is approximately 25 μs. The level 2 trigger further reduces the event rate to approximately 300 Hz.

Level 3 Trigger

The level 3 trigger consists of two components: an "event builder" that uses custom hardware to assemble data from all subdetectors of CDF into a reconstructed event, and

a large processing farm consisting of commodity computing hardware. Each processor in the processing farm can then make a decision as to whether an event reconstructed by the event builder satisfies pre-defined level 3 trigger criteria. The level 3 trigger then separates events into streams based on the physics objects that resulted in their trigger and commits them to permanent storage. The level 3 trigger reduces the event rate to approximately 75 Hz.

CHAPTER 4

Data Sample and Event Selection

We select $t\bar{t} \to b\ell\nu_\ell\bar{b}\ell'\bar{\nu}_{\ell'}$ decays with a high-p_T lepton trigger and the requirement that candidates have (i) two leptons each with $p_T > 20$ GeV/c, (ii) significant missing energy transverse to the beam direction ($\displaystyle{\not}E_T$), and (iii) two jets each with $E_T > 15$ GeV. Missing transverse energy is calculated as

$$\displaystyle{\not}E_T = -\sum_i E_T^i \vec{n}_i, \qquad (4.1)$$

where E_T^i are the magnitudes of transverse energy contained in each calorimeter tower i, and $\vec{n}_i$ is the unit vector from the interaction vertex to the tower in the transverse (x, y) plane. $\displaystyle{\not}E_T$ is corrected for the presence of isolated high-p_T muons by subtracting the momentum lost by the muons in the calorimeter and adding the muon p_T to the vector sum.

The selection was designed for a cross-section measurement and is described as "DIL" in [29]. A description of the trigger requirements and selection used to obtain this dataset follows.

4.1 Trigger Requirements

The trigger requires at least one high-p_T lepton. For central electron candidates, the first two trigger levels require an electromagnetic calorimeter cluster with a confirming

track in the COT and without a large hadronic energy deposit. The third level trigger requires an electron candidate with $E_T \geq 18$ GeV. Events with electron candidates in the plug ($|\eta| > 1.2$) are required to have electron $E_T > 20$ GeV and $\not{E}_T > 15$ GeV. For muon candidates, the first two trigger levels require hits in the muon chambers and a confirming COT track. The third level trigger requires a muon stub with a matching track of $p_T \geq 18$ GeV/c.

4.2 Event Selection

4.2.1 Leptons

After offline event reconstruction, tighter cuts are placed on the leptons that pass the basic trigger requirements.

Electron candidates are required to have an electromagnetic calorimeter cluster with $E_T > 20$ GeV and muon candidates to have a track with $p_T > 20$ GeV/c. At least one of the leptons is required to be isolated in the calorimeter, where the lepton contains at least 90% of the total E_T within a cone $\Delta R \equiv \sqrt{(\Delta\eta)^2 + (\Delta\phi)^2} = 0.4$. In addition, electron candidates are required to have a well-measured track pointing at an energy deposition in the calorimeter. For electron candidates with $|\eta| > 1.2$, this track association uses a calorimeter-seeded silicon tracking algorithm [30].

Muon candidates are required to have a well-measured track linked to hits in the muon chambers and energy deposition in the calorimeter consistent with that expected for muons. If the event contains two muons, only one is required to have hits in muon chambers used in the trigger decision. The other muon may have hits in chambers not used for the trigger decision if there is a matching COT track, or no hits in muon chambers if the COT track points in regions where there is no muon chamber coverage.

4.2.2 Jets

Quarks and gluons formed in collisions or from decays of other particles will either immediately decay (in the case of the top quark), or fragment and combine with other quarks and gluons to form color-neutral particles called hadrons[1], a process called hadronization. This process usually results in a stream of energetic hadrons with momenta distributed in a cone around the direction the original quark or gluon was traveling. This object is referred to as a hadronic jet, or simply, a jet. While hadronization makes direct measurement of a quark or gluon's momentum impossible, the energy and direction of a jet can be used to infer the momentum of the underlying quark or gluon.

Jets are identified using a process called clustering; the clustering algorithm used at CDF is called JETCLU [31]. Jet clustering is done by first identifying an energetic tower with $E_T > 1$ GeV, called a "seed tower." The energy of all the towers in a cone of $\Delta R = 0.4$ around the seed tower is then calculated. A new centroid of the tower is then calculated as:

$$\eta = \frac{\sum_i E_T^i \eta^i}{\sum_i E_T^i}, \qquad\qquad \phi = \frac{\sum_i E_T^i \phi^i}{\sum_i E_T^i}, \qquad\qquad (4.2)$$

where the sum is performed over all towers in the cluster. A cone of $\Delta R = 0.4$ is then drawn around the new cluster centroid, and the above process is repeated until the cluster remains unchanged. After the clustering process is completed, the "raw" jet energy can be calculated.

The jets resulting from the b-quarks in the top decay carry the most kinematic information about the mass of the parent top quark of any of its decay products. However, since jets are measured with poor energy resolution relative to leptons, they also are the largest source of uncertainty in the measurement of the top mass.

---

[1]Hadrons are particles formed from the combination of a quark and anti-quark (called "mesons") or three quarks or antiquarks (called "baryons").
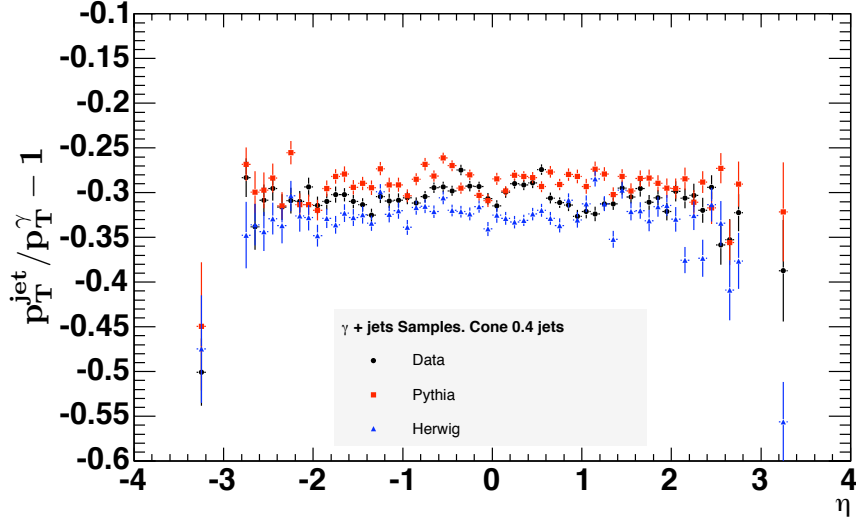
Figure 4.1: $p_T^{jet}/p_T^{\gamma} - 1$ in γ+jets events as a function of η of the jets after relative corrections are applied. Response is seen to be nearly flat for data as well as for events simulated with PYTHIA [33] or HERWIG [34].

Jet Corrections

A series of corrections is made to raw jet energies to best approximate parton energies. These corrections are largely derived in dijet and minimum bias samples which are independent of the underlying physics process and are described in detail in Ref. [32].

First, a dijet balancing procedure is used to correct for non-uniformities in the response of the calorimeter as a function of η; these corrections are referred to as "relative corrections." Events with exactly two jets, one of which is in the central region, are chosen. The knowledge that the E_T of both jets should be equal is used to extract a correction as a function of the jet p_T and η. The relative correction ranges from +15% to -10%. Applying this correction to both γ+jets data and simulated events from two different event generators, we find that the calorimeter response is almost flat with respect to η as seen in Figure 4.1.

A small, approximately 1%, correction is then applied for events containing multiple

$p\bar{p}$ collisions in the same accelerator bunch. This correction is needed to account for energy from different collisions in the same bunch falling inside the jet cluster and thus increasing the energy of the measured jet. In addition, a correction is made to subtract energy associated with spectator partons in the underlying event.

Finally an absolute scale correction is needed to account for any non-linearity and energy loss in the un-instrumented regions of each calorimeter. The response of the calorimeter is measured using E/p of single tracks in the data. Studies of energy flow and jet shapes in the data are also used in constraining the modeling of jet fragmentation. This information is used to tune the simulation to model observations in the data, and high statistics simulation samples are then used to extract the approximately 10-30% absolute scale correction.

After the above corrections, the momentum components of each b quark are estimted from the measured jet E_T and angle assuming a b quark mass of 4.7 GeV/c^2 [8]. Events are then required to have at least two jets with $|\eta| < 2.5$ and $E_T > 15$ GeV.

4.2.3 Final Selection Cuts

After lepton and jet identification, further requirements are made to reduce the expected level of background in the sample. Events are required to have missing transverse energy of $\not{E}_T > 25$ GeV. In events with $\not{E}_T < 50$ GeV, the direction of the $\not{E}_T$ vector is required to be separated by at least 20° in ϕ from any lepton or jet in the event. This reduces the background from Drell-Yan production of τ pairs as well as the number of events in which mismeasured jet or lepton energy contributes a large fraction of the $\not{E}_T$.

To reduce the number of $Z/\gamma^* \rightarrow ee, \mu\mu$ events in which mismeasured jet energy leads to significant amounts of measured missing tranverse energy, ee and $\mu\mu$ events with dilepton invariant mass between 76 and 106 GeV/c^2 are required to have their $\not{E}_T$ vector

point away from any energetic jets in the event. This is done by requiring these events to have jet significance $\sigma_{jet} > 8.0$, where jet significance is defined as:

$$\sigma_{jet} \equiv \frac{\not{E}_T}{\sqrt{\sum_k (\not{E}_T \cdot E_T^k)}}, \qquad (4.3)$$

where the sum is performed over all jets passing jet selection cuts defined in Section 4.2.2 that are in the same hemisphere as $\not{E}_T$.

To further suppress background, events are required to have H_T, defined as the scalar sum of E_T of all leptons and jets passing the above cuts and $\not{E}_T$, greater than 200 GeV.

Events which are likely to be due to cosmic rays are removed by requiring a coincidence of the muon arrival times to the calorimeter. Electrons resulting from photon conversion to $e^+ e^-$ pairs are also removed. Conversions are identified by pairing the electron track to a track of opposite sign and requiring that the two tracks are consistent with originating from a common vertex and being parallel at that vertex. Events with three leptons are removed as well as events in which the leptons have the same sign (no such events are found in the data after all other selection cuts have been made).

4.3 Backgrounds

While the selection criteria above are designed to minimize the amount of background in the sample, approximately 40% of the final dilepton top sample is expected to be composed of background events.

The largest source of background in the sample is Drell-Yan (Z/γ^*) decaying to ee and $\mu\mu$ final states with associated jets. Since there are no neutrinos in these events, in order to pass the $\not{E}_T$ cut, they must have substantial $\not{E}_T$ resulting from mismeasurement of the jet energies. Because of this, the contribution of this background is estimated using Z events in data as well as Monte Carlo events.

The second largest source of background in the sample are events in which an object is incorrectly identified as a lepton, or "fake" events. These events are mostly the result of $W \to \ell\nu$+jets events where one jet gets reconstructed as a lepton. The contribution to the final sample from these events is determined by applying a lepton fake rate to a data sample of $W \to \ell\nu$+jets events. The lepton fake rate is determined using a large data sample collected using a trigger on jets with $E_T > 50$ GeV from which known sources of real leptons are removed.

The remaining sources of background, including diboson (WW and WZ) production with associated jets and $Z/\gamma^* \to \tau\tau$ events are smaller and have their contributions estimated using ALPGEN [35] Monte Carlo events of each process.

All remaining sources of background are assumed to have negligible contribution to the sample.

4.4   Sample Composition

The accuracy of the background predictions for the DIL selection can be tested by predicting the number of events expected in the sample with exactly one jet or no jets passing the selection cuts. These events are expected to be nearly entirely background. The predicted number of events can compared to the number seen in the data with zero or one jets. As seen in Figure 4.2, the events in the data agree well with the prediction for the background events.

Table 4.1 lists the number of expected background events of each type and the number of $t\bar{t}$ signal events expected at various top quark masses [15] for the data sample used in this measurement. The signal estimate includes $t\bar{t}$ events in which a W decays to a τ when the τ decays to an e or a μ. Studies in Monte Carlo simulations show that 14% of the accepted signal events have at least one W decaying to a τ. In the 1.0 fb^{-1} data
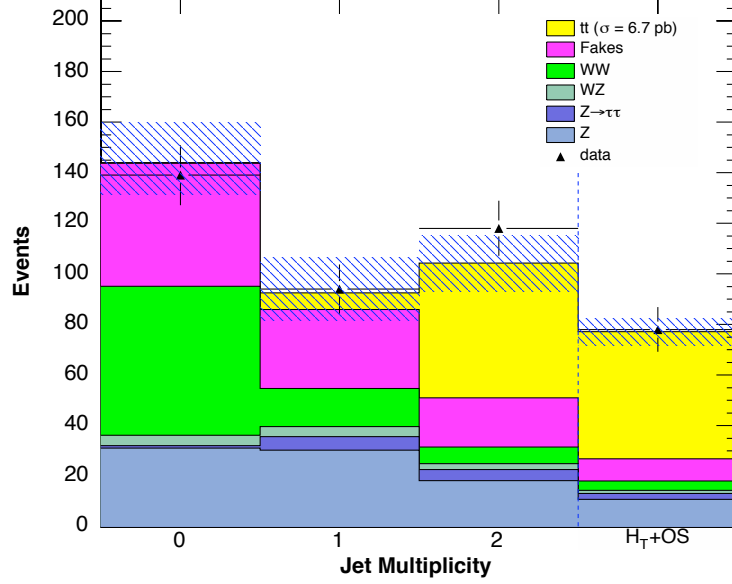
Figure 4.2: The predicted jet multiplicity of events in the DIL selection with that observed in the data overlaid. The first three bins contain events that have not had the H_T and opposite sign cut applied to them while the final bin contains events passing all selection cuts outlined in this chapter.

sample used, 78 events satisfy all of the selection cuts described in this chapter.

The fraction of $t\bar{t}$ events that will pass our selection criteria will increase as a function of the true top mass. This is due to the fact that a more massive top quark will have more energetic decay products that are more likely to pass the kinematic selection cuts in place. We calculate the overall acceptance of the selection criteria used by applying it to $t\bar{t}$ events simulated with HERWIG [34] at a range of top quark masses. The acceptance at each mass, along with a second-order polynomial fit to these points is shown in Figure 4.3.

Source	Events
$t\bar{t}$ ($M_t = 165$ GeV/c^2, $\sigma = 9.1$pb)	63.4 ± 1.7
$t\bar{t}$ ($M_t = 175$ GeV/c^2, $\sigma = 6.7$pb)	50.2 ± 1.7
$t\bar{t}$ ($M_t = 185$ GeV/c^2, $\sigma = 4.9$pb)	38.9 ± 1.7
Total Expected Background Rate	26.9 ± 4.8
WW	3.8 ± 1.0
WZ	1.3 ± 0.2
$Z/\gamma^* \to ee, \mu\mu$	10.9 ± 4.4
$Z/\gamma^* \to \tau\tau$	2.2 ± 0.5
Fakes	8.7 ± 1.5
Total Expected Rate ($M_t = 165$ GeV/c^2)	90.3 ± 5.1
Total Expected Rate ($M_t = 175$ GeV/c^2)	77.1 ± 5.1
Total Expected Rate ($M_t = 185$ GeV/c^2)	65.8 ± 5.1
Observed in Data ($\int \mathcal{L}dt = 1.0$ fb^{-1})	78

Table 4.1: Expected numbers of signal and background events for a data sample of $\int \mathcal{L}dt = 1.0$ fb^{-1}. The signal cross section is obtained from [15]. The total expected background is the sum of the indented background contributions.
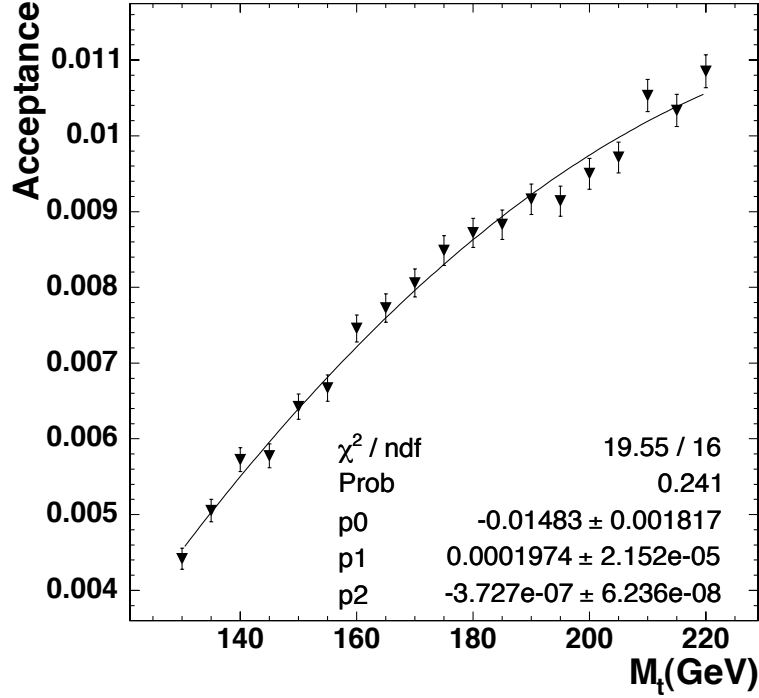
Figure 4.3: The Acceptance of the DIL selection criteria as a function of top quark mass. The sample of simulated event used is generated using the HERWIG generator [34] and includes $t\bar{t}$ decays to all standard model decay channels with the theoretically predicted branching ratios. The parameterization shown is for a fit to the function $A = p_0 + p_1 M_t + p_2 M_t^2$.

CHAPTER 5

Method Overview

The most commonly used approach to measure the top quark mass has been to use template-based methods. These methods measure a reconstructed mass[1] per event and compare the distribution of reconstructed mass in the data to templates from a variety of top quark masses. The calculation of a reconstructed mass requires making several kinematic assumptions (*e.g.* the invariant masses of both intermediate-state W-bosons being equal). The templates are parameterized using Monte Carlo event generators and detector simulations. Template-based methods have been used to make all measurements of the top quark mass in the dilepton channel from Run I data [36, 37]. Since these methods utilize fully simulated events to form templates, they take into account all detector effects accounted for in the simulation. However, only a single number, a reconstructed mass, enters into the final likelihood per event. In addition, all events, regardless of their kinematic consistency with the $t\bar{t}$ process, have equal weight in the final likelihood.

A different class of methods, such as the one used in this analysis, utilizes our theoretical knowledge of the underlying physics processes to construct per-event likelihoods. These methods, commonly known as "matrix-element methods," are grounded in ideas proposed before the discovery of the top quark [38, 39] and pioneered for usage in the

---

[1]This approach can be used using any kinematically reconstructible quantity, such as the event mass.

38

lepton+jets channel [40, 41, 42].

We construct per-event likelihoods by convolving the matrix element for $t\bar{t}$ decays and detector resolution functions. Rather than making the kinematic assumptions made in template-based methods, we instead integrate over unmeasured quantities. This allows for maximal extraction of information from each event as the full phase-space of unmeasured quantities is explored via integration. The final joint likelihood is a product of the per-event likelihoods. This procedure weights events according to the relative amount of information they carry. For computational tractability, a series of simplifying assumptions must be made. These assumptions are accounted for by calibrating the final response of the method using simulated events.

This chapter provides a brief overview of the method used. More detailed descriptions of each part of the method are provided in chapters 7, 8, and 9.

5.1 Signal Likelihood

The probability density for $t\bar{t}$ decays is expressed as $P_s(\mathbf{x}|M_t)$, where M_t is the top quark pole mass and $\mathbf{x}$ is a vector of measured quantities in the event (lepton momenta, jet momenta and missing transverse energy). We calculate $P_s(\mathbf{x}|M_t)$ using the theoretical description of the $t\bar{t}$ production and decay process expressed with respect to $\mathbf{x}$,

$$P_s(\mathbf{x}|M_t) = \frac{1}{\sigma(M_t)} \frac{d\sigma(M_t)}{d\mathbf{x}}, \tag{5.1}$$

where $\frac{d\sigma}{d\mathbf{x}}$ is the differential cross section evaluated with respect to event measurements contained in $\mathbf{x}$.

If the momenta of the initial-state and final-state partons were known exactly, the evaluation of the differential cross section would reduce to the expression

$$\frac{d\sigma(M_t)}{d\mathbf{x}} = \int d\Phi |\mathcal{M}_{t\bar{t}}(q_1, q_2, \mathbf{p}; M_t)|^2 f_{PDF}(q_1) f_{PDF}(q_2), \tag{5.2}$$

39

where $\mathcal{M}$ is the leading order matrix element for top pair production and decay, q_1 and q_2 are the initial state partons, $\mathbf{p}$ is a vector of final state particle momenta, f_{PDF} are the parton distribution functions[2] [43], and $d\Phi$ is the phase space for the process $q\bar{q} \to t\bar{t} \to bl\nu_l \bar{b} l' \nu_{l'}$.

The matrix element depends on the momenta of the incoming partons (q_1 and q_2), and of the outgoing two b-quarks (p_1 and p_2), two leptons (ℓ_1 and ℓ_2), and two neutrinos (ν_1 and ν_2). Observed quantities consist of jets ($j_1, \dots j_i$), measured leptons (L_1 and L_2), and two components of missing transverse energy. To express the differential cross section with respect to these observed quantities $\mathbf{x}$, transfer functions are introduced to connect the quantities which correspond to external legs of the matrix element ($q_1, q_2, p_1, p_2, l_1, l_2, \nu_1, \nu_2$) to the observed quantities ($j_1, \dots, j_i, L_1, L_2$). Quantities which are well-measured by the detector, lepton momenta and jet angles, are described by delta functions which directly reduce the number of unknown parton-level quantities. Integrations are performed over quantities which are not directly measured, $i.e.$ quark and neutrino energies. While quark energies are not directly measured, they can be estimated from the observed energies of the corresponding jets. The transfer function between quark and jet energies parameterizes this relationship, and is expressed as $W(E_p, E_j)$, the probability of measuring jet energy E_j given parton energy E_p.

We make the following assumptions regarding the transfer between parton-level quantities and the observables:

- Leptons are measured perfectly. We express the lepton transfer functions as a three-dimensional δ-function,

$$\delta^3(\ell_1 - L_1)\, \delta^3(\ell_2 - L_2).$$

---

[2]The Parton Distribution Functions (PDFs), describe the probability that a parton, q, will carry a given fraction of the momentum of the system.

- Jet angles are measured perfectly, and jet energy can be described as a parametric function of parton energy. We express the b-quark to jet transfer function as

$$\delta(\theta_{j_1} - \theta_{p_1})\delta(\phi_{j_1} - \phi_{p_1})W(E_{p_1}, E_{j_1})W(E_{p_2}, E_{j_2}).$$

- Incoming partons are massless and have no transverse momentum.

- The two leading jets come from b-quarks.

- Masses of the final state leptons are zero, masses of the b-quarks are set to 4.7 GeV/c^2.

These assumptions, while reasonable approximations, are not fully held in realistic events, resulting in the measured statistical uncertainty being underestimated in these events. The effect of these assumptions is considered in detail in Chapter 7. We can correct for this effect by performing pseudo-experiments of simulated events as described in Chapter 9.

The probability density in $\mathbf{x}$ for $q\bar{q} \to t\bar{t} \to \bar{b}\ell^-\bar{\nu}_\ell b\ell'^+\nu'_\ell$ for a fixed M_t can be written as

$$P_s(\mathbf{x}|M_t) = \frac{1}{\sigma(M_t)} \int d\Phi \sum_{a,b} |\mathcal{M}_{t\bar{t}}(q_i, p_i; M_t)|^2 W(p, x) f^a_{\text{PDF}}(q_1) f^b_{\text{PDF}}(q_2). \qquad (5.3)$$

In this expression, the integral is over the phase space $d\Phi$ for $q\bar{q} \to t\bar{t} \to bl\nu_l\bar{b}l'\nu_{l'}$, the sum runs over the flavors a, b of the incoming partons, and f^a_{PDF} are parton distribution functions for flavor a. The transfer functions, $W(p, x)$, link the measured quantities $\mathbf{x}$ to the parton-level ones, p, and are described in detail in Chapter 6. Constraints such as conservation of momentum which appear as delta functions and modify the integration are here implicitly included in the phase-space integration and are discussed in detail in Chapter 7. The term, $1/\sigma(M_t)$, in front of the integral ensures the normalization condition

for the probability,

$$\int d\mathbf{x} \ P_s(\mathbf{x}|M_t) = 1, \tag{5.4}$$

where the integration is performed over all accepted $\mathbf{x}$ to account for mass-dependent effects of the selection.

5.2 Accounting for Background Processes

While the expression in equation 5.3 would be sufficient to extract the top mass in a pure $t\bar{t}$ sample, the data sample which we use to perform this measurement contains several sources of background. We calculate the probability for the dominant background processes, $P_b(\mathbf{x})$ and form the generalized per-event probability density in $\mathbf{x}$,

$$P(\mathbf{x}|M_t) = P_s(\mathbf{x}|M_t)p_s(M_t) + P_{b_1}(\mathbf{x})p_{b_1} + P_{b_2}(\mathbf{x})p_{b_2} + \cdots , \tag{5.5}$$

as a weighted sum of the probabilities for each process, where the weights $p_s(M_t)$ and p_{b_i} are determined from the expected fractions of signal and background events (see Table 4.1). We evaluate probabilities for the three largest expected backgrounds: Z/γ^* with associated jets, W+3 jets production in which one jet is incorrectly identified as a lepton ("fakes"), and W pair production with associated jets. These background probabilities are described in detail in Chapter 8.

CHAPTER 6

Transfer Functions

The transfer functions describe the probability of reconstructing an object of energy y given a corresponding parton of energy x immediately after the hard-scattering process. For quantities that are assumed to be measured perfectly, such as lepton momentum, this reduces to a δ-function, $\delta(x - y)$. Of particular importance to this measurement is the jet-parton transfer function, $W(E_p, E_j)$, which describes the probability of a parton with energy E_p being measured as a jet with energy E_j in the CDF detector. In addition, we construct transfer functions which allow us to estimate the p_T of the $t\bar{t}$ system given the measured recoil energy in the event.

6.1 Jet Transfer Functions

The transfer function between quark and jet energies, $W_j(E_p, E_j)$, expresses the probability of measuring jet energy E_j from a given parton with energy E_p such that

$$n(E_j, E_p)dE_jdE_p = n(E_p)dE_pW_j(E_p, E_j), \tag{6.1}$$

where $n(E_j, E_p)dE_jdE_p$ is the number of events with jet energy between E_j and $E_j + dE_j$ and parton energy between E_p and $E_p + dE_p$, and $n(E_p)$ is the number of partons with energy between E_p and $E_p + dE_p$.

p_i	a_i	b_i
p_1	1.90 ± 0.62 GeV	0.023 ± 0.008
p_2	2.83 ± 0.54 GeV	0.075 ± 0.005
p_3	0.70 ± 0.08	0.000 ± 0.001 GeV^{-1}
p_4	-1.79 ± 0.79 GeV	-0.187 ± 0.012
p_5	8.04 ± 0.67 GeV	0.095 ± 0.008

Table 6.1: Parameters for $W_j(E_p, E_j)$ extracted using jets matched in angle to b-quarks (see text), from Monte Carlo.

We parametrize the distribution of measured jet energies, E_j, as a function of the quark energies, E_p, and the difference between the parton energy and the jet energy, $W_j(\delta \equiv E_p - E_j)$ [41]. The parametrization is a sum of two Gaussians to account for both the peak of the δ distribution and its tails,

$$W_j(\delta) = \frac{1}{\sqrt{2\pi}(p_2 + p_3 p_5)} \left[e^{\frac{-(\delta - p_1)^2}{2p_2^2}} + p_3 e^{\frac{-(\delta - p_4)^2}{2p_5^2}} \right], \tag{6.2}$$

where each p_i depends linearly on E_p:

$$p_i = a_i + b_i E_p. \tag{6.3}$$

The parameters p_i are extracted with an unbinned maximum likelihood fit over N jets in a sample of simulated $t\bar{t}$ events with $M_t = 178$ GeV/c^2 which pass the event selection and contain jets whose axis is contained in a cone of $\Delta R = 0.4$ surrounding b-quarks. Jets which arise from initial or final state radiation are excluded. The log likelihood is expressed as a sum over jets:

$$-\ln L = -\sum_{k=1}^{N} \ln n(E_{p_k}) - \sum_{k=1}^{N} \ln W(E_{p_k}, E_{j_k}). \tag{6.4}$$

The first term does not depend on the parameters p_i and can be dropped from the minimization. We extract the parameters shown in Table 6.1.

To test the jet transfer function, we calculate the distribution of jet energies which result from simulated partons of known energy. The calculation for jet energies resulting

from partons with energy $E_1 < E_p < E_2$ is the integral of $n(E_j, E_p)dE_p$:

$$\int_{E_1}^{E_2} n(E_p)dE_p W(E_p, E_j). \qquad (6.5)$$

The calculation for the jet energy distribution and the difference in jet and parton energies resulting from all partons ($0 < E_p < 1$ TeV) in a simulated sample of $t\bar{t}$ with $M_t = 178$ GeV/c^2 is shown in Figure 6.1. Similar tests using slices of parton energies are shown in Figure 6.2.

The jet transfer function models the detector response to partons and should be independent of the production process. We confirm this by using $W_j(E_p, E_j)$ parametrized from $M_t = 178$ GeV/c^2 events to calculate the jet energy distribution resulting from b-quarks in Monte Carlo top decays of varied top masses. Figure 6.3 shows that the jet transfer function derived using partons from $M_t = 178$ GeV/c^2 top decays satisfactorily describes jet energies from top decays of M_t ranging from 150 GeV/c^2 through 200 GeV/c^2. The performance of the transfer functions in fully realistic simulated events is included in the measurement calibrations discussed in Chapter 9.
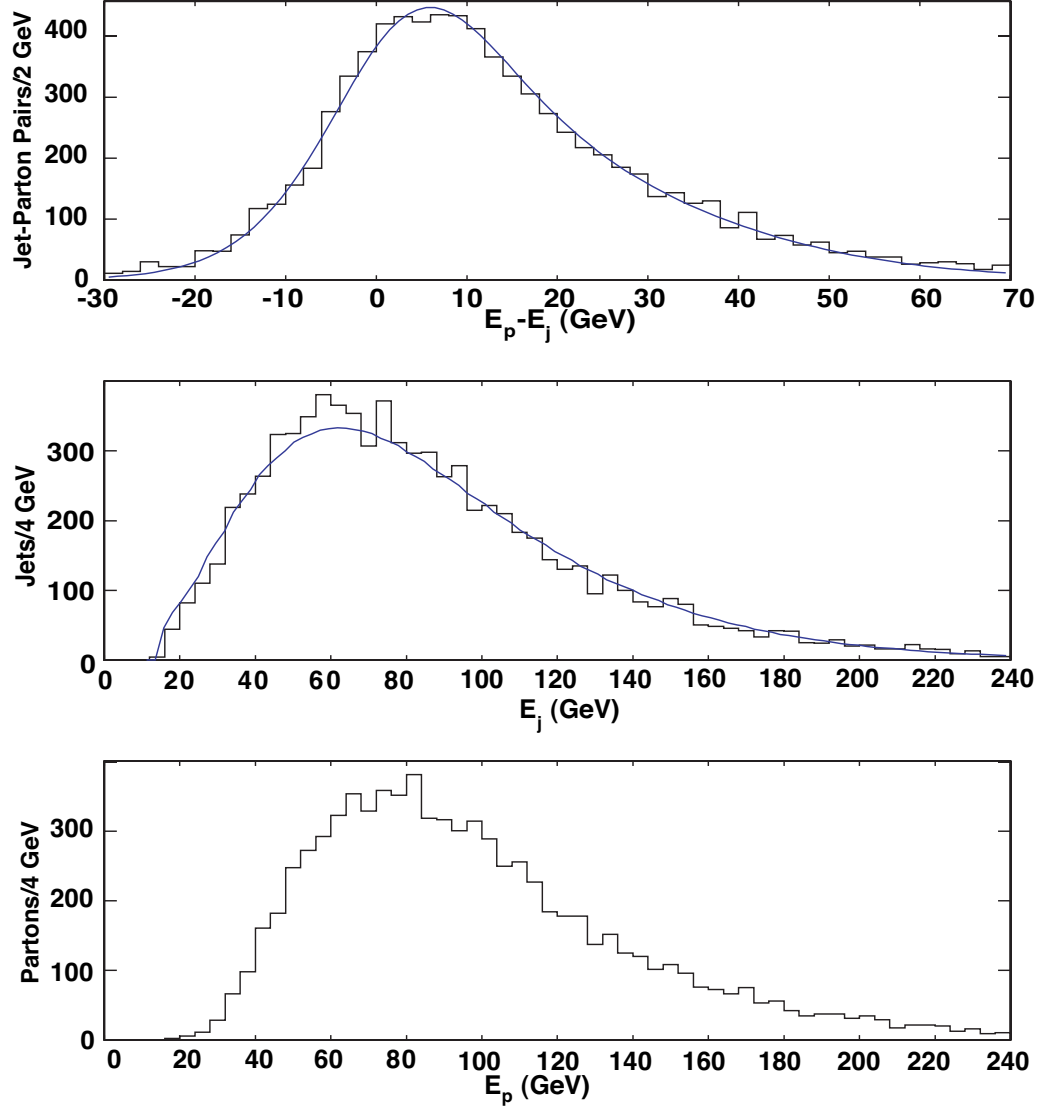
Figure 6.1: Top, difference of $E_p - E_j$ between parton and jet energy. Center, distribution of E_j of jet energy. Bottom, input distribution of parton energy E_p. Histograms are simulated events for $M_t = 178$ GeV/c^2; curves in the upper two histograms show the distributions calculated using $W(E_p, E_j)$.
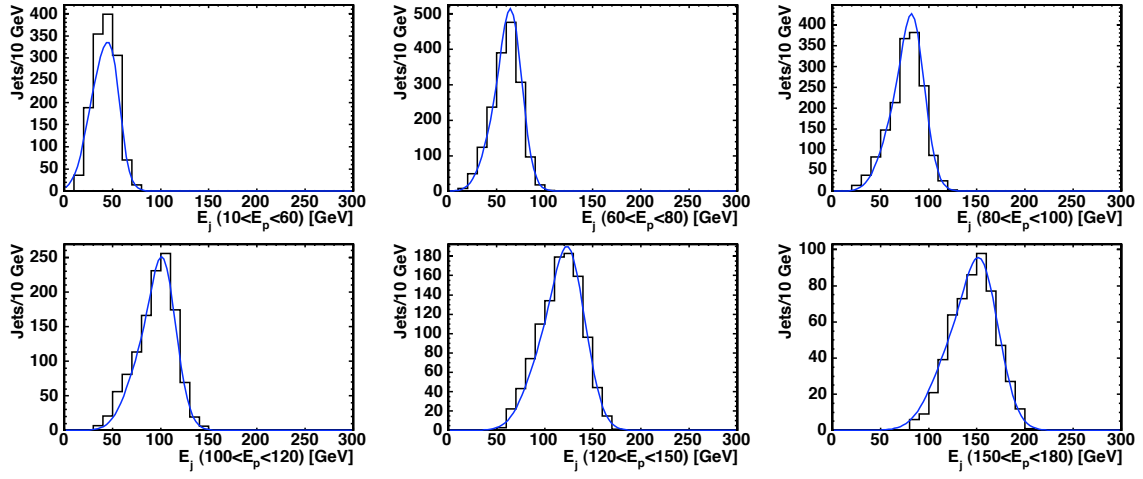
Figure 6.2: Comparison of simulated E_j with calculations from $W(E_p, E_j)$ from six ranges of E_p. Histograms are simulated events; curves show the calculated distributions using $W(E_p, E_j)$.
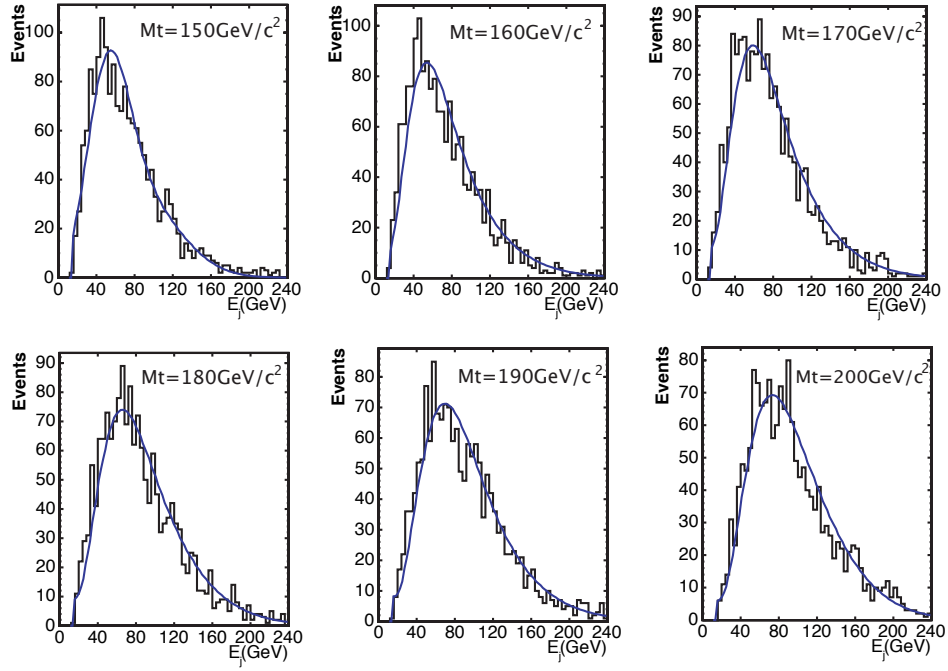
Figure 6.3: Comparison of simulated E_j with calculations from $W(E_p, E_j)$ from distributions E_p in simulated samples with $M_t = 150$, 160, 170, 180, 190, and 200 GeV/c^2. Histograms are simulated events for $M_t = 178$ GeV/c^2; lines show the calculated distributions using $W_j(E_p, E_j)$ derived using partons from $M_t = 178$ GeV/c^2.

6.2 $t\bar{t}$ p_T Transfer Functions

Often in $t\bar{t}$ events, gluon radiation in an event will result in the $t\bar{t}$ system recoiling and obtaining non-negligible p_T. Correct reconstruction of the final state would require knowledge of the $t\bar{t}$ p_T. While we cannot measure the p_T of the the $t\bar{t}$ ($p_T^{t\bar{t}}$) system in data events, we observe strong correlations between several measured quantities and $p_T^{t\bar{t}}$. Gluons resulting from radiation, if energetic enough, can result in hadronic jets being reconstructed in the event. Thus, for events with more than two jets passing our selection cuts, we can utilize the measured jet energy of sub-leading jets to form transfer functions to $p_T^{t\bar{t}}$. In Monte Carlo events, $p_T^{t\bar{t}}$ is shown to have a strong dependence on the number of jets in the event (see Figure 6.4). In addition, less energetic gluons resulting from radiation may still deposit measured energy in the hadronic calorimeter. This softer energy can be quantified using unclustered energy. The unclustered energy in an event is the total energy in an event that is measured in the calorimeter, but not clustered into an object such as a lepton or jet that is used in this measurement. The transverse components of unclustered energy can be calculated as:

$$E_{(x,y)}^{unclustered} = \sum_i (L_{i_{(x,y)}} + j_{i_{(x,y)}}) - \not{E}_{T(x,y)} \tag{6.6}$$

by subtracting the measured $\not{E}_T$ from the measured transverse energies of clustered objects passing the selection cuts outlined in Chapter 4 in an event. A comparison of the transverse unclustered energy between what is measured in the data events used in this analysis and what is predicted using Monte Carlo events is shown in Figure A.11.

For forming a transfer function for $p_T^{t\bar{t}}$, we utilize a variable U, whose transverse quantities are given by:

$$U_{(x,y)} = E_{(x,y)}^{unclustered} + \sum_{i=3}^{N_{jets}} j_{i_{(x,y)}},$$
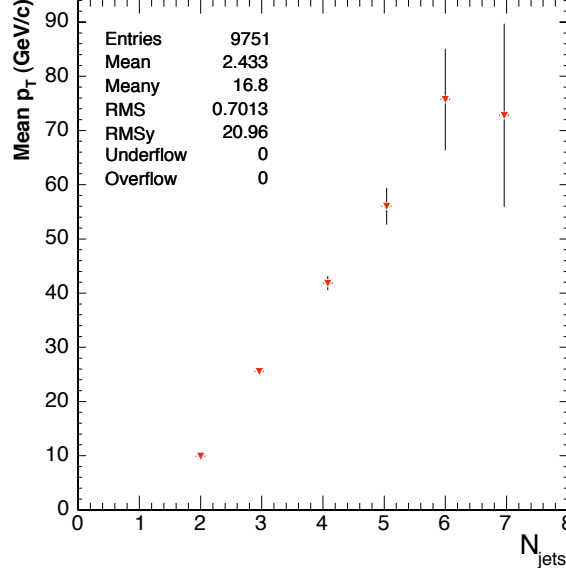
Figure 6.4: Mean $p_T^{t\bar{t}}$ for PYTHIA simulated $t\bar{t}$ events with the number of reconstructed jets ranging from two to seven or more.

or,

$$U_{(x,y)} = \sum_{1,2}(L_{i_{(x,y)}} + j_{i_{(x,y)}}) - \not{E}_{T(x,y)}, \tag{6.7}$$

where the L_i and j_i are the measured momenta of the leptons and jets in the event passing the selection cuts described in Chapter 4. Thus, for an event with exactly two jets above threshold, U reduces to the unclustered energy. The p_T transfer function is parametrized in terms of the difference between $p_T^{t\bar{t}}$ and U, $\delta_{p_T} \equiv p_T^{t\bar{t}} - U$. As with the jet transfer function, the p_T transfer function is parametrized as the sum of two Gaussians, to account for the peak and the tails of the δ_{p_T} distribution,

$$W_{p_T}(\delta_{p_T}) = \frac{1}{\sqrt{2\pi}}\left[p_0 e^{\frac{-(\delta_{p_T}-p_1)^2}{2p_2^2}} + p_3 e^{\frac{-(\delta_{p_T}-p_4)^2}{2p_5^2}}\right]. \tag{6.8}$$

The distributions of δ_{p_T} in events with only two jets passing the selection cuts and events with three or more jets are substantially different. Thus, we extract two sets of parameters for W_{p_T} and use them for each class of events. The distributions of δ_{p_T} with the extracted fits overlaid are shown in Figure 6.5. The parameters extracted are shown
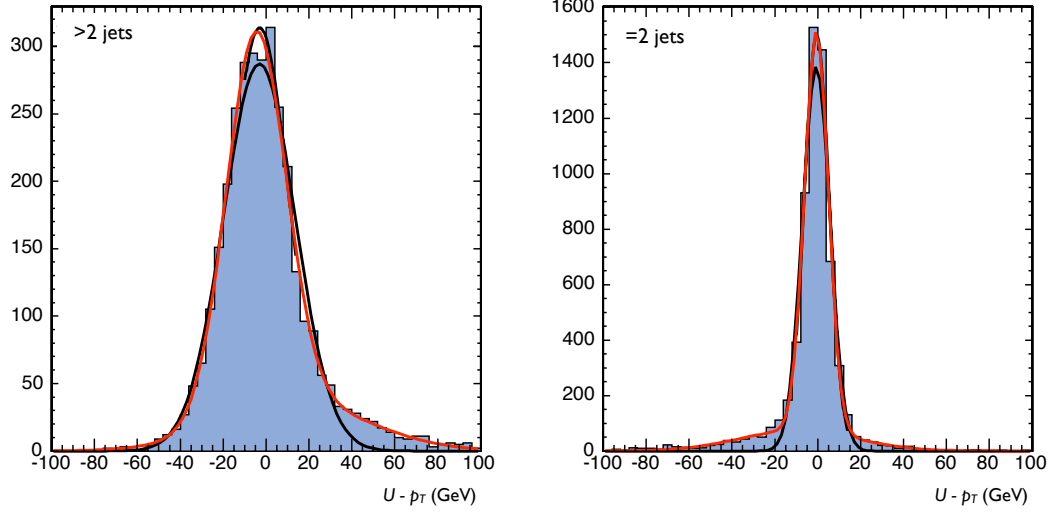
Figure 6.5: The distributions of δ_{p_T} for events with more than two jets (*right*) and exactly two jets (*left*). The extracted fits are overlaid with the individual Gaussians in black and the total fit in red.

p_i	2 jets	>2 jets
p_0	73.98	40.30
p_1	-9.351 GeV	-2.321 GeV
p_2	26.80 GeV	38.89 GeV
p_3	1443	253.6
p_4	-0.597 GeV	-7.202 GeV
p_5	5.568 GeV	14.27 GeV

Table 6.2: Parameters extracted for W_{p_T} using $t\bar{t}$ Monte Carlo events. Events with 2 jets passing selection cuts and events with more than 2 jets are considered separately.

in Table 6.2.

We form an additional transfer function which links the ϕ component of the $t\bar{t}$ momentum to the ϕ component of U. The ϕ transfer function, W_ϕ, is parametrized in terms of $\delta_\phi \equiv \phi_{t\bar{t}} - U_\phi$. As most events have U pointing opposite of the $t\bar{t}$ p_T, we parametrize this transfer function as the sum of a linear function and a Gaussian,

$$W_\phi = p_0 + p_1\delta_\phi + p_2 e^{\frac{-(\delta_\phi - p_3)^2}{2p_4^2}} . \tag{6.9}$$

As with W_{p_T}, the ϕ transfer function is also derived separately for events with exactly two jets and events with three or more jets. The distributions of δ_ϕ for these two classes

50
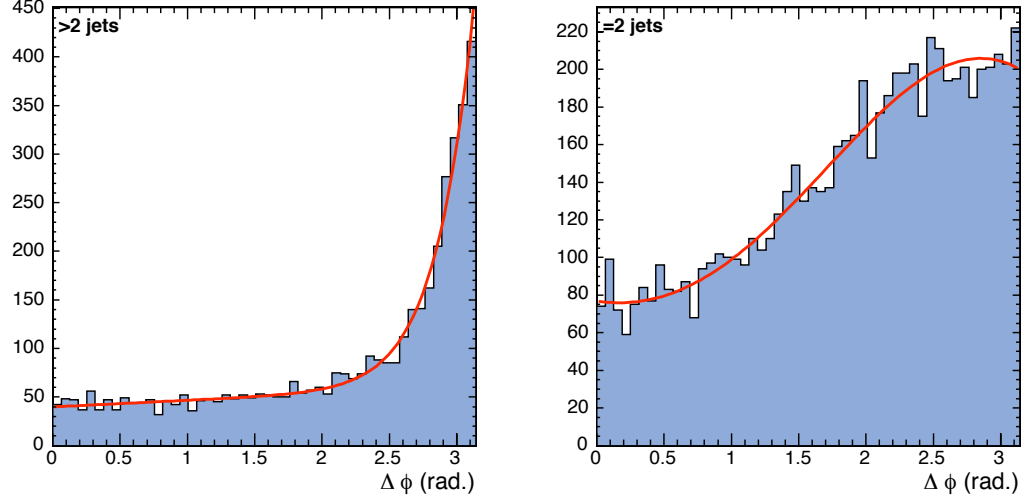
Figure 6.6: The distributions of δ_ϕ for events with more than two jets (*right*) and exactly two jets (*left*). The extracted fits are overlaid in red.

p_i	2 jets	>2 jets
p_0	86.24	37.77
p_1	13.44	6.718
p_2	170.3	5.045×10^6
p_3	2.924	11.69
p_4	1.778	1.932

Table 6.3: Parameters extracted for W_ϕ using $t\bar{t}$ Monte Carlo events. Events with 2 jets passing selection cuts and events with more than 2 jets are considered separately.

of events are shown in Figure 6.6 along with the extracted fits. The parameters extracted

are shown in Table 6.3.

CHAPTER 7

Signal Probability

The probability $P_s(\mathbf{x}|M_t)$ describes the likelihood of a measured event $\mathbf{x}$ being consistent with $t\bar{t}$ decay with a top quark pole mass of M_t. It is constructed as a convolution of the transfer functions described in the previous chapter and a leading-order matrix element for $t\bar{t}$ production and decay.

7.1 Differential Cross-Section Expression

The probability density for $q\bar{q} \to t\bar{t} \to b\ell\nu_\ell\bar{b}\ell'\nu_{\ell'}$ decays is constructed as the differential cross section, $d\sigma$, with respect to the measured event quantities, $\mathbf{x}$. The total cross section σ is written as

$$\sigma = \int \sum_{a,b} \frac{(2\pi)^4 |\mathcal{M}|^2}{4\sqrt{(q_1 \cdot q_2)^2 - m_1^2 m_2^2}} f_{\mathrm{PDF}}^a \left(\frac{q_{z_1}}{E_{\mathrm{beam}}} \right) f_{\mathrm{PDF}}^b \left(\frac{q_{z_2}}{E_{\mathrm{beam}}} \right) d\Phi_6 dq_1 dq_2, \qquad (7.1)$$

where the sum runs over incoming parton flavors, $\mathcal{M}$ is the matrix element for the process, $q_{1,2}$ and $m_{1,2}$ refer to the momenta and mass of the incoming partons, f_{PDF} are the parton distribution functions for flavor a, and the integration is over the phase space for the six final state particles as well as the longitudinal momenta of the incoming particles.

The matrix element [44, 45] has the form

$$|\mathcal{M}|^2 = \frac{g_s^4}{9} F\bar{F} \left((2 - \beta^2 s_{qt}^2) - X_{sc} \right), \qquad (7.2)$$

where β is the top-quark velocity in the $q\bar{q}$ rest frame, X_{sc} contains terms describing spin correlations between the top quarks, g_s is the strong coupling constant ($g_s^2/4\pi = \alpha_s$), s_{qt} is the sine of the angle between the incoming parton and the top quark, and F and $\overline{F}$ are the propagators for the top and the anti-top respectively. We drop the spin correlation term X_{sc} as it is negligible. The top-quark propagator and decay terms are given by

$$F = \frac{g_w^4}{4}\left[\frac{m_t^2 - m_{\ell\nu}^2}{(m_t^2 - M_t^2)^2 + (M_t\Gamma_t)^2}\right]\left[\frac{m_t^2(1 - \hat{c}_{\ell b}^2) + m_{\ell\nu}^2(1 + \hat{c}_{\ell b})^2}{(m_{\ell\nu}^2 - M_W^2)^2 + (M_W\Gamma_W)^2}\right], \qquad (7.3)$$

where m_t is the invariant mass of the t-quark decay products and $\hat{c}_{ij}$ is the cosine of the angle between particles i and j in the W rest frame. The M_t, Γ_t, M_W, Γ_W are the pole masses and widths of the top-quark and W-boson, and g_w[1] is the weak coupling constant. The top width, Γ_t [46], is a function of M_t, M_W and Γ_W as described by the standard model to leading order:

$$\Gamma_t = \frac{G_F M_t^3 |V_{tb}|^2}{8\pi\sqrt{2}}\left[1 - 3\frac{M_W^4}{M_t^4} + 2\frac{M_W^6}{M_t^6} + \cdots\right], \qquad (7.4)$$

where G_F is the Fermi coupling constant and $|V_{tb}|$ is a mixing term from the CKM matrix. $\overline{F}$ is given by the same expression as Eq. 7.3, replacing the terms for t and its decay products with $\bar{t}$ and its decay products.

While approximately 15% of $t\bar{t}$ pairs in $p\bar{p}$ collisions at $\sqrt{s} = 1.96$ TeV are produced in gluon-gluon fusion ($gg \to t\bar{t}$) [15], our studies have shown that this term can be excluded from the matrix element with very little loss of sensitivity to the measurement[2].

To evaluate the differential cross section with respect to observed quantities, $\frac{d\sigma}{d\mathbf{x}}$, we introduce conditional probability terms that relate the observed quantities to the parton level variables and subsequently integrate over unconstrained parton-level quantities, as described above. In order to make the computation associated with these integrals

---

[1]$G_F = \sqrt{2}g_w^2/8M_W^2$

[2]Additionally, we can verify that the exclusion of the gg term introduces no bias by using simulated events with varied initial state content and using only the qq matrix element. We observe negligible variation in the measured mass amongst samples consisting of 0%, 5%, and 15% gg events.

tractable, a series of assumptions, listed in Chapter 5, are made regarding the transfer between parton level quantities and the observables. These assumptions are enforced as delta functions in the expression for the differential cross section.

The differential cross section is given by

$$\frac{d\sigma}{d\mathbf{x}} = \left(\frac{1}{(2\pi)^3}\right)^6 \int \sum_{a,b} |\mathcal{M}(q_1^i, q_2^j \to \ell_1, \nu_1, p_1, \ell_2, \nu_2, p_2)|^2 (2\pi)^4 \delta^4 \left(\sum_{k=1,2} (q_k - \ell_k - \nu_k - p_k)\right)$$

$$\times \, \delta(q_{x_1}) \, \delta(q_{y_1}) \, dq_{x_1} \, dq_{y_1} \delta(q_{x_2}) \, \delta(q_{y_2}) \, dq_{x_2} \, dq_{y_2} \frac{(2\pi)^4 f_{\text{PDF}}^a(q_{z_1}^i/E_{\text{beam}}) \, f_{\text{PDF}}^b(q_{z_2}^j/E_{\text{beam}}) dq_1^i \, dq_2^j}{4\sqrt{(q_1 \cdot q_2)^2 - m_{q_1}^2 m_{q_2}^2}}$$

$$\times \, \delta^3(\ell_1 - L_1) \, \delta^3(\ell_2 - L_2) \frac{d^3\ell_1}{2E_{\ell_1}} \frac{d^3\ell_2}{2E_{\ell_2}} \delta(\theta_{p_1} - \theta_{j_1}) \, \delta(\theta_{p_2} - \theta_{j_2}) \delta(\phi_{p_1} - \phi_{j_1}) \, \delta(\phi_{p_2} - \phi_{j_2})$$

$$\times \, W(E_{p_1}, E_{j_1}) W(E_{p_2}, E_{j_2}) W_{p_T}(p_T^{t\bar{t}}, U) W_\phi(\phi_{t\bar{t}}, U_\phi) \frac{d^3p_1}{2E_{p_1}} \frac{d^3p_2}{2E_{p_2}} \frac{d^3\nu_1}{2E_{\nu_1}} \frac{d^3\nu_2}{2E_{\nu_2}} dp_x^{t\bar{t}} dp_y^{t\bar{t}}.$$

$$(7.5)$$

The sum is over possible incoming parton flavors. The term $1/4\sqrt{(q_1 \cdot q_2)^2 - m_{q_1}^2 m_{q_2}^2}$ reduces to $f_{\text{flux}}(q_{z_1}, q_{z_2}) = 1/2q_{z_1}q_{z_2}$ with the assumption that the parton mass is small in comparison to the longitudinal momentum.

7.2 Phase Space Transformation and Integration

We integrate over the lepton momenta, initial parton momenta, intermediate top and W momenta, angular components of the b-partons, the x and y components of the momentum of the $t\bar{t}$ system, and the six components of neutrino momenta.

In order to efficiently integrate over the parton-level variables, we perform a transformation which splits the original phase space into subspaces and introduces the equivalent number of extra variables and integrations. We introduce invariant masses that correspond to intermediate t and $\bar{t}$ quarks and W-bosons. Each additional integration over an invariant mass of the intermediate particle has a corresponding δ-function in squared invariant mass, and each intermediate particle four-momentum has corresponding δ^4-

function for the momentum conservation at the intermediate vertex.

The expression of the integrand is written in terms of the momenta of the final state particles, $b\ell\nu_\ell\bar{b}\ell'\bar{\nu}'_\ell$. Integration over the t and W invariant masses (m_{t_i} and m_{W_i}) requires expressing the neutrino momenta in terms of these invariant masses. These two sets of variables are related by a system of six coupled quadratic equations written in terms of the final-state momenta and the W-boson momenta (W_i) and derived from expressions in the δ functions.

$$
\begin{aligned}
m_{t_1}^2 &= (p_1 + W_1)^2 \\
m_{t_2}^2 &= (p_2 + W_2)^2 \\
m_{W_1}^2 &= (\ell_1 + \nu_1)^2 \\
m_{W_2}^2 &= (\ell_2 + \nu_2)^2 \\
(p_1 + \ell_1 + \nu_1 + p_2 + \ell_2 + \nu_2)_x &= p_x^{t\bar{t}} \\
(p_1 + \ell_1 + \nu_1 + p_2 + \ell_2 + \nu_2)_y &= p_y^{t\bar{t}}
\end{aligned}
\tag{7.6}
$$

We rewrite these equations as a single fourth-order polynomial and find the solutions numerically using the Sturm Sequence approach [47]. The transformation between the phase space for neutrino momenta and invariant masses is not one-to-one due to the non-linearity of the relations. Multiple neutrino solutions may exist for specific invariant masses; such solutions are therefore summed. Other invariant masses may have no corresponding region of neutrino phase space and therefore no solutions and no contribution to the total probability. A test of the neutrino solutions is shown in Figure 7.1.

Finally, the transformation of variables requires the inclusion of a Jacobian term, J, which has the form:

$$
J = \left| \frac{\partial f_i}{\partial \nu_{(1,2)(x,y,z)}} \right|
\tag{7.7}
$$
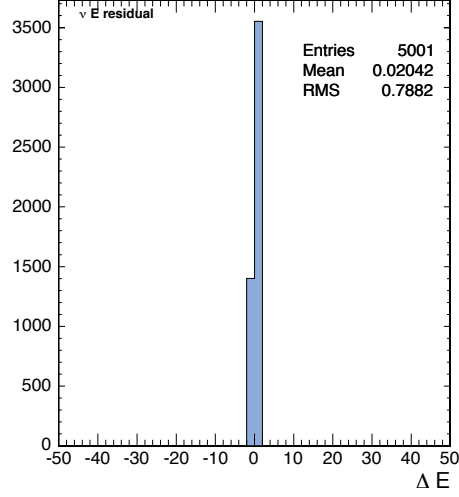
Figure 7.1: A plot of the difference between the true neutrino energy and neutrino energy as solved from equation 7.6 in simulated events using parton-level quantities.

The f_i are the functions of neutrino momenta that occur inside δ-functions:

$$f_1 = \left((L_1 + \nu_1 + p_1)_x + (L_2 + \nu_2 + p_2)_x - p_x^{t\bar{t}} \right)$$

$$f_2 = \left((L_1 + \nu_1 + p_1)_y + (L_2 + \nu_2 + p_2)_y - p_y^{t\bar{t}} \right)$$

$$f_3 = \left((L_1 + \nu_1 + p_1)^2 - M_{t_1}^2 \right)$$

$$f_4 = \left((L_2 + \nu_2 + p_2)^2 - M_{t_2}^2 \right)$$

$$f_5 = \left((L_1 + \nu_1)^2 - M_{W_1}^2 \right)$$

$$f_6 = \left((L_2 + \nu_2)^2 - M_{W_2}^2 \right)$$

(7.8)

The determinant has the form:

$$\begin{vmatrix} 1 & 0 & J_{3x} & 0 & J_{5x} & 0 \\ 0 & 1 & J_{3y} & 0 & J_{5y} & 0 \\ 0 & 0 & J_{3z} & 0 & J_{5z} & 0 \\ 1 & 0 & 0 & J_{4x} & 0 & J_{6x} \\ 0 & 1 & 0 & J_{4y} & 0 & J_{6y} \\ 0 & 0 & 0 & J_{4z} & 0 & J_{6z} \end{vmatrix}$$

56

that evaluates to:

$$J = |J_{3z}J_{4z}J_{5y}J_{6x} - J_{3y}J_{4z}J_{5z}J_{6x} - J_{3z}J_{4z}J_{5x}J_{6y}+$$

$$+ J_{3x}J_{4z}J_{5z}J_{6y} + J_{3z}J_{4y}J_{5x}J_{6z} - J_{3z}J_{4x}J_{5y}J_{6z}+ \qquad (7.9)$$

$$+ J_{3y}J_{4x}J_{5z}J_{6z} - J_{3x}J_{4y}J_{5z}J_{6z}|$$

with:

$$J_{3x} = \frac{\partial f_3}{\partial \nu_{1x}} = \frac{2(L_1^0 + p_1^0)\nu_{1x}}{\sqrt{\nu_{1x}^2 + \nu_{1y}^2 + \nu_{1z}^2}} - 2(L_{1x} + p_{1x})$$

$$J_{3y} = \frac{\partial f_3}{\partial \nu_{1y}} = \frac{2(L_1^0 + p_1^0)\nu_{1y}}{\sqrt{\nu_{1x}^2 + \nu_{1y}^2 + \nu_{1z}^2}} - 2(L_{1y} + p_{1y})$$

$$J_{3z} = \frac{\partial f_3}{\partial \nu_{1z}} = \frac{2(L_1^0 + p_1^0)\nu_{1z}}{\sqrt{\nu_{1x}^2 + \nu_{1y}^2 + \nu_{1z}^2}} - 2(L_{1z} + p_{1z})$$

$$J_{4x} = \frac{\partial f_4}{\partial \nu_{2x}} = \frac{2(L_2^0 + p_2^0)\nu_{2x}}{\sqrt{\nu_{2x}^2 + \nu_{2y}^2 + \nu_{2z}^2}} - 2(L_{2x} + p_{2x})$$

$$J_{4y} = \frac{\partial f_4}{\partial \nu_{2y}} = \frac{2(L_2^0 + p_2^0)\nu_{2y}}{\sqrt{\nu_{2x}^2 + \nu_{2y}^2 + \nu_{2z}^2}} - 2(L_{2y} + p_{2y})$$

$$J_{4z} = \frac{\partial f_4}{\partial \nu_{2z}} = \frac{2(L_2^0 + p_2^0)\nu_{2z}}{\sqrt{\nu_{2x}^2 + \nu_{2y}^2 + \nu_{2z}^2}} - 2(L_{2z} + p_{2z})$$

$$J_{5x} = \frac{\partial f_5}{\partial \nu_{1x}} = \frac{2(L_1^0\nu_{1x})}{\sqrt{\nu_{1x}^2 + \nu_{1y}^2 + \nu_{1z}^2}} - 2L_{1x} \qquad (7.10)$$

$$J_{5y} = \frac{\partial f_5}{\partial \nu_{1y}} = \frac{2(L_1^0\nu_{1y})}{\sqrt{\nu_{1x}^2 + \nu_{1y}^2 + \nu_{1z}^2}} - 2L_{1y}$$

$$J_{5z} = \frac{\partial f_5}{\partial \nu_{1z}} = \frac{2(L_1^0\nu_{1z})}{\sqrt{\nu_{1x}^2 + \nu_{1y}^2 + \nu_{1z}^2}} - 2L_{1z}$$

$$J_{6x} = \frac{\partial f_6}{\partial \nu_{2x}} = \frac{2(L_2^0\nu_{2x})}{\sqrt{\nu_{2x}^2 + \nu_{2y}^2 + \nu_{2z}^2}} - 2L_{2x}$$

$$J_{6y} = \frac{\partial f_6}{\partial \nu_{2y}} = \frac{2(L_2^0\nu_{2y})}{\sqrt{\nu_{2x}^2 + \nu_{2y}^2 + \nu_{2z}^2}} - 2L_{2y}$$

$$J_{6z} = \frac{\partial f_6}{\partial \nu_{2z}} = \frac{2(L_2^0\nu_{2z})}{\sqrt{\nu_{2x}^2 + \nu_{2y}^2 + \nu_{2z}^2}} - 2L_{2z}$$

The final form of the expression is

$$\frac{d\sigma}{d\mathbf{x}} = \left(\frac{1}{(2\pi)^3}\right)^6 (2\pi)^2 \int \sum_{a,b} \frac{|\mathcal{M}|^2}{2E_{\text{beam}}^2} \frac{J^{-1}}{E_{\nu_1} E_{\nu_2} E_{L_1} E_{L_2}} \frac{|p_1|^2 \sin\theta_{p_1} d|p_1|}{2E_{p_1}} \frac{|p_2|^2 \sin\theta_{p_2} d|p_2|}{2E_{p_2}}$$

$$\times f_{\text{PDF}}^a\left(\frac{q_{z_1}}{E_{\text{beam}}}\right) f_{\text{PDF}}^b\left(\frac{q_{z_2}}{E_{\text{beam}}}\right) f_{\text{flux}}(q_{z_1}, q_{z_2}) W(E_{p_1}, E_{j_1}) \, W(E_{p_2}, E_{j_2})$$

$$\times W_{p_T}(p_T^{t\bar{t}}, U) W_\phi(\phi_{t\bar{t}}, U_\phi) \, |p_T^{t\bar{t}}| \, dp_T^{t\bar{t}} \, d\phi_{t\bar{t}} M_{t_1} \, M_{t_2} \, M_{W_1} \, M_{W_2} \, dM_{t_1} \, dM_{t_2} \, dM_{W_1} \, dM_{W_2},$$

$$(7.11)$$

where the remaining integrations are over the invariant masses of the t quarks and the W bosons, the magnitude and ϕ direction of $p_T^{t\bar{t}}$, and the magnitude of the b-quark momenta.

The cross section as a function of M_t is expressed as a eight-dimensional integral; this integration is performed numerically using the VEGAS [48] algorithm as implemented in the GNU Scientific Library [49]. As we do not have *a priori* knowledge of which jet and which lepton came from the same top quark, we evaluate the final probability for each of the two possible combinations and sum the two resulting probabilities.

7.3   Tests of the Signal Probability

We can test the signal probability using simulated events using increasing levels of complexity.

We begin with simulated $p\bar{p} \to t\bar{t}$ events generated with PYTHIA in which all of the parton-level information from the hard scattering and subsequent decay is known. Evaluating the matrix element in Equation 7.2 for these events as a function of top quark pole mass results in sharp peaks at the invariant mass of each of the top quarks in the event, as shown in Figure 7.2.

We can then discard information not present in data events (such as neutrino momenta) and apply Gaussian smearing to b-quark energies to simulate jets. We then evaluate the
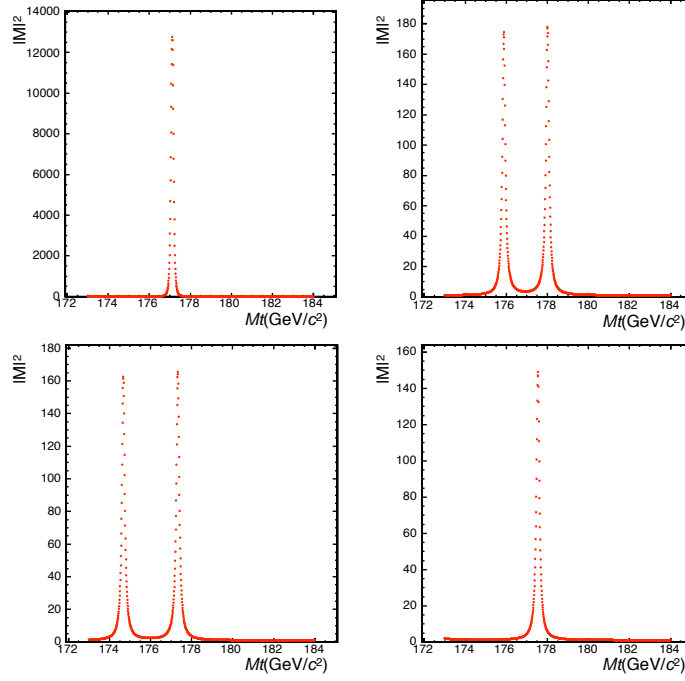
Figure 7.2: Evaluation of the $t\bar{t}$ matrix element using parton-level information from Monte Carlo events.

integral in Equation 7.11, resulting in curves as shown in Figure 7.3. The resulting curves are smooth, indicating that the calculation is well-behaved, and peak roughly in the region corresponding to the true invariant masses.

As individual events are not very illustrative, we then perform pseudo-experiments with ensembles of simulated events. The mass is extracted from each pseudo-experiment using the same method as is used with data events (see Chapter 9). The distribution of pulls of each pseudo-experiment gives a measure of how well the statistical uncertainty is estimated. The pull of a pseudo-experiment is defined as

$$p = \frac{M_t^{meas} - M_t^{true}}{\sigma_{M_t}}, \tag{7.12}$$

where M_t^{meas} is the mass measured in each pseudo-experiment, M_t^{true} is the input mass and σ_{M_t} is the measured statistical uncertainty in each pseudo-experiment. For a set of pseudo-experiments where the result is unbiased and the error is estimated correctly, the
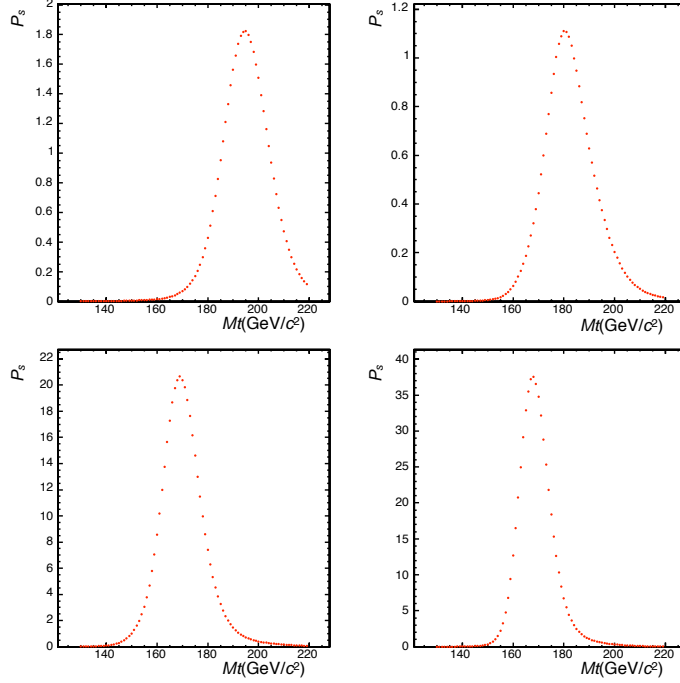
Figure 7.3: Evaluation of P_s using Monte Carlo events with smeared partons.

Events	True Mass	Mean Mass	Mass RMS	Pull Width
Smeared Parton	178	176.7 ± 1.5	5.5	1.04 ± 0.04
Fully Simulated	178	178.3 ± 1.0	8.7	1.14 ± 0.04

Table 7.1: Results from pseudo-experiments using both smeared parton-level quantities and fully simulated events and the full signal probability to extract the measured mass.

pulls are expected to fall in a gaussian distribution with a mean of 0 and a width of 1.0.

We perform pseudo-experiments using parton level quantities with smeared b-quarks as above and also using events passed through a full detector simulation. The results of these pseudo-experiments are shown in Table 7.1. We note that the pull widths of the fully simulated events, which we expect to be similar to events observed in the data, indicate the statistical uncertainty is underestimated by approximately 15%. This is due to the violation of the assumptions listed in Chapter 5 in these events. These assumptions are all held in smeared parton-level events, where the pull width is consistent with 1.0. This indicates the method correctly estimates the statistical uncertainty in the class of

events where all assumptions made are held. We can study the effect of each of these assumptions by performing pseudo-experiments where we control the degree to which the assumptions are violated in the events used.

7.3.1 Jet-Parton Assignment

In samples of simulated events which pass selection requirements, 70% of events contain two reconstructed jets whose axes lie within a cone of $\Delta R < 0.7$ of unique b-quarks from the top quark decay. Monte Carlo experiments using this subset of events have a significantly smaller pull width, 1.06 ± 0.04. This suggests that events in which the assumption of correspondence between jets and b-quarks is violated contribute significantly to non-unit pull widths.

7.3.2 Lepton Resolution

Though lepton energies are well measured by CDF, electrons and muons are measured by different subdetectors. The energy of electrons at high E_T is very well measured by the calorimeter:

$$\frac{\sigma_E}{E} = \frac{13.5\%}{\sqrt{E(\text{GeV})}} \oplus 2.0\%. \tag{7.13}$$

The momentum of muons is measured by the central tracker, whose resolution begins to degrade at large p_T:

$$\frac{\sigma_{p_T}}{p_T} = 0.0011 \cdot p_T(\text{GeV}/c). \tag{7.14}$$

Monte Carlo experiments formed using events in which jets are matched well to b-quarks and events containing only electrons have a pull width of 0.98 ± 0.04. Similar Monte Carlo experiments using only muons have a pull width of 1.03 ± 0.04, indicating that muon momentum resolution contributes to pull widths greater than unity. Electrons and
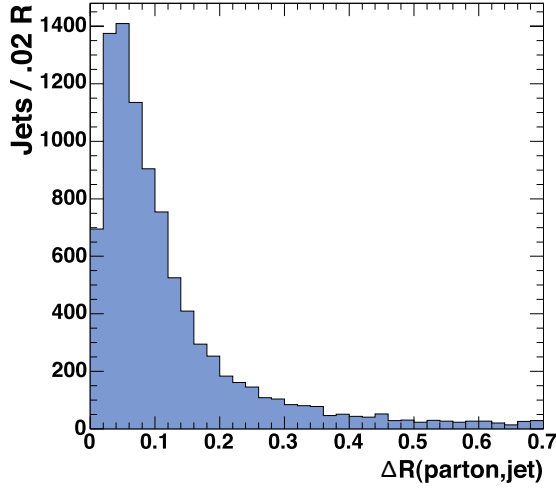
Figure 7.4: Angular distance, ΔR, between a reconstructed jet and the closest b-quark in $t\bar{t}$ events simulated with HERWIG. The width of the distribution demonstrates the angular resolution. 20% of jet-parton pairs have $\Delta R \geq 0.7$ (not shown), coming from jets with no corresponding b-quark.

muons which arise from $W \to \tau\nu_\tau$ decays are not well described by the matrix-element so they contribute to the growth in pull width as well.

7.3.3 Jet Angle Resolution

The jet angle resolution is finite, though it is significantly more precise than the jet energy resolution. Figure 7.4 shows the angular distance, ΔR, between reconstructed jets and the closest b-quarks in fully simulated $t\bar{t}$ events passing the selection criteria described in Chapter 4. Jets which are not matched to either of the b-quarks from top decay (no b-quark within $\Delta R < 0.7$) are likely due to initial state radiation, as described above.

To isolate the effect of the jet-angle resolution, we examine a subset of events from a fully simulated sample with $M_t = 178$ GeV/c^2. To remove the effects of lepton resolution and jet-parton matching as isolated above, we require well measured leptons ($p_T^{lepton} - p_T^{reconstructed} < 2$ GeV/c) and matched jets ($\Delta R < 0.4$). Events of this type have a negligible rate of jet-parton misassignment. Monte Carlo experiments with this subset of

events have a pull width of 1.04 ± 0.04, consistent with experiments described above which use only electrons and matched jets. Further tightening the ΔR requirement reduces the pull width to 0.97 ± 0.04.

As we observe the underestimation of the statistical uncertainty in fully simulated events to be constant as a function of input top quark mass, we can apply a constant scale factor to the measured uncertainty. This procedure is described in Chapter 9.

CHAPTER 8

Background Probabilities

We calculate the per-event differential cross section for the three largest sources of background: the $Z/\gamma^* + 2$ jet process (Zjj) where the Z decays directly to electrons or muons, the $WW + 2$ jet process $(WWjj)$ and the $W + 3$ jet process $(Wjjj)$ where one jet is misidentified as a lepton. WZ with associated jets and $Z \to \tau\tau$ with two jets have a small overall contribution to the sample and are not directly modeled.

8.1 Matrix Element Evaluation

Unlike top pair production, the major background processes can not be well described using a small number of diagrams. This is primarily due to the fact that more diagrams are needed to describe the presence of hard jets in these background events. In addition, there is no closed-form expression for the QCD processes which dominate the jet production in these background events.

We therefore adapt routines from the ALPGEN Monte Carlo generator, which make effective approximations to evaluate the matrix elements for these processes. While generators such as COMPHEP [50] and MADGRAPH [51] provide generation based directly on the explicit evaluation of the Feynman diagrams, final states with more than a single jet result in the calculation becoming unwieldy and slow.

The ALPGEN routines are a function of the spin and color configurations of the initial and final state partons as well as their momenta. While it is computationally prohibitive to rigorously sum over each of the possible configurations, it is possible to employ statistical sampling to numerically evaluate the average matrix element, $\mathcal{M}$. Figure 8.1 shows the distribution of $|\mathcal{M}|^2$ in generated events using sums of a specific number of terms; it is clear that the matrix element calculation is sensitive to the configuration and that it converges fairly rapidly.

We sample spin and color configurations until the sum has converged, satisfying the criteria

$$\frac{RMS(|\mathcal{M}|^2)}{Mean(|\mathcal{M}|^2)\sqrt{N}} < \epsilon \tag{8.1}$$

where ϵ is the convergence tolerance, set to $\epsilon = 0.25$ for these calculations, and N is the number of terms summed over.

The calculation of the matrix element is well behaved; as an example, Figure 8.2 shows the variation of $|\mathcal{M}_{Zjj}|^2$ with the invariant mass of the lepton pair in $Z \to \ell\ell$ events. It shows the expected strong peak at $M_{ll} = M_Z$.

The final measurement is calibrated using fully realistic Monte Carlo events, which will incorporate the effects of these approximations.

8.2 $Z/\gamma^* + 2$ jets

We employ the set of assumptions as described in Chapter 5 and use transfer functions as defined and derived in Chapter 6 to connect the parton-level quantities to observed quantities. We integrate over the unknown p_T which arises from additional softer jets and unclustered energy. We express this as r_x and r_y, components of the recoil in the x and y axes, respectively. We integrate over $dr_x dr_y$ using uncorrelated Gaussian priors in x
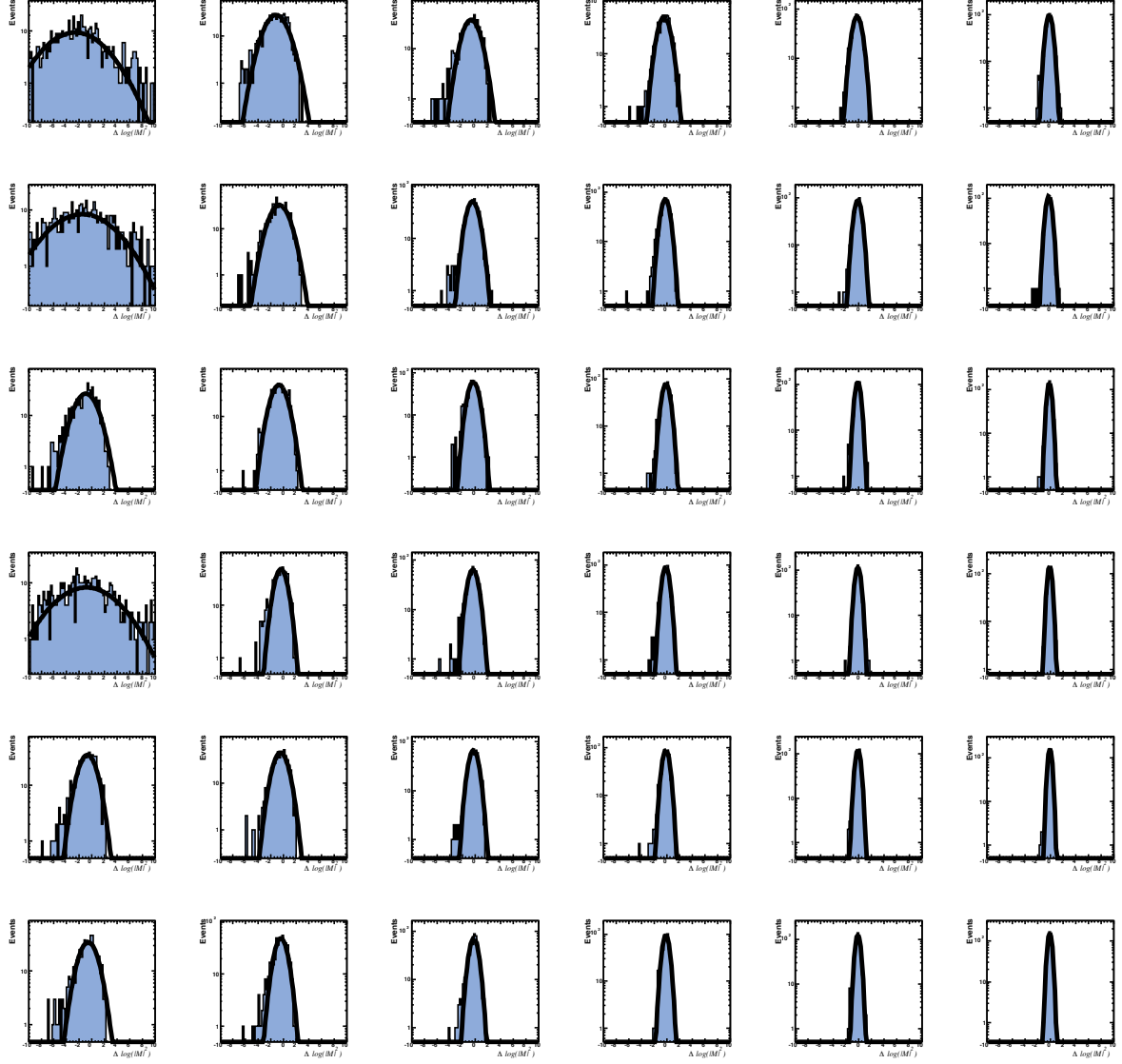
Figure 8.1: Variation in $\log(|M|^2)$ with increasing number of terms in the spin and color sum. From top, moving downwards, the number of spin terms sampled increases by powers of 2 from 1 to 32. From left, moving right, the number of color terms sampled increases by powers of 2 from 1 to 32.
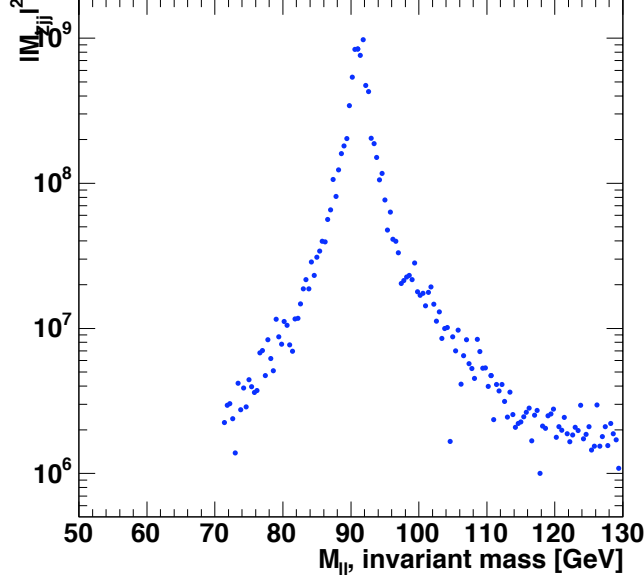
Figure 8.2: Variation of the squared matrix element for $p\bar{p} \to Z(\to ll) + 2$ jets as a function of the leptonic pair invariant mass.

and y with widths of 12 GeV/c^2, $f_{UTF}(r_x, r_y)$, as extracted from simulated samples. The differential cross section can be expressed as

$$
\begin{aligned}
\frac{d\sigma_{Zjj}}{d\mathbf{x}} =& \frac{1}{(2\pi)^8} \frac{1}{16^2} \int \sum_{i,j} dr_x dr_y f_{UTF}(r_x, r_y) \frac{f_{\text{PDF}}^i(q_{z_1}/E_{\text{beam}}) \, f_{\text{PDF}}^j(q_{z_2}/E_{\text{beam}})}{E_{L_1} E_{L_2} E_{p_1} E_{p_2}} \\
& \times \frac{|\mathcal{M}|^2}{2} \frac{W(E_{p_1}, E_{j_1}) \, W(E_{p_2}, E_{j_2}) \, |p_1|^2 \, |p_2|^2}{|q_{z_1} q_{z_2}| |\sin(\phi_{j_1} - \phi_{j_2})|},
\end{aligned}
\tag{8.2}
$$

where p_1, p_2 are the four-momenta of the final state partons which lead to creation of extra jets, L_1, L_2 are the four-momenta of the final state leptons, and q_1, q_2 are the four-momenta of incoming partons.

To test the performance of the Zjj probability, we evaluate it on simulated $t\bar{t}$ and Drell-Yan events which have passed the DIL selection outlined in Chapter 4. While the kinematic cuts sculpt both samples so that they are nearly identical kinematically, visible discrimination between the two can be observed, as seen in Figure 8.3.
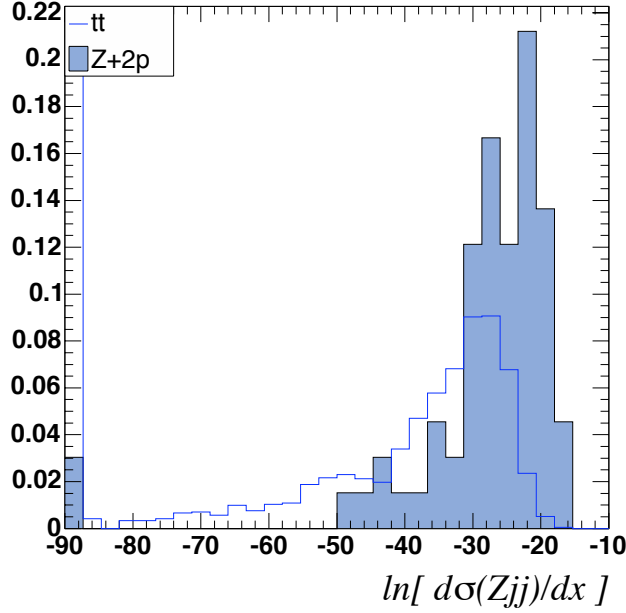
Figure 8.3: Evaluation of the Zjj probability for fully reconstructed Z and $t\bar{t}$ events, after selection is applied.

8.3 $WW + 2$ jets

The production of W pairs with associated jets is modeled in a similar fashion. We make the assumptions listed in Chapter 5 and in addition assume that the p_T of the system is 0. We choose to transform the phase-space by introducing the invariant masses of the intermediate W bosons. We express all the parton variables except the neutrino momenta in spherical coordinates. Integrating over delta functions for lepton energy, jet angles, and total conservation of momentum gives

$$
\begin{aligned}
\frac{d\sigma_{WWjj}}{d\mathbf{x}} =& \frac{1}{(2\pi)^{16}} \int \sum_{a,b} \frac{|\mathcal{M}|^2}{2E_{\text{beam}}^2} \frac{|p_1|^2 \sin\theta_{p_1} d|p_1|}{2E_{p_1}} \frac{|p_2|^2 \sin\theta_{p_2} d|p_2|}{2E_{p_2}} \frac{J^{-1}}{E_{\nu_1} E_{\nu_2} E_{L_1} E_{L_2}} \\
& \times f_{\text{PDF}}^a\left(\frac{q_{z_1}}{E_{\text{beam}}}\right) f_{\text{PDF}}^b\left(\frac{q_{z_2}}{E_{\text{beam}}}\right) f_{\text{flux}}(q_{z_1}, q_{z_2}) W(E_{p_1}, E_{j_1})\, W(E_{p_2}, E_{j_2}) \qquad (8.3) \\
& \times M_{W_1}\, M_{W_2}\, dM_{W_1}\, dM_{W_2} d\nu_{1z} d\nu_{2z},
\end{aligned}
$$

where L_1, L_2 are the measured four-momenta , ℓ_1, ℓ_2 are the parton-level four-momenta of the final state leptons, ν_1, ν_2 are the four-momenta of the final state neutrinos, p_1, p_2 are the four-momenta of the final state partons that lead to creating extra jets, and q_1, q_2 are the four-momenta of the incoming partons. The sum runs over the incoming parton flavors.

The final integration is performed over the momenta of the partons which lead to jet production, the W boson invariant masses, and the z components of neutrino momenta. Transformation of the space requires solving a coupled system of equations to express the neutrino energies in terms of the W masses and the evaluation of a Jacobian, J, similar to the signal probability.

An evaluation of the ALPGEN matrix element for $WWjj$ is shown in Figure 8.4 (*left*) using generated, parton-level events for both $WWjj$ and $t\bar{t}$. We also evaluate the $WWjj$ probability on simulated events that have passed final dilepton selections for the DIL sample. As with the Zjj case, the event selection results in the passing background events being very similar to $t\bar{t}$ kinematically. There is still, however, visible discrimination between $WWjj$ events and $t\bar{t}$ events using the $WWjj$ probability calculation, as seen in Figure 8.4 (*right*).

8.4 Fakes

Events in which a jet is misidentified as a lepton can be modeled with the process $p\bar{p} \rightarrow Wjjj \rightarrow l\nu jjj$. Using this process as the basis for the model, we sum over the possibility that either lepton is a fake originating from a jet:

$$P_{fake} = P_{Wjjj}(j_1, j_2, l_1, [l_2 \rightarrow j_3]) + P_{Wjjj}(j_1, j_2, [l_1 \rightarrow j_3], l_2). \tag{8.4}$$

Making the assumptions listed in Chapter 5 and in addition assuming that the p_T of

Figure 8.4: *Left*: Evaluation of the squared matrix element for $p\bar{p} \to WW(\to l\nu l\nu) + 2$ jets for parton-level $t\bar{t}$ and $WW + 2p$ events. *Right*: Evaluation of the $WWjj$ probability for WW and $t\bar{t}$ events in fully simulated events, after selection has been applied.

the system is 0, and integrating over all delta functions gives

$$\frac{d\sigma_{Wjjj}}{d\mathbf{x}} = \int \sum_{a,b} \frac{|\mathcal{M}|^2}{2} \frac{d|p_1|d|p_2|d|p_3|d\nu_z}{(2\pi)^8 32 E_L E_\nu E_{p_1} E_{p_2} E_{p_3}} W(E_{p_1}, E_{j_1}) W(E_{p_2}, E_{j_2}) W(E_{p_3}, E_{j_3})$$

$$\times |p_1|^2 |p_2|^2 |p_3|^2 \sin\theta_{j_1} \sin\theta_{j_2} \sin\theta_{j_3} f_{\text{PDF}}^a\left(\frac{q_{z_1}}{E_{\text{beam}}}\right) f_{\text{PDF}}^b\left(\frac{q_{z_2}}{E_{\text{beam}}}\right) f_{\text{flux}}(q_{z_1}, q_{z_2}),$$

(8.5)

where p_1, p_2, p_3 are the four-momenta of the final state partons which lead to creation of extra jets, L is the four-momenta of the final state lepton, ν the four-momentum of the final state neutrino, and q_1, q_2 are the four-momenta of incoming partons. We assume further that the misidentified lepton carries the momentum of the parton.

An evaluation of the matrix element for $Wjjj$ using parton-level events is shown in Figure 8.5 (*left*); the matrix element is able to separate $t\bar{t}$ events from $Wjjj$ events quite well. In Figure 8.5 (*right*), we have discarded the neutrino information, Gaussian smeared

70

the parton-level quantities and performed the four-dimensional integration using Gaussian transfer functions.

Finally, we evaluate the full fake probability, applying the integration and transfer functions as above. We employ a sample of events from the data which are candidates to produce a fake lepton. Figure 8.6 shows the resulting distributions.

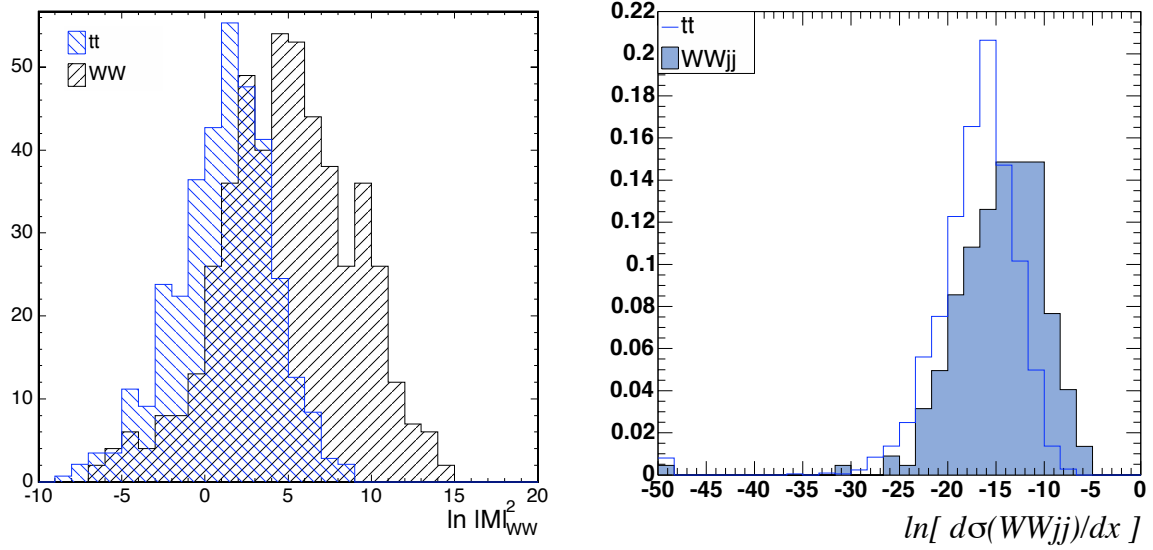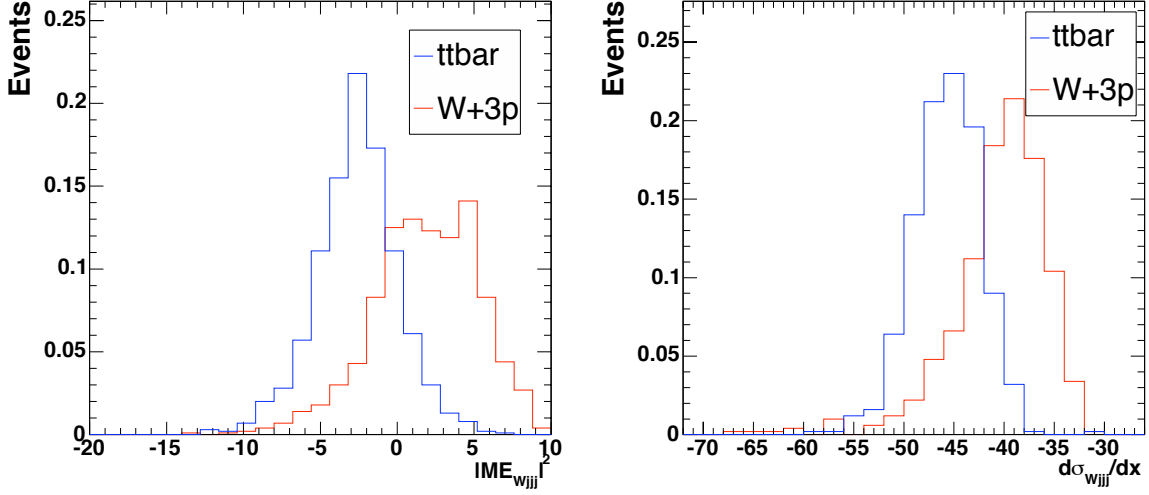Figure 8.5: *Left*: Evaluation of the squared matrix element for $p\bar{p} \rightarrow W(\rightarrow l\nu) + 3$ jets for parton-level $t\bar{t}$ and $W + 3p$ events. *Right*: Evaluation of the $Wjjj$ probability for Gaussian smeared $Wjjj$ and $t\bar{t}$ events.
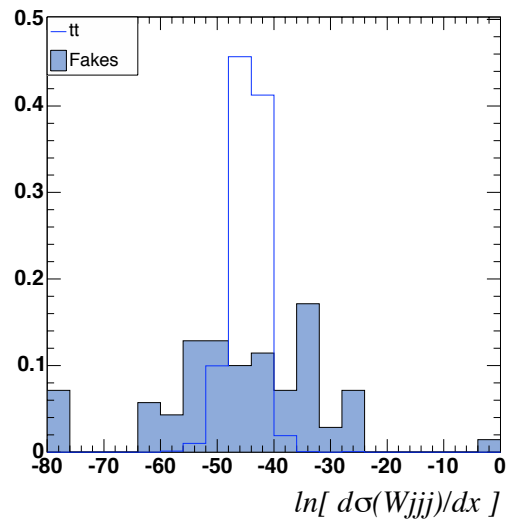
Figure 8.6: Evaluation of the $Wjjj$ probability for fully simulated $t\bar{t}$ and events from the data which are candidates to produce a fake lepton.

CHAPTER 9

Mass Extraction and Calibration

In this chapter, we discuss the combination of the per-event differential cross section calculations for signal and background into a joint probability for a sample of events, the procedure for mass extraction, and calibration of the method using simulated events.

9.1 Mass Extraction

9.1.1 Posterior Probability

We express the individual event probability density in $\mathbf{x}$ as a sum of the signal and background probabilities with their respective fractions as in Equation 5.5. The signal and background fractions are expressed in terms of the number of expected signal events $\lambda_s(M_t)$ and background λ_b events:

$$
\begin{aligned}
p_s(M_t) &= \frac{\lambda_s(M_t)}{\lambda_s(M_t) + \lambda_b} \\
p_{b_i}(M_t) &= \frac{\lambda_{b_i}}{\lambda_s(M_t) + \lambda_b},
\end{aligned} \tag{9.1}
$$

where $\lambda_b = \sum_i \lambda_{b_i}$. The values used for $\lambda_s(175)$ and the λ_{b_i} are given in Table 4.1. The expected signal $\lambda_s(M_t)$ is calculated relative to a reference point M_0 and extrapolated to

other masses using the mass dependence of the total accepted cross section $\sigma_s(M_t)\epsilon_s(M_t)$:

$$\lambda_s(M_t) = \lambda_s(m_0)\frac{\sigma_s(M_t)\epsilon_s(M_t)}{\sigma_s(M_0)\epsilon_s(M_0)},\tag{9.2}$$

where $\sigma_s(M_t)$ is the total production cross section [15] and $\epsilon_s(M_t)$ is the acceptance measured in Monte Carlo events (see Figure 4.3).

For an individual event $\mathbf{x}$, $P(\mathbf{x}|M_t)$ is a likelihood in M_t. The posterior probability density in M_t is the product of a flat prior probability and the product of the individual event likelihoods. The measured mass, $\hat{M}_t$, is chosen as the expectation value of the posterior probability to avoid potential fluctuations in the position of the maximum probability:

$$\hat{M}_t = \frac{\int dM_t M_t P(\mathbf{x}|M_t)}{\int dM_t P(\mathbf{x}|M_t)}\tag{9.3}$$

The measured statistical uncertainty, $\Delta\hat{M}_t$, is the standard deviation of the posterior probability,

$$\Delta\hat{M}_t = \sqrt{\frac{\int dM_t M_t^2 P(\mathbf{x}|M_t)}{\int dM_t P(\mathbf{x}|M_t)} - (\hat{M}_t)^2}\tag{9.4}$$

Due to effects including the violation of assumptions listed in Chapter 5 in realistic events, imperfections in the models used for background probabilities, and the presence of backgrounds that are not modeled with a background probability, $\hat{M}_t$ and $\Delta\hat{M}_t$ deviate from what we expect the true mass and error to be. The following section describes the procedure used to extract a calibration to correct for these effects.

9.2   Calibration

We have searched for any potential biases on the extracted mass or its uncertainty due to our fitting procedure. We parameterize this bias using a linear correction factor to the

measured mass consisting of an offset M_0 and a slope s_{M_t},

$$M_t = 178.0\,\mathrm{GeV}/c^2 + (\hat{M}_t - M_0)/s_{M_t}, \tag{9.5}$$

and a simple scale factor,

$$\Delta M_t = S_\Delta \times \Delta\hat{M}_t/s_{M_t}, \tag{9.6}$$

to the measured statistical error in data, where M_0, s_{M_t}, S_Δ are extracted from ensembles of Monte Carlo experiments. In the following sections, we study the calibration of the method in Monte Carlo experiments with only $t\bar{t}$ events as well as in Monte Carlo experiments with both $t\bar{t}$ and background events.

9.2.1 Signal only tests with P_s

We first measure the response of the method using purely signal events. The number of events in each Monte Carlo experiment is a random number, Poisson distributed with expected number of events shown in Table 4.1. The probability expression in this case includes only the term that describes leading order $t\bar{t}$ production. Figure 9.1 shows that the response is linear, with a slope very close to 1.0. The statistical uncertainty is underestimated due to approximations (listed in Chapter 5) made in the calculation of the likelihood as discussed in detail in Chapter 7. Figure 9.2 shows the residual and pull parameters.

9.2.2 Signal and Background tests with P_s

We then measure the response of the method using signal and background events. The number of signal and background events in each Monte Carlo experiment is Poisson distributed around the expected number shown in Table 4.1. The probability expression only includes the term that describes the signal process and thus the sensitivity of the method degrades considerably as seen in Figure 9.3.
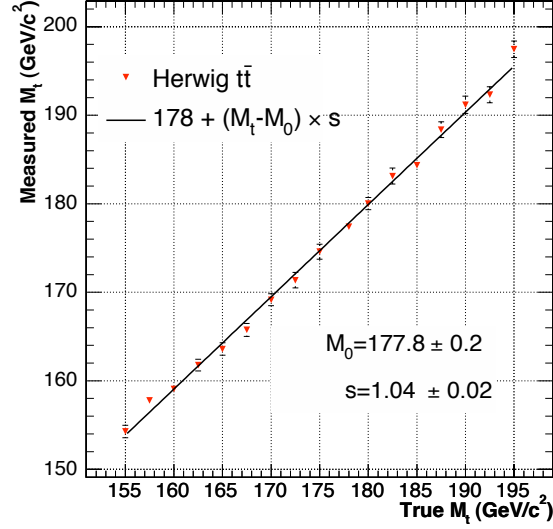
Figure 9.1: Response for Monte Carlo experiments of signal events, using only P_s to extract the mass.

Figure 9.2: Residual in top mass, and mean of pull distribution for varying simulated M_t, in signal-only Monte Carlo experiments.

9.2.3 Signal and Background tests with P_s and P_b

To extract a calibration which will be applicable to the data, we construct Monte Carlo experiments with signal and background events as before. We also add to our likelihood machinery the description of the background processes in the form of P_b, which recovers a significant amount of sensitivity.

We model the largest backgrounds: Z-boson production with two additional jets, W-boson pair production and W boson with three jets with one of the jets being mis-identified
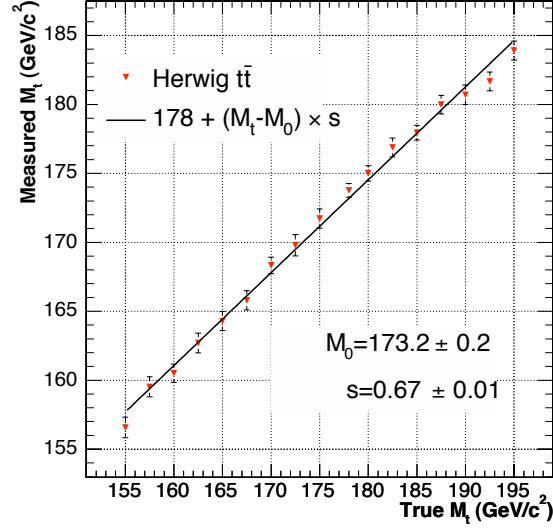
Figure 9.3: Response for Monte Carlo experiments of signal and background events, using only P_s to extract the mass.

as a lepton. While the inclusion of the background probabilities improves the description of the events in the Monte Carlo experiments, it does not return it to the level of the signal-only case, for two reasons. First, the background probabilities are an imperfect description of the background events, due the the same assumptions made during the formulation of the signal probability; second, the generated Monte Carlo experiments contain backgrounds that are not explicitly modeled by any probability term.

Figure 9.4 shows the response with the full probability expression.

Derivation of Response correction

The necessary bias correction is based on the numbers presented in Figure 9.4. We transform the raw mass into the corrected mass using a linear correction in the form of Equation 9.5 where $M_0 = 176.4 \pm 0.2 \text{ GeV}/c^2$ and $s_{M_t} = 0.83 \pm 0.01$. The statistical error in this transformation is propagated to a systematic error in the final analysis. Figure 9.5 shows residuals and pull parameters of the slope-corrected and error-corrected top quark mass.
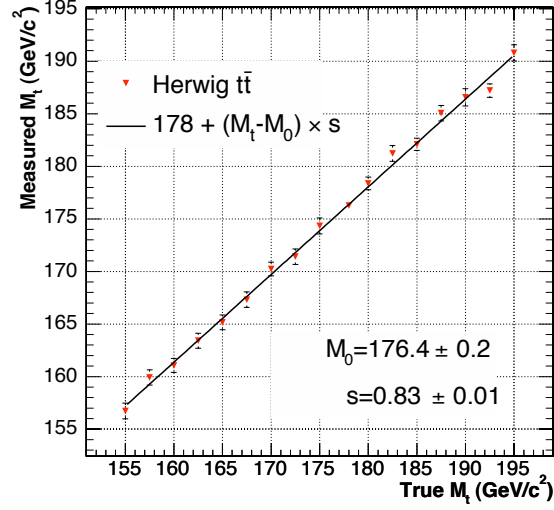
Figure 9.4: Response for Monte Carlo experiments of signal and background events, using only P_s to extract the mass.

Derivation of Error correction

We derive a correction factor for the expected error in the mass by measuring the average underestimation of the statistical error (see Figure 9.5). We measure

$$S_\Delta = 1.17 \pm 0.02$$

and apply this to all samples independent of M_t. The final corrected and scaled performance as a function of M_t can be seen in Figure 9.6 and specifically for $M_t = 175 \text{ GeV}/c^2$ in Figure 9.7 and for $M_t = 165 \text{ GeV}/c^2$ in Figure 9.8.
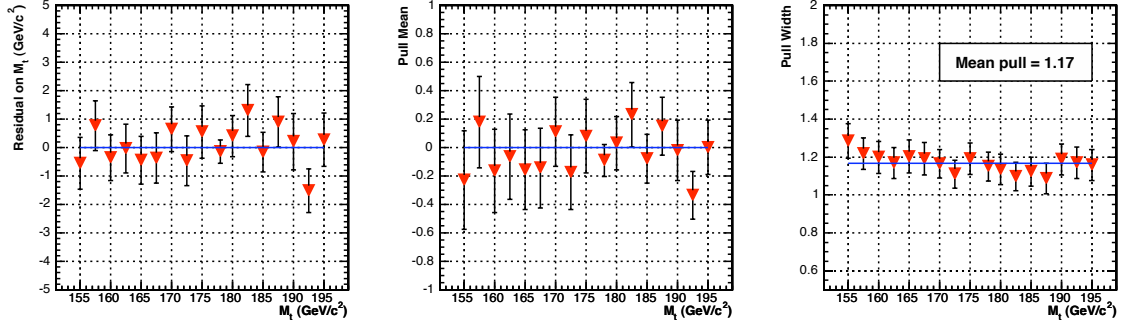
Figure 9.5: Residual in top mass, and mean of pull distribution for varying simulated M_t, in Monte Carlo experiments including both signal and background events. The probability expression includes both P_s and P_b.
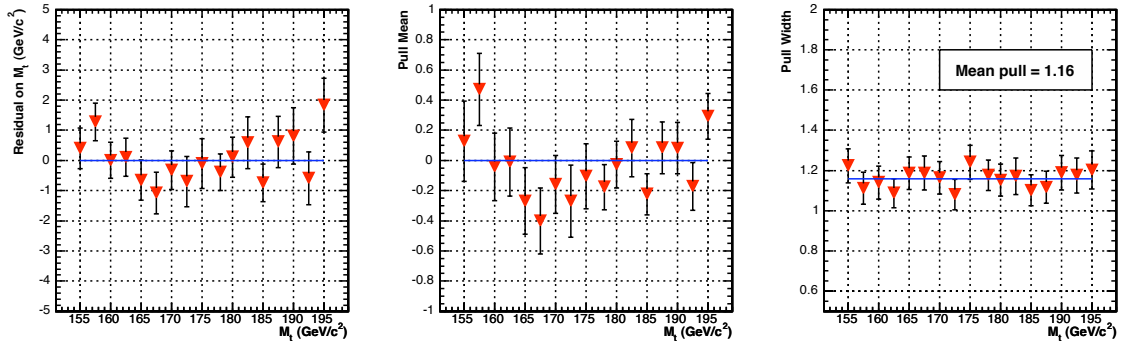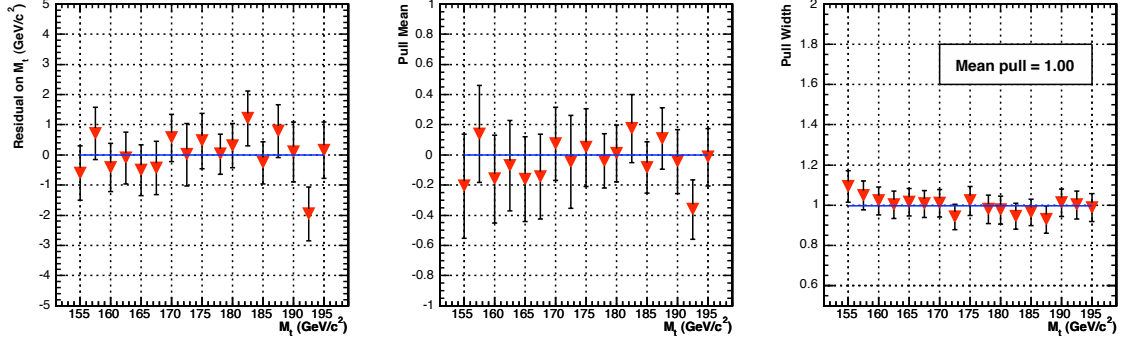

Figure 9.6: Residual in top mass, and mean of pull distribution for varying simulated M_t, Monte Carlo experiments after error scaling.
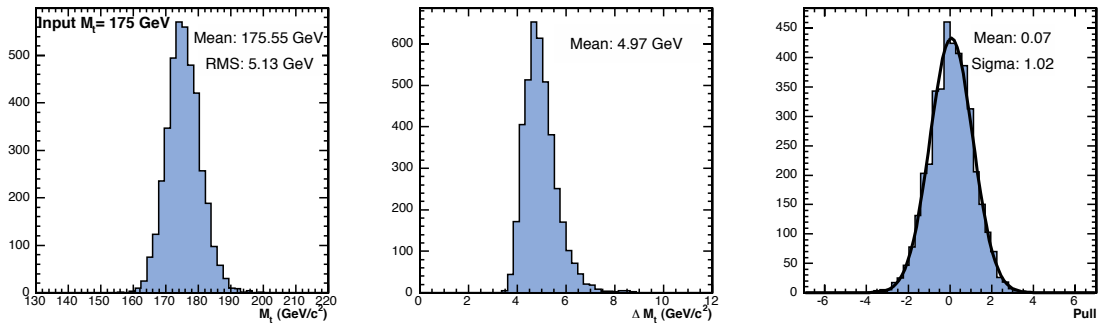
Figure 9.7: Distribution of measured mass, measured statistical error, and pulls for pseudo-experiments using signal events of $M_t = 175$ GeV/c^2 and expected numbers of background events.

79
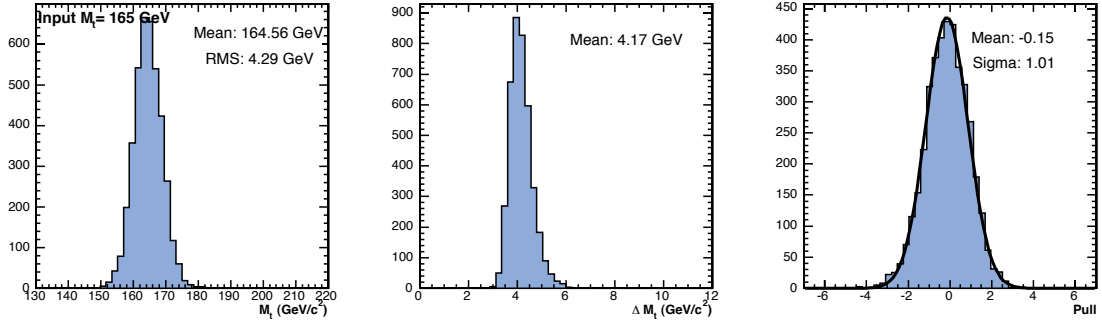
Figure 9.8: Distribution of measured mass, measured statistical error, and pulls for pseudo-experiments using signal events of $M_t = 165$ GeV/c^2 and expected numbers of background events.

CHAPTER 10

Systematic Uncertainties

Our measurement is calibrated using Monte Carlo simulated events. The majority of systematic uncertainties therefore come from our uncertainty in the accuracy of the simulation in modeling the data. In this chapter, we describe the facets of the simulation which may not accurately describe the observed data, and estimate the sensitivity of our measurement to these effects.

To measure the size of the impact of these uncertainties, our strategy is to perform pseudo-experiments using a pool of events in which some feature of the events has been modified. By extracting the average measured mass, we can determine the typical shift due to these shifted features. In some cases, the magnitude of the shift is smaller than its statistical error; for these effects we take as a systematic uncertainty, the magnitude of the statistical error.

10.1 Jet Energy Scale

The measured energy of jets is calibrated using simulated and data events as described in Chapter 4. Due to lack of knowledge of the underlying processes in hadronization and limited data statistics, there is an uncertainty in the correction of the raw jet energy.

We vary the response of the jets in simulated events by one unit of the uncertainty in

the response, and measure the difference in our extracted top mass.

Sample	Measured M_t for $M_t^{true} = 178.0$ GeV/c^2
JES $+1\sigma$	181.87 ± 0.73 GeV/c^2
JES -1σ	174.86 ± 0.71 GeV/c^2

We take half of the difference between the two measurements, $\Delta_{\text{JES}} = 3.51$ GeV/c^2. This is the single largest source of systematic uncertainty in this analysis.

The jet energy scale and its systematic errors are derived primarily for events with light quark and gluon jets. Studies [52] have demonstrated that in lepton+jets events, the b-jet energy scale may have up to a 0.6% additional uncertainty. For comparison, we have measured that moving the b-jet energy scale up by 1% changes the extracted mass by 1.02 GeV/c^2. Thus, we assign an additional uncertainty of 0.61 GeV/c^2.

10.2 Generator

We measure the difference in our extracted mass when using events generated with PYTHIA and with HERWIG.

Sample	Measured M_t for $M_t^{true} = 178.0$ GeV/c^2
Herwig	177.84 ± 0.49 GeV/c^2
Pythia	178.72 ± 0.47 GeV/c^2

We take the difference between the two measurements, $\Delta_{Gen} = 0.88 \pm 0.68$ GeV/c^2.

10.3 Response calibration

The final result depends on the correction derived from our response curve. Uncertainty in this response translates directly into uncertainty in our result. We vary the response by 1σ within the statistical uncertainties of the fit, and measure the difference in our extracted mass.

	Variation of [offset,slope] (GeV/c^2)			
Sample	$[+\sigma, +\sigma]$	$[-\sigma, -\sigma]$	$[+\sigma, -\sigma]$	$[-\sigma, +\sigma]$
$M_t = 170$	170.57	170.71	170.95	170.32
$M_t = 178$	177.67	178.05	178.05	177.66
$M_t = 185$	184.54	184.15	184.92	184.76

In order to be conservative, we take half of the difference between the pair with the largest variation, $\Delta_{Resp} = 0.63$ GeV/c^2.

10.4   Sample composition

We require a knowledge of the expected signal and background composition of the sample in order to construct pseudo-experiments from which we extract our response curve. Given our response curve, we vary the background composition within the quoted uncertainties and measure the difference in the mean extracted mass of an ensemble of pseudo-experiments. Note that the uncertainty in the number of expected $t\bar{t}$ events includes, and is dominated by, the theoretical uncertainty of 10%.

Varied Sample	$+\sigma$ (GeV/c^2)	$-\sigma$ (GeV/c^2)	$\Delta_{M_t}/2$ (GeV/c^2)
$t\bar{t}$	177.43	176.08	0.68
Fakes	177.79	177.86	0.04
Z	178.62	177.86	0.38
WW	177.63	177.86	0.12
WZ	177.96	177.86	0.11
$Z \rightarrow \tau\tau$	177.90	177.54	0.38

We take these results to indicate that we are not strongly sensitive to the background composition and thus assign the uncertainty associated with $t\bar{t}$ as a systematic uncertainty of $\Delta_{Sample} = 0.68$ GeV/c^2.
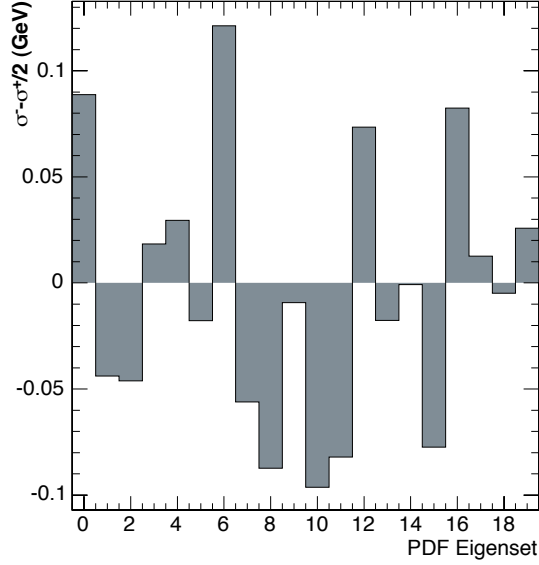
Figure 10.1: Difference in extracted mass between the positive and negative PDF eigenvectors for a Pythia sample.

10.5 PDF uncertainties and α_s

To estimate the uncertainty due to the uncertainties in the PDFs, we reweight the Pythia sample according to 20 sets of positive and negative eigenvectors. We modify our prescription for forming pseudo-experiments to allow for event weights, in which events with higher weight are more likely to be chosen for a given pseudo-experiment. Figure 10.1 shows the $\frac{1}{2}$ difference between the positive and negative eigenvectors. The total uncertainty added in quadrature is $\Delta_{PDF} = 0.27$ GeV/c^2.

In addition, we compare samples with different PDFs, CTEQ5L [43] and MRST72 and confirm that their central values agree well.

Sample	M_t (GeV/c^2)
Pythia, CTEQ5L	178.72 ± 0.47
Pythia, MRST72	178.21 ± 0.49
Pythia, MRST75	178.05 ± 0.52

The two samples MRST72 and MRST75 [53] use different values of α_s to calculate the PDFs; the difference in these two provides a measure of our sensitivity to the uncertainty in α_s. We estimate our systematic uncertainties due to variation of α_s to be $\Delta_{\alpha_s} = 0.15 \pm 0.72$ GeV/c^2.

10.6 Radiation

Our model does not contain any description of initial (ISR) or final state radiation (FSR), which may contribute significantly to the fraction of mismeasured events. The rate of initial state radiation can be well studied in Z+jet events, as there is no final state radiation; the radiation is found to depend smoothly on the energy transfer [52], and can be examined over a broad range of energies, extending up to the range of $t\bar{t}$ production. To measure the uncertainty due to imperfect knowledge of the rate of radiation, we examine the measured top mass in samples where the simulation parameters are varied by very conservative amounts. Final state radiation can be probed in the same manner, as it is described by the same showering algorithm.

Sample	M_t (GeV/c^2)
Pythia	178.72 ± 0.47
Pythia, ISR less	177.92 ± 0.48
Pythia, ISR more	178.53 ± 0.48
Pythia, FSR less	178.16 ± 0.49
Pythia, FSR more	178.80 ± 0.50

We therefore estimate the systematic uncertainty due to modeling of radiation to be $\Delta_{ISR} = 0.30 \pm 0.34$ GeV/c^2, and $\Delta_{FSR} = 0.32 \pm 0.34$ GeV/c^2.

10.7   Background statistics

To measure our dependence on the relatively small background samples, we split each background sample into twenty pairs of disjoint sets. We measure the mass in the $M_t = 178$ GeV/c^2 sample for each of the disjoint sets and take the root mean square of the difference between them as an estimate of the uncertainty due to having samples of finite size. The variation in measured mass for each of the background samples is shown in Figure 10.2. This is an estimate of the uncertainty due to having samples twice as small as the samples we use, and so we divide the uncertainty by $\sqrt{2}$.

Background	$RMS(\Delta M_t)/\sqrt{2}$ (GeV/c^2)
Z	0.44
Fakes	0.48
WW	0.13
WZ	0.09
$Z \to \tau\tau$	0.21

We take the sum in quadrature, $\Delta_{BGstat} = 0.70$ GeV/c^2.

10.8   Background Modeling

The modeling of the two largest backgrounds may be imperfect; we estimate our sensitivity to possible imperfections in these background models.

10.8.1   Drell-Yan

Drell-Yan production is difficult to model well, as it has a large cross-section and a small acceptance. Since there is no real missing energy due to escaping neutrinos, there is a small probability to pass the missing energy requirement. One might be concerned whether the modeling of large missing energy on the tails of these distributions is accurate.
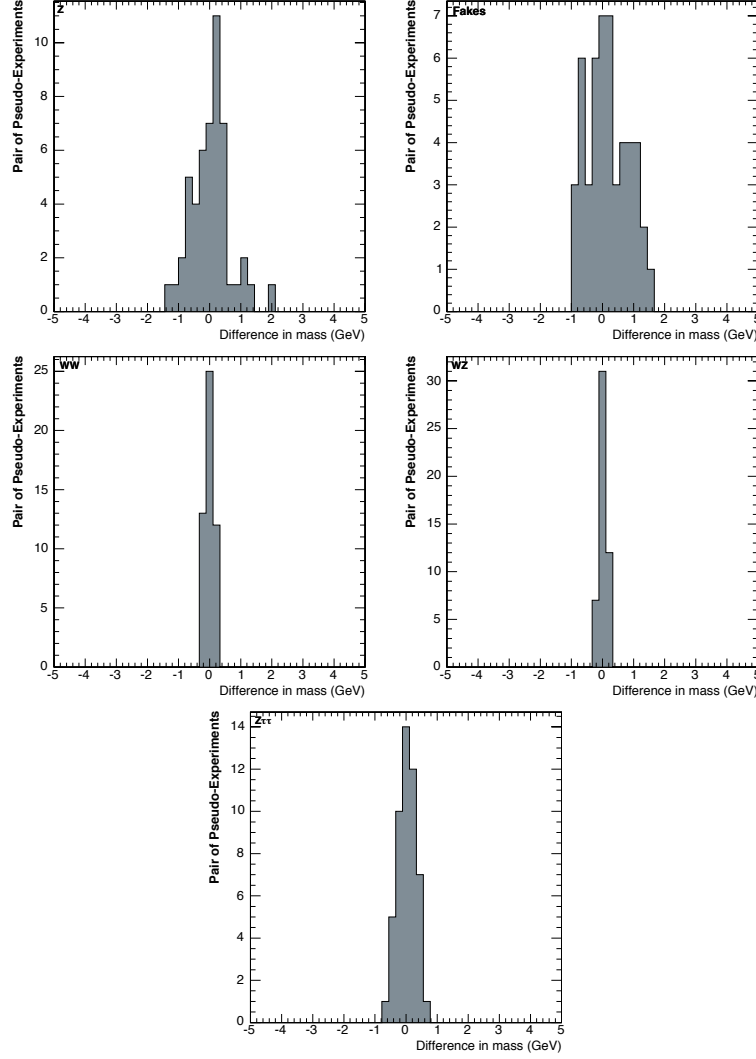
Figure 10.2: Variation in measured mass when background samples are split into disjoint sets. Top left, Z; Top right, Fakes. Middle left, WW; Middle right, WZ. Bottom, $Z \to \tau\tau$.

To gauge our sensitivity to events on the tails of the distribution, we vary the composition of our pseudo-experiments by both enhancing events and suppressing on events on the tails. We assign a weight to each event as

$$w_+ = 1 + \frac{1}{\sqrt{n_+}}$$

$$w_0 = 1$$

87

$$w_- = 1 - \frac{1}{\sqrt{n_+}}$$

where n_+ represents the number of events further out on the tail of the missing energy distribution than the given event. The event with the largest missing energy will receive weights $(w_+ = 2, w_0 = 1, w_- = 0)$. This enhances or suppresses the tail events.

Weights	M_t (GeV/c^2)
w_+	177.73 ± 0.50
w_0	177.79 ± 0.49
w_-	177.57 ± 0.50

As demonstrated by the calibration of the response, the mass measurement suppresses a good portion of contribution of Zjj events to the extracted mass; this makes the result less sensitive to variations in the background shape.

We take as the uncertainty due to the shape of this background $\Delta_{Shape}^{Drell-Yan} = 0.22$ GeV/c^2.

10.8.2 Fake background

The fake background is very difficult to model well in the simulation, as it is sensitive to the smallest details of the detector performance. To avoid issues of modeling, the events which imitate this background are drawn from the data itself; the events are selected with a looser requirement on one of the leptons in order to accumulate a sample of fake candidates, and then weighted by the probability that the loose lepton would pass lepton identification requirements. These weights are calculated as a function of the P_T and isolation of the fake candidate, and each candidate has its own weight (w) and uncertainty (Δw).

To gauge our sensitivity to the calculation of the fake rates, we vary the fake rates in two ways. First (a), we enhance those events with large fake probability, to exaggerate

their effect; second (b), we enhance events with small fake probability, to exaggerate their effect:

Mode	$w > \overline{w}$	$w < \overline{w}$
a	$w \to w + \Delta w$	$w \to w - \Delta w$
b	$w \to w - \Delta w$	$w \to w + \Delta w$

We study the effect of this weighting on fully realistic pseudo-experiments:

Weights	M_t (GeV/c^2)
w_a	177.83 ± 0.49
default	177.84 ± 0.49
w_b	177.76 ± 0.49

As argued above, the mass measurement is reasonably successful at reducing the effect of these background events, which makes the extracted mass less sensitive to their shapes.

We take the difference as our systematic uncertainty, $\Delta_{Shape}^{fakes} = 0.08$ GeV/c^2, and the total shape uncertainty to be the two in quadrature

$$\Delta_{Shape} = 0.23 \text{ GeV}/c^2.$$

10.9   Lepton Energy Scale

Studies have shown that the Monte Carlo has an energy scale for electrons that is up to 0.5% higher than that in data. As the Monte Carlo events we use do not include a scale factor to account for this effect, we measure an associated systematic uncertainty by varying the lepton energy scale in Monte Carlo events by $\pm 1\%$.

Sample	Measured M_t for $M_t^{true} = 178.0$ GeV/c^2
LES $+1\%$	177.54 ± 0.49 GeV/c^2
LES -1%	177.29 ± 0.48 GeV/c^2

Source	Size
Jet Energy Scale	3.5 GeV/c^2
B-jet energy scale	0.6 GeV/c^2
Generator	0.9 GeV/c^2
Response uncertainty	0.6 GeV/c^2
Sample composition uncertainty	0.7 GeV/c^2
Background statistics	0.7 GeV/c^2
Background modeling	0.2 GeV/c^2
ISR modeling	0.3 GeV/c^2
FSR modeling	0.3 GeV/c^2
PDFs	0.3 GeV/c^2
α_s	0.2 ± 0.7 GeV/c^2
Lepton Energy Scale	0.1 GeV/c^2
Total	3.9 GeV/c^2

Table 10.1: Summary of systematic uncertainties

We take half of the difference between the two measurements, $\Delta_{\text{LES}} = 0.13$ GeV/c^2.

10.10   Summary

The systematic uncertainties measured in the previous sections are summarized in Table 10.1. Our total systematic uncertainty is 3.9 GeV/c^2.

CHAPTER 11

Measurement in Data

The measurement in data is performed with a sample of $\int L dt = 1.0$ fb^{-1}. This sample contains 78 candidate events passing the selection cuts outlined in Chapter 4. Their run, event numbers and a summary of their kinematic properties can be found in Appendix A, Tables A.1- A.3.

11.1   Kinematic Properties of Observed Events

We examine the events observed in the data and compare their kinematic properties to those predicted from the simulation; the latter is the sum of signal and background contributions.

Examining the kinematic distributions in Appendix A (see Figures A.1-A.14) does not reveal any dramatic deviation in shape for any variable.

In addition, we compare the expected probability distributions of $t\bar{t}$, Zjj, Fake and $WWjj$ probabilities to the observed events, see Figures 11.1-11.4. These quantities are sensitive to all of the kinematic information in the event, and show no significant shape discrepancies.

Figure 11.1: Comparison of the $t\bar{t}$ probability distribution for simulated events, scaled by expected contribution to the sample composition, to that for observed events.

Figure 11.2: Comparison of the Zjj probability distribution for simulated events, scaled by expected contribution to the sample composition, to that for observed events.

92

Figure 11.3: Comparison of the $WWjj$ probability distribution for simulated events, scaled by expected contribution to the sample composition, to that for observed events.
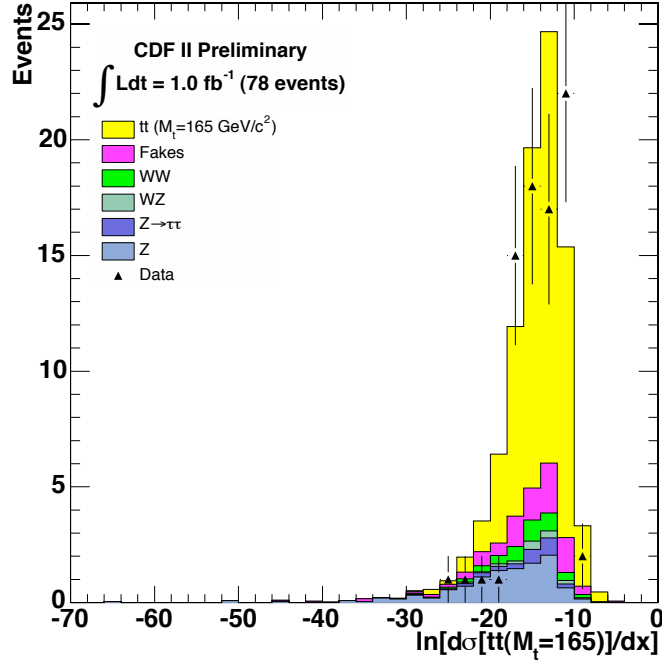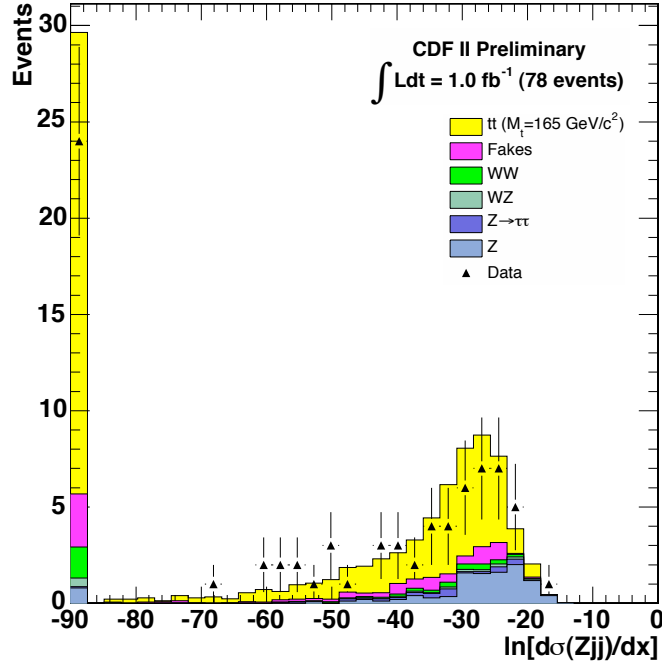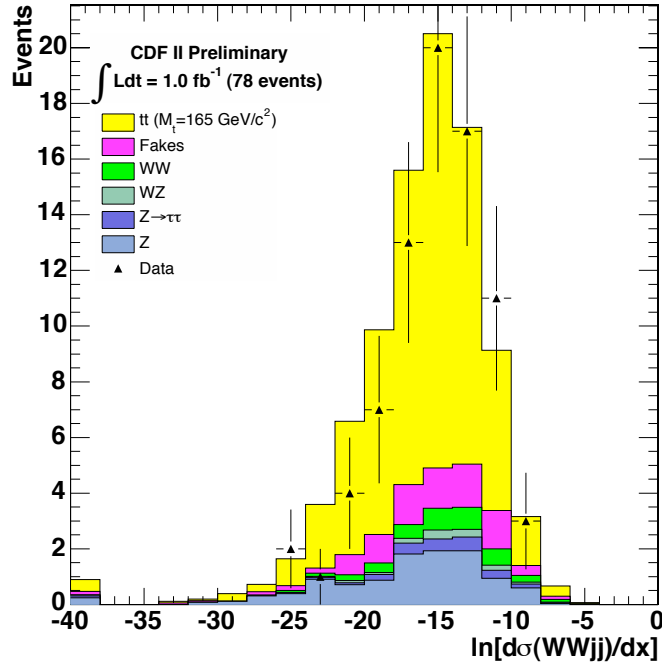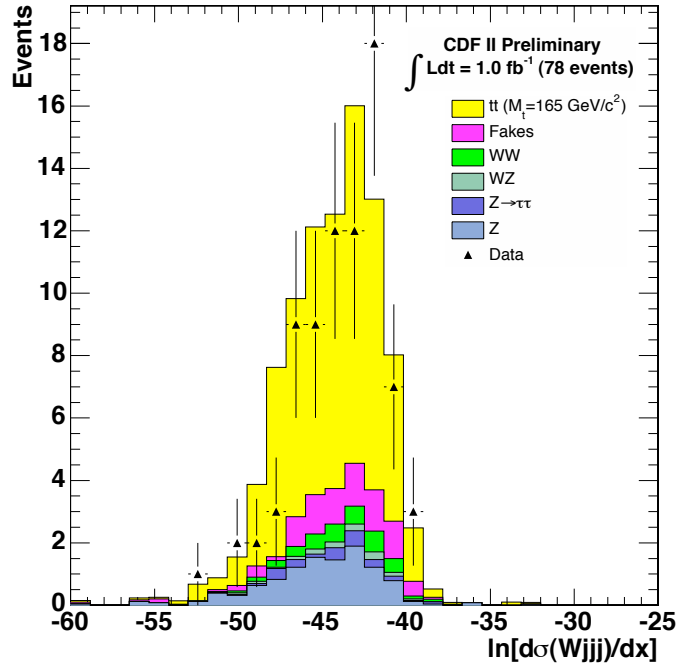

Figure 11.4: Comparison of the Fake probability distribution for simulated events, scaled by expected contribution to the sample composition, to that for observed events.

11.2 Result

The 78 candidate events in the data have individual posterior probabilities as seen in Figures 11.5-11.7. From the joint probability, we extract the uncorrected, unscaled mass,

$$M_t^{raw} = 165.11 \pm 2.82^{raw,unscaled} \text{ GeV}/c^2$$

After applying the response correction and the error scaling as described in Chapter 9, the final result is

$$M_t = 164.49 \pm 3.94 \text{ GeV}/c^2$$

The posterior probability curve can be seen in Figure 11.8. The error we measure is not unexpected when one considers the central value; in pseudo-experiments where $M_t = 165$ GeV/c^2, 46% of the errors are smaller than this value, see Figure 11.9.

We can validate the measured mass by measuring M_t separately in events with two electrons, events with two muons and events with both an electron and a muon. These results are shown in Figure 11.10 and are all consistent with one another.
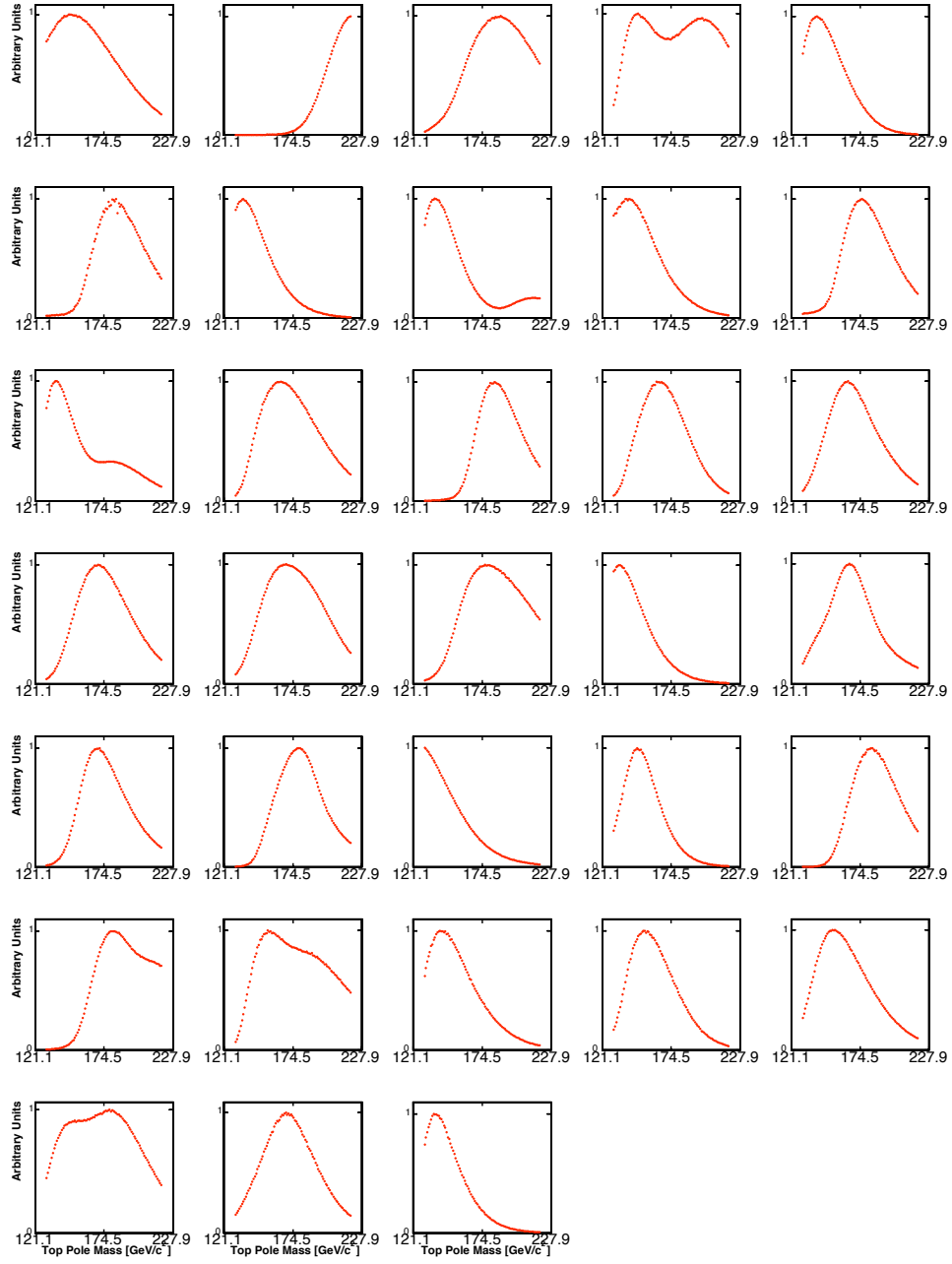
Figure 11.5: Posterior probabilities for each of the 33 candidate events found in 340 pb^{-1} of data collected between March 2002 and August 2004. Each includes the normalized signal and background probabilities.
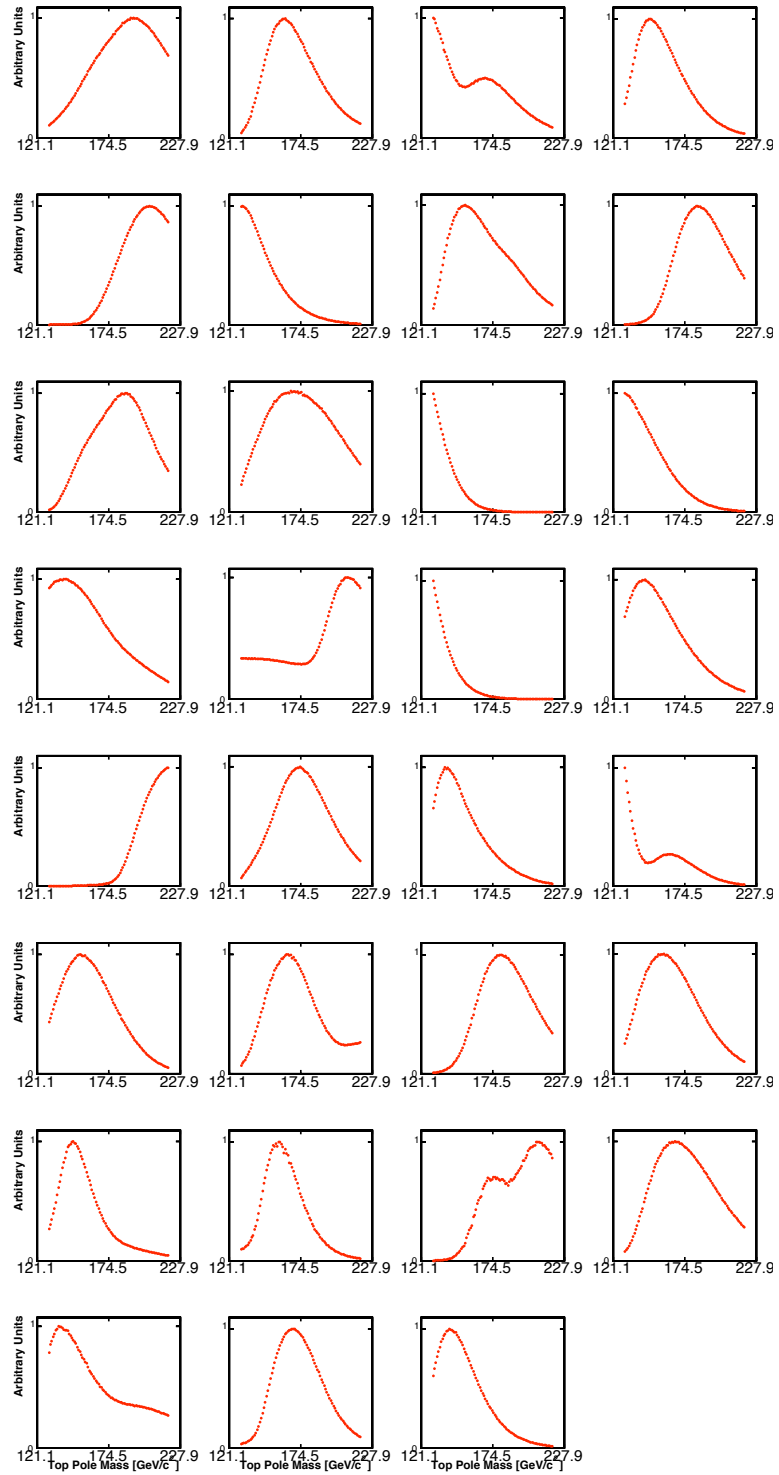
Figure 11.6: Posterior probabilities for each of the 31 candidate events found in the 400 pb^{-1} of data collected between December 2004 and September 2005. Each includes the normalized signal and background probabilities.
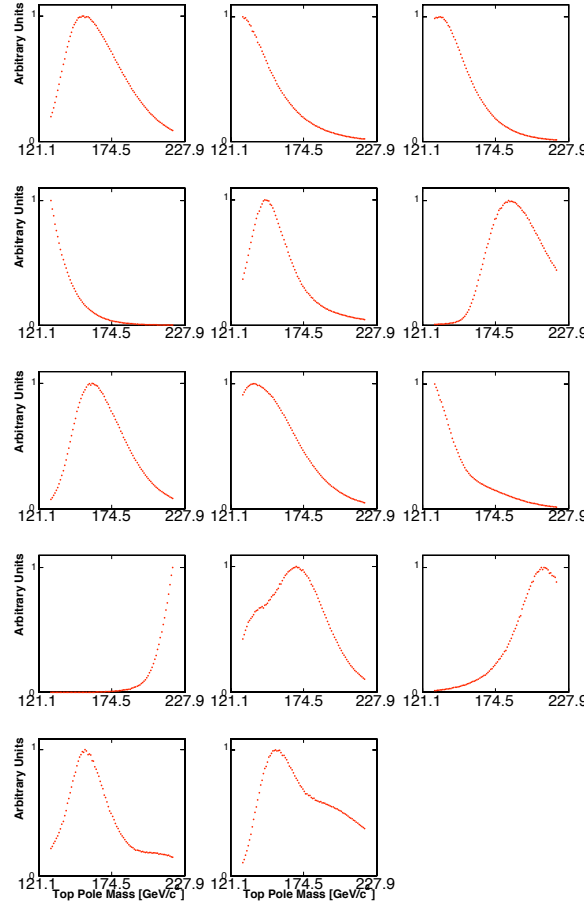
Figure 11.7: Posterior probabilities for each of the 14 candidate events found in the 260 pb^{-1} of data collected between September 2005 and February 2006. Each includes the normalized signal and background probabilities.
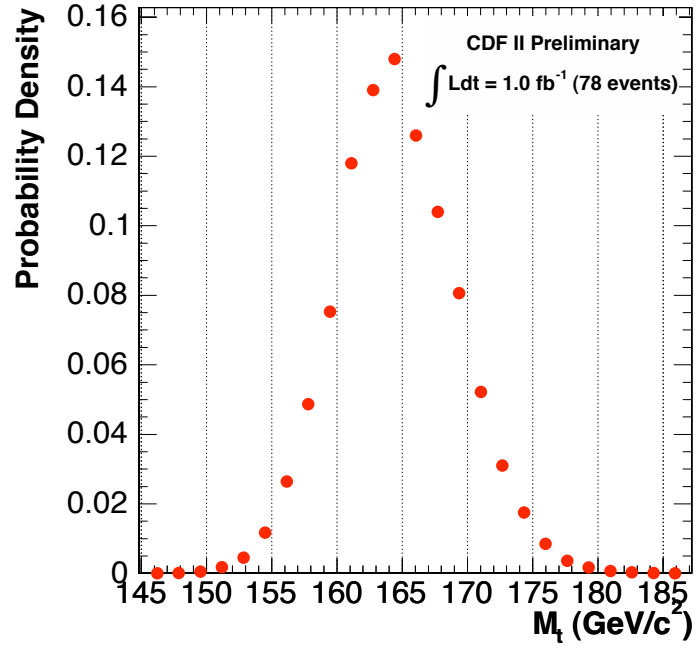
Figure 11.8: Final posterior probability density as a function of the top pole mass for the 78 candidate events in the data.
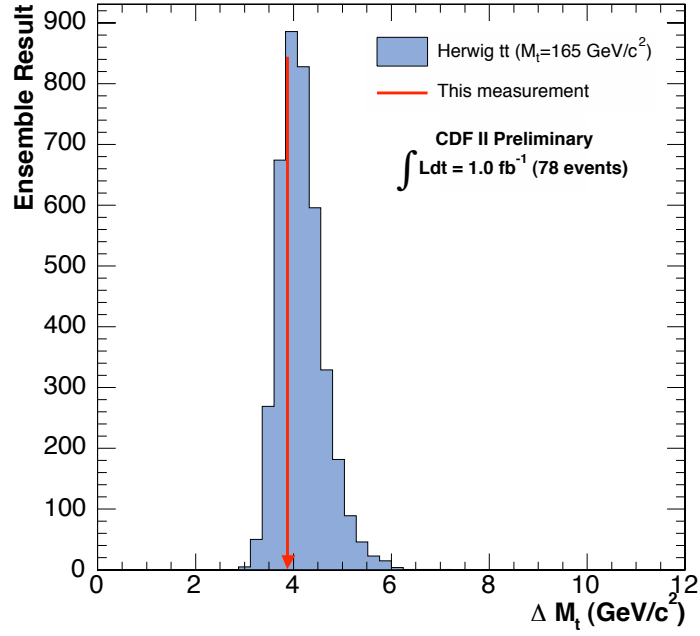
Figure 11.9: Distribution of expected errors for $M_t = 165$ GeV/c^2. The measured error is shows as the line; 46% of pseudo-experiments yield a smaller error.
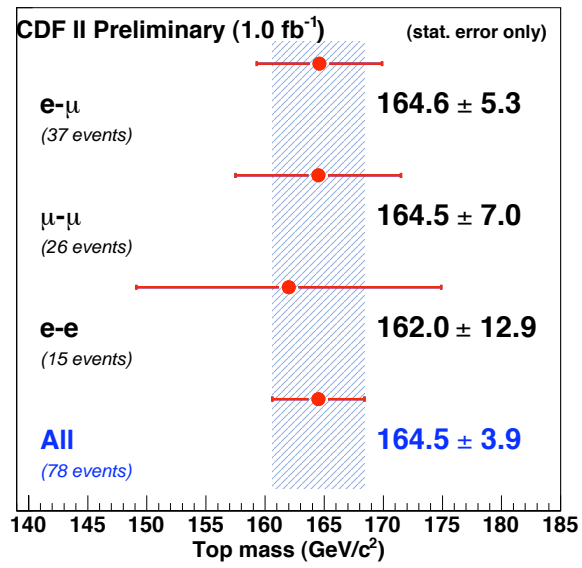
Figure 11.10: Measurement of the top quark mass in ee, $\mu\mu$ and $e\mu$ events separately. The measurement in all data events is also shown for comparison. Only statistical uncertainties are shown.

CHAPTER 12

Conclusion

We have measured the mass of the top quark in the dilepton decay channel. Using 1.0 fb^{-1} of Run II data collected at the CDF detector, we measure:

$$M_t = 164.5 \pm 3.9(\text{stat.}) \pm 3.9(\text{syst.})\text{GeV}/c^2.$$

This result shows little deviation from the previously published result in this channel [2],

$$M_t = 165.2 \pm 6.1(\text{stat.}) \pm 3.4(\text{syst.})\text{GeV}/c^2,$$

which uses 340 pb^{-1} of data. It is also consistent with recently published template-based measurements of the top quark mass in this channel [54],

$$M_t = 170.1 \pm 6.0(\text{stat.}) \pm 4.1(\text{syst.})\text{GeV}/c^2,$$

which uses up to 360 pb^{-1} of data. Our measured value is smaller than recent template-based measurements in the lepton+jets channel [55],

$$M_t = 173.4 \pm 2.5(\text{stat.+JES}) \pm 1.3(\text{syst.})\text{GeV}/c^2,$$

using 680 pb^{-1}. This deviation is not inconsistent with a statistical fluctuation [18]. The possibility of this deviation being a fluctuation is further enforced by the most recent

preliminary measurement of the top quark mass in the lepton+jets channel [56],

$$M_t = 170.9 \pm 2.2(\text{stat.+JES}) \pm 1.4(\text{syst.})\text{GeV}/c^2,$$

which uses 940 pb^{-1} of data and a matrix-element method. More data will be needed to tell whether a significant deviation exists amongst channels.

Additionally, we can apply secondary vertex tagging to identify b-quarks in the dilepton sample used in this analysis. The requirement of a b-tag results in a subset of the dilepton sample with a signal-to-background ratio of 20:1 despite the loss of 40% of the expected signal statistics. The resulting sample can be used to verify our measurement of the top quark mass in the dilepton channel in a near background-free sample. Applying the same mass measurement technique to this b-tagged sample (we use the SECVTX tagging algorithm, described in Ref. [57]), we measure [58]:

$$M_t = 167.3 \pm 4.6(\text{stat}) \pm 3.8(\text{syst.})\text{GeV}/c^2.$$

This result is consistent with the measurement made in the full sample.

The measurement described in this dissertation is included as part of a combination performed using measurements from both CDF and DØ in all decay channels [59]:

$$M_t = 171.4 \pm 1.2(\text{stat.}) \pm 1.8(\text{syst.})\text{GeV}/c^2.$$

In this combination, our measurement contributes a weight of 4.8%. Using this evaluation of the top quark mass and other precision electroweak measurements the constraints on the standard model Higgs Boson are [60]:

$$M_H = 85^{+39}_{-28} \text{ GeV}/c^2$$

$$M_H < 166 \text{ GeV}/c^2 \text{ at } 95\% \text{ CL.}$$

We anticipate that the method used to make this measurement will result in a statistical uncertainty of 2 GeV/c^2 with 4 fb^{-1} of data. Systematic uncertainties will be dominant at this level. Several improvements to the method are in progress, including:

- Using a selection criteria based on genetically evolving neural networks, optimized for measurements of the top quark mass.

- Using events from the decay $Z \to b\bar{b}$ to calibrate the b-jet energy scale, allowing for a reduction in the jet energy scale systematic uncertainty.

In addition, accumulating more data will help reduce the uncertainty associated with background estimates that rely on data events, such as fakes and $Z/\gamma^* \to ee, \mu\mu$. Assuming 8 fb^{-1} of data can be accumulated by the end of Run II, an overall uncertainty of less than 1.5 GeV/c^2 for a combined measurement of the top quark mass is possible.

APPENDIX A

Kinematic Details of Data Events

The run, event numbers and a summary of their kinematic properties can be found in Table A.1-A.3. Distribution of kinematic variables can be found in Figures A.1-A.14.
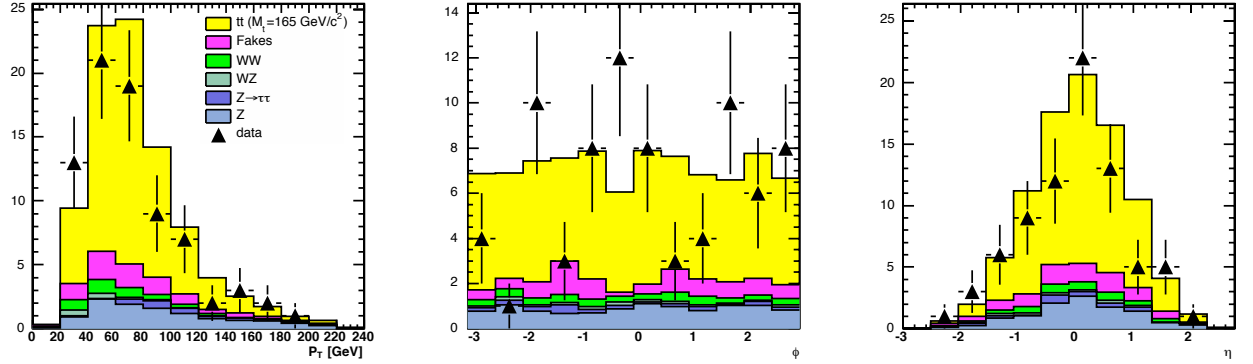

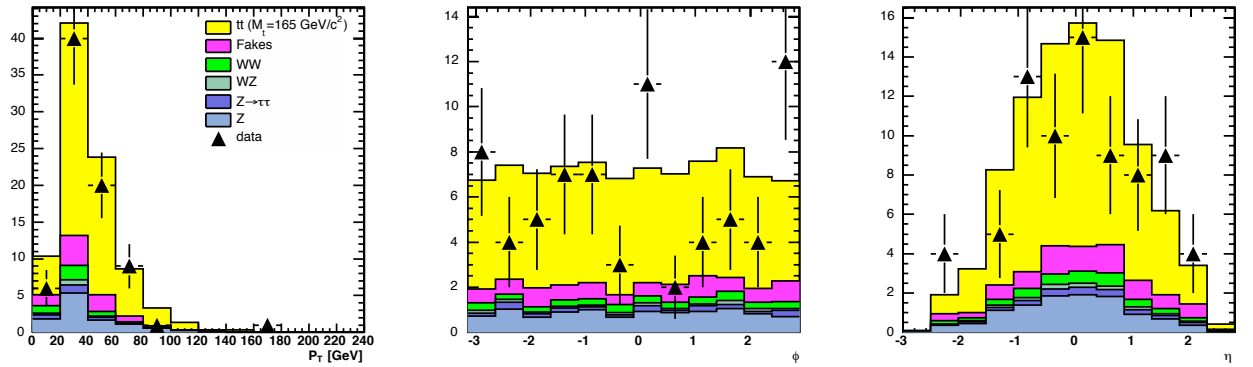Figure A.1: Transverse momentum (P_T), azimuthal angle (ϕ) and pseudo-rapidity (η) of the leading jet.

Figure A.2: Transverse momentum (P_T), azimuthal angle (ϕ) and pseudo-rapidity (η) of the second jet.

| | | P_T [GeV/c] | | E_T [GeV] | | $\not{E}_T$ | |
Run	Event	Lepton 1	Lepton 2	Jet 1	Jet 2	[GeV]	N_{jets}
177491	3807306	25.94	21.03	67.44	42.8	79.22	3
178738	1660363	99.99	60.59	42.67	36.52	90.26	3
143257	760520	27.29	20.96	43.87	36.79	92.24	4
150431	368759	58.27	36.19	54.85	32.56	44.07	4
150435	2896171	45.37	42.88	88.21	44.22	64.71	2
155114	478702	34.48	28.47	73.59	36.02	89.96	3
156484	3099305	35.17	34.31	66.91	34.22	75.91	3
150418	960369	91.38	89.48	30.67	25.99	68.66	2
151978	507773	35.89	34.72	47.04	45.7	91.35	2
153374	2276742	72.02	56.87	85.76	55.15	58.14	3
161633	963604	40.24	26.49	62.27	36.36	60.52	3
165364	592961	47.35	21.59	78.9	47.31	127.9	3
166063	2833132	41.36	38.04	49.73	49.62	64.97	2
167053	12011678	75.77	50.43	86.61	26.31	28.47	3
167631	2058969	33.97	31.34	38.33	36.65	61.32	2
167629	180103	96.57	78.59	77.06	35.49	28.4	2
168599	2964061	40.76	23.68	35.7	33.45	96.85	3
183963	1259645	84.72	27.04	142.1	28.9	63.14	2
184779	892809	51.1	46.9	46.05	20.01	48.86	2
184289	101220	147.8	49.19	135.1	38.71	29.67	2
186598	1618142	69.41	35.75	70.19	68.91	66.96	3
186598	4194951	54.5	36.05	90.35	58.62	42.65	2
178540	2208375	64.42	34.77	96.19	42.62	53.59	2
178738	10340757	50.05	21.39	75.71	36.06	88.4	2
153325	599511	37.11	25.23	50.78	34.32	46.47	3
153447	2643751	87.45	26.3	106.4	20.98	35.52	3
154654	7344016	59.42	52.86	36.43	19.96	56.66	3
160988	385505	26.05	21.02	87.15	56.91	32.19	2
162820	7050764	33.46	26.24	65.95	52.41	95.84	2
163012	1438203	119.1	98.54	103.8	73.67	80.55	2
165198	1827962	34.48	23.82	63.08	31.83	101.4	2
185037	2287335	85.73	56.09	65.78	60.03	26.92	2
185377	103906	76	20.87	69.53	26.34	80.59	2

Table A.1: Run and event numbers and some kinematic quantities for the 33 candidate events found in 340 pb^{-1} of data collected between March 2002 and August 2004.

		P_T [GeV/c]		E_T [GeV]		$\not{E}_T$	
Run	Event	Lepton 1	Lepton 2	Jet 1	Jet 2	[GeV]	N_{jets}
193031	7271850	94.82	42.06	76.9	64.41	103	2
193032	1657759	69.74	43.75	40.1	16.31	70.32	2
193051	1108405	114.1	60.28	40.05	39.72	55.01	2
193892	345334	75.91	50.23	142.3	31.74	116.5	3
194590	4487208	65.96	34.23	51.62	44.88	90.77	3
196902	291907	25.06	23.86	56.24	27.19	69.67	3
196170	1783955	44.93	33.17	109.9	39.17	55.08	2
196473	3624629	36.67	26.96	53.77	34.69	51.88	3
196902	1636420	34.79	24.94	166.5	64.69	50.15	4
195742	628424	67.02	23.05	54.43	49.66	67.58	4
198082	4507326	30.64	22.66	105.2	64.17	25.77	3
197404	240811	87.96	51.25	33.14	18.31	78.74	3
198695	5284824	109	81.18	74.63	41.11	40.93	2
198710	4284073	39.7	25.56	52.52	44.92	57.89	4
202135	5684094	34.61	32.99	26.7	23.7	57.16	4
202514	4625226	52.84	34.79	37.7	36.95	79.06	2
203265	2621856	32.84	21.37	96.81	55.72	87.55	3
193901	1732074	146.9	76.4	32.5	32.07	31.12	2
193901	1851653	76.88	27.09	117.9	15.83	91.4	2
191545	898092	58.75	33.64	79.17	64.26	45.53	5
192348	8119187	120.4	37.35	156.5	21.3	109.9	2
193991	1042119	45.31	34.51	74.95	60.55	80.07	2
195341	4235173	43.63	26.5	46.68	40.44	109.2	2
198340	192801	47.55	28.39	90.26	52.81	56.23	2
197808	6530989	57.85	33.78	39.85	20.67	63.05	2
196663	714179	61.08	36.59	30.35	24.74	56.98	3
202771	5737518	48.85	24.36	72.86	26.07	62.12	3
202397	204913	53.87	33.56	58.92	37.08	25.55	3
203764	2353176	39.65	31.2	165	96.52	93.98	3
199650	2833299	79.63	38.44	127.1	61.65	52.95	2
199655	1714860	35.16	22.61	64.12	50.29	71.22	2

Table A.2: Run and event numbers and some kinematic quantities for events found in the 400 pb^{-1} of data collected between December 2004 and September 2005.

Run	Event	P_T [GeV/c] Lepton 1	Lepton 2	E_T [GeV] Jet 1	Jet 2	$\not{E}_T$ [GeV]	N_{jets}
206723	7731509	31.28	25.01	100.8	17.38	74.9	2
206836	1380873	38.9	23.63	58.04	40.29	71.4	3
204111	59242	56.46	49.33	39.74	21.91	33.64	2
205009	1907663	41.66	25.84	25.29	22.2	25.73	6
204640	4116811	56.62	41.22	102	31.76	63.77	2
205324	1393300	65.22	25.47	88.32	42.01	127.4	2
209191	2272489	121.4	81.12	24.8	17.12	44.36	2
210008	7652752	50.66	46.37	55.64	34.38	64.92	3
207156	2387787	41.77	26.14	47.88	31.3	95.6	2
209263	3986598	32.78	25.1	188.3	177.8	47.96	4
203819	7922132	63.86	36.84	69.81	36.56	41.47	2
205628	2185064	162	97.41	52.12	35.29	66.84	3
203824	196206	139.1	20.85	58.01	22.96	58.05	2
207079	11915785	37.84	33.52	99.8	30.88	108.1	3

Table A.3: Run and event numbers and some kinematic quantities for cthe 14 candidate events found in the 260 pb^{-1} of data collected between September 2005 and February 2006.
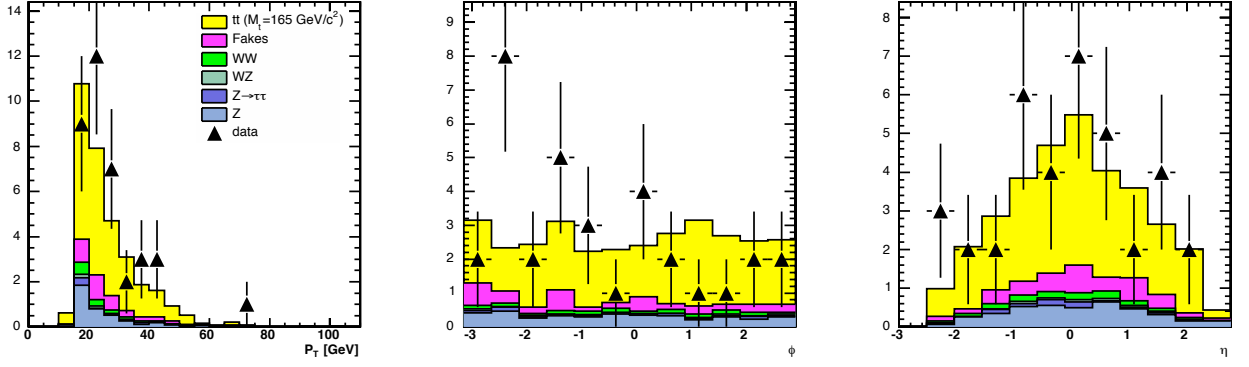

Figure A.3: Transverse momentum (P_T), azimuthal angle (ϕ) and pseudo-rapidity (η) of the third jet.
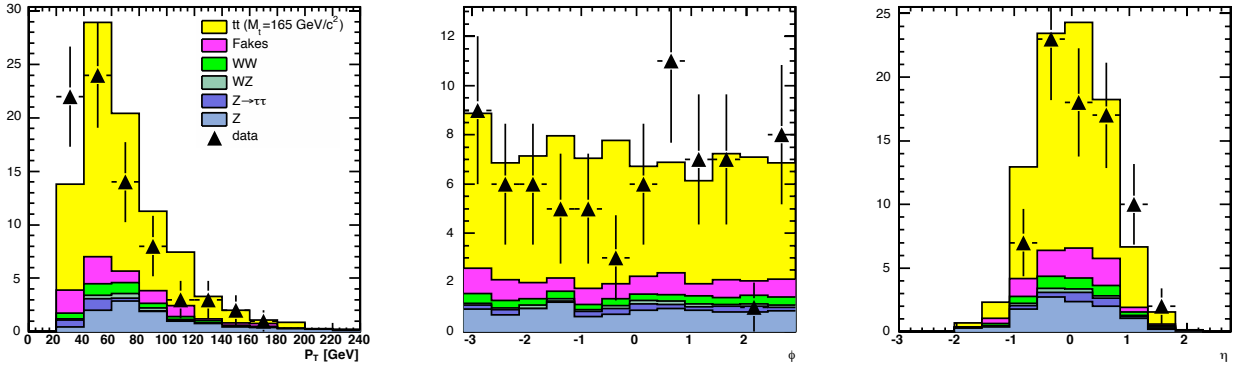

Figure A.4: Transverse momentum (P_T), azimuthal angle (ϕ) and pseudo-rapidity (η) of the leading lepton.
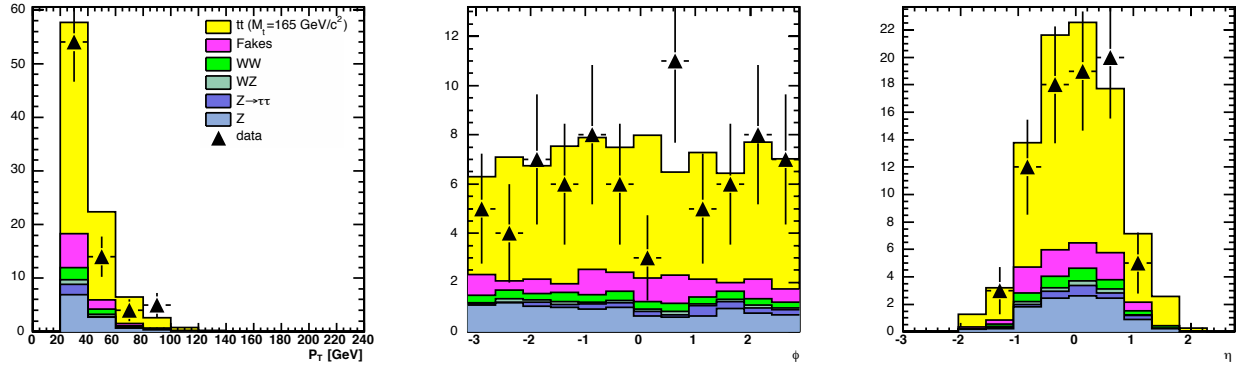
Figure A.5: Transverse momentum (P_T), azimuthal angle (ϕ) and pseudo-rapidity (η) of the second lepton.
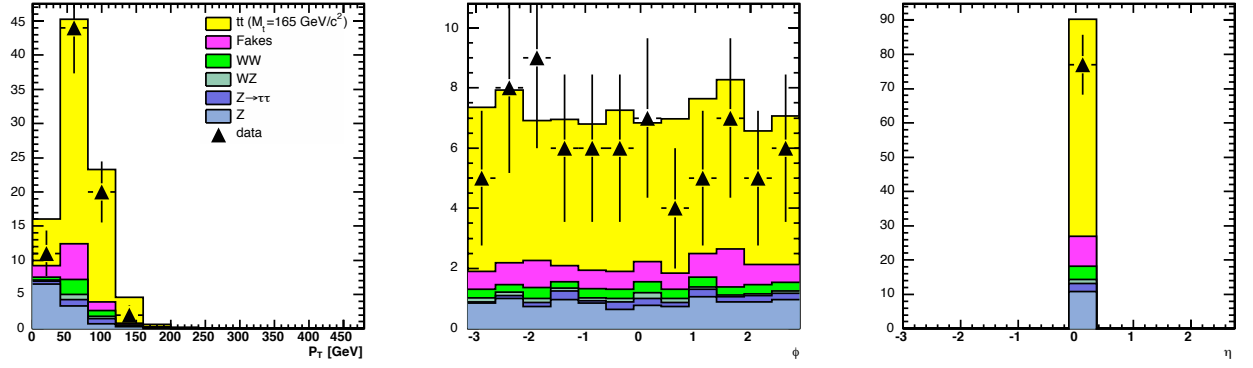

Figure A.6: Transverse momentum (P_T), azimuthal angle (ϕ) and pseudo-rapidity (η) of the missing transverse energy.
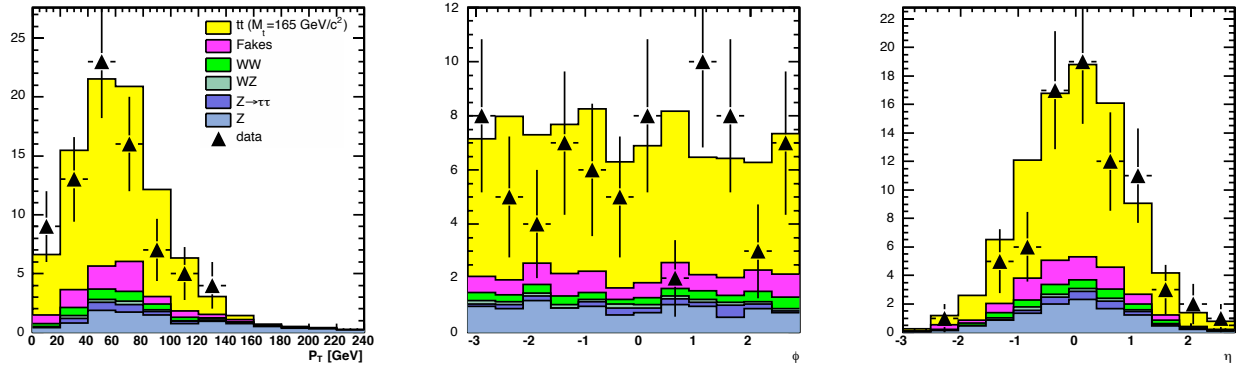

Figure A.7: Transverse momentum (P_T), azimuthal angle (ϕ) and pseudo-rapidity (η) of the vector sum of the leptons.
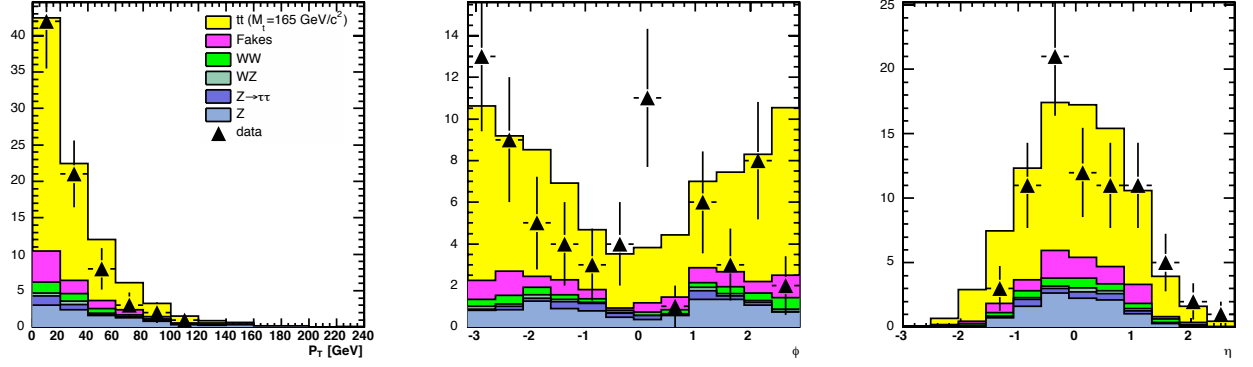
Figure A.8: Difference in transverse momentum (P_T), azimuthal angle (ϕ) and pseudo-rapidity (η) of the two leptons.
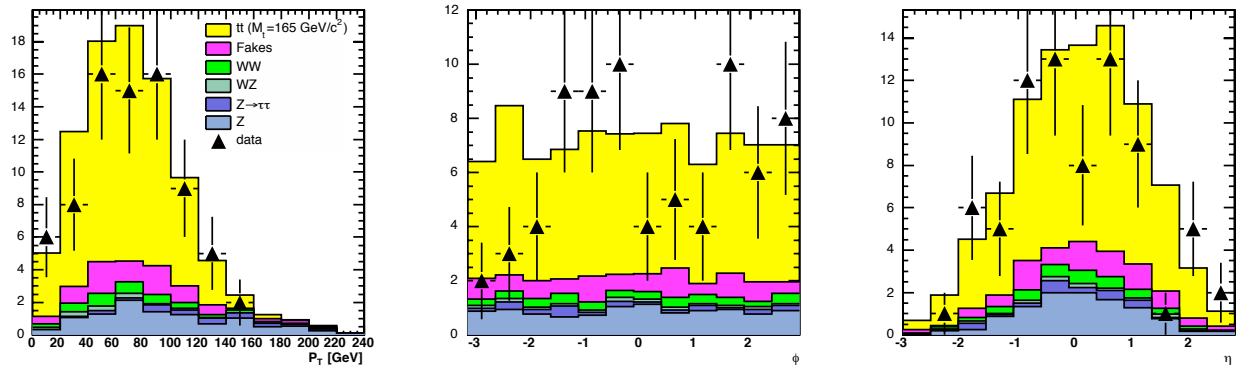

Figure A.9: Transverse momentum (P_T), azimuthal angle (ϕ) and pseudo-rapidity (η) of the vector sum of the jets.
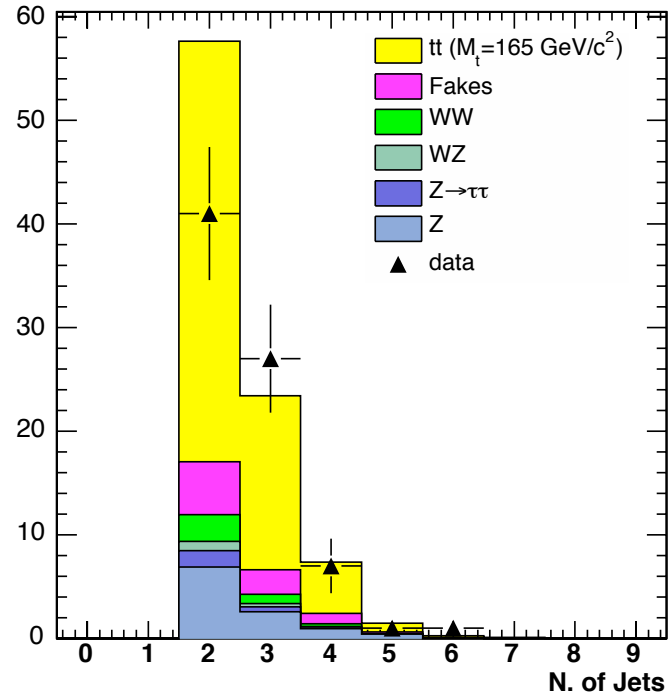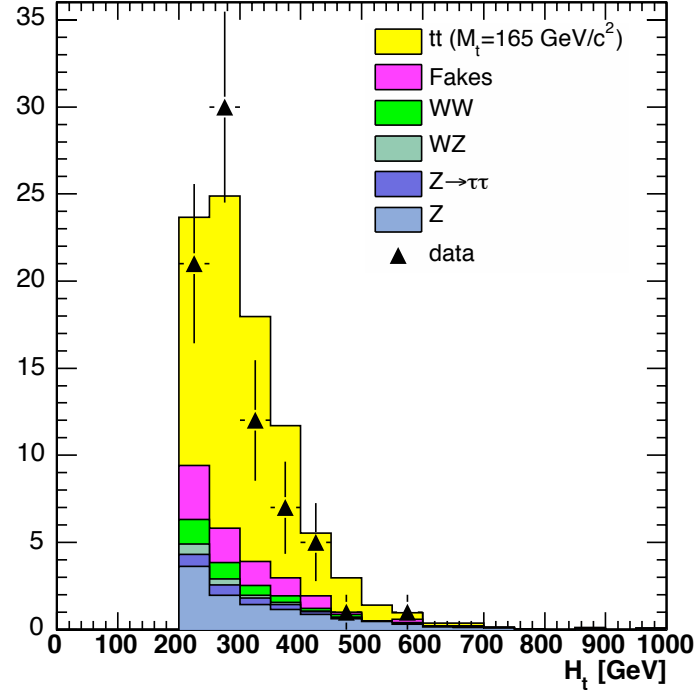
Figure A.10: Distribution of H_T and N_{jets}.
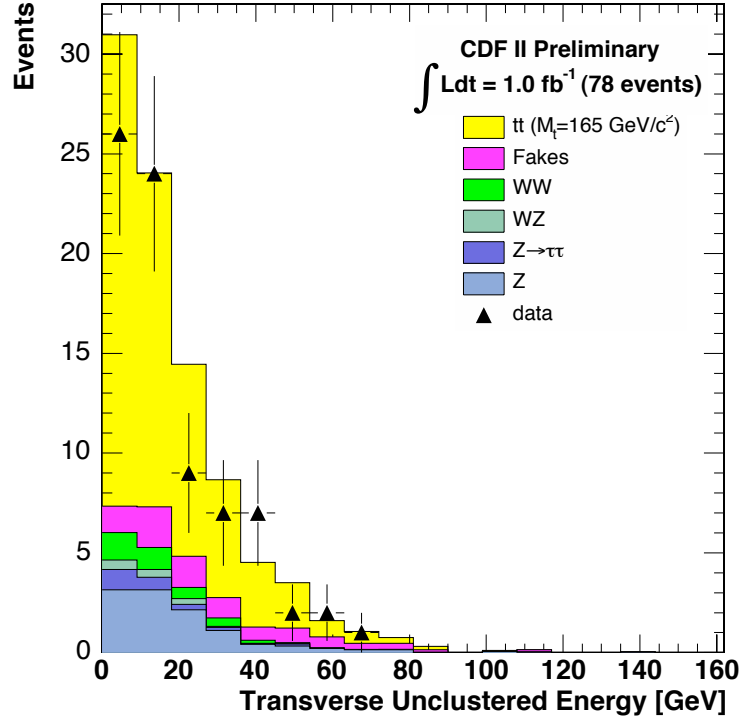
Figure A.11: Distribution of transverse unclustered energy.
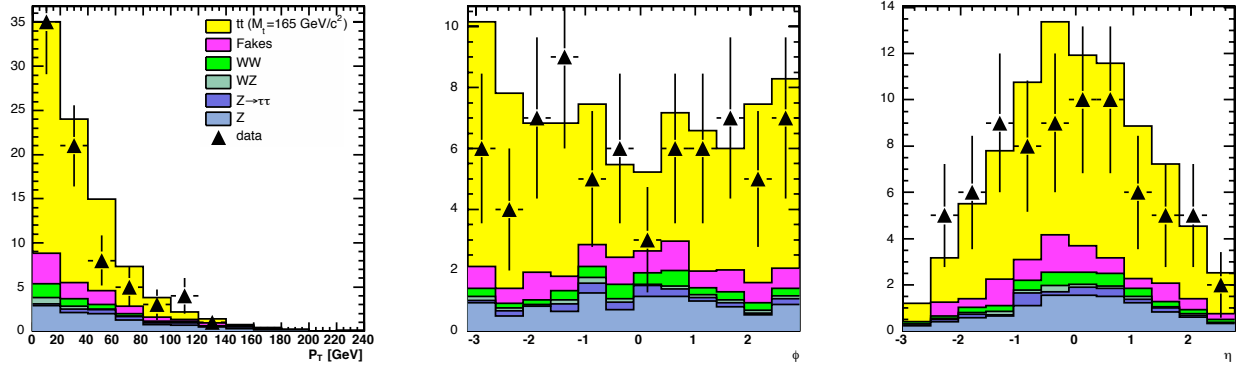
Figure A.12: Transverse momentum (P_T), azimuthal angle (ϕ) and pseudo-rapidity (η) of the difference between the leading jets.

Figure A.13: Transverse momentum (P_T), azimuthal angle (ϕ) and pseudo-rapidity (η) of the difference between the missing energy and the leading jet.

Figure A.14: Transverse momentum (P_T), azimuthal angle (ϕ) and pseudo-rapidity (η) of the vector sum of both jets and leptons.

BIBLIOGRAPHY

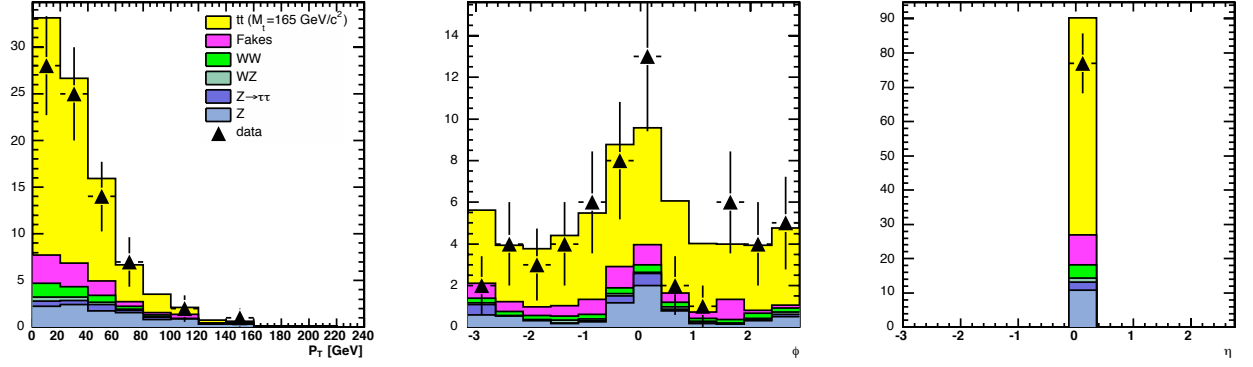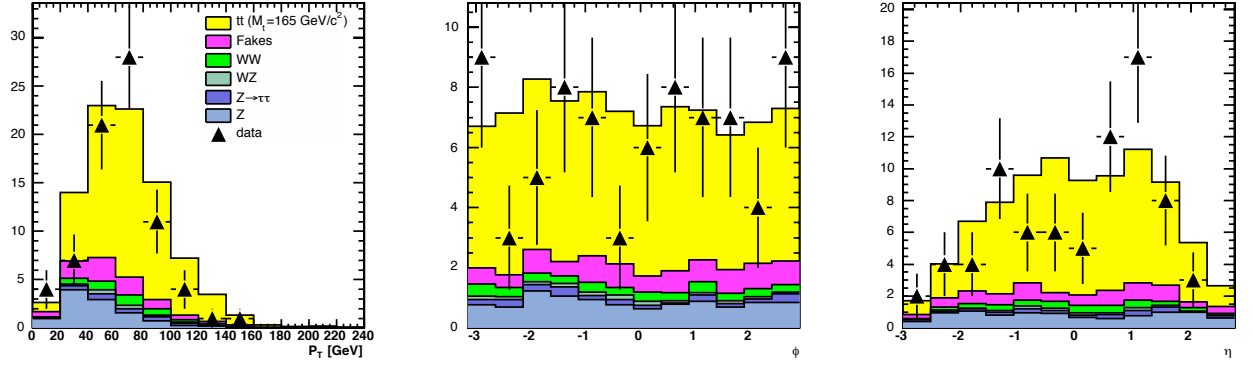[1] A. KOVALEV, *Measurement of the top quark mass at CDF II*, PhD thesis, University of Pennsylvania, 2005. 2

[2] A. ABULENCIA ET AL., *Top quark mass measurement from dilepton events at CDF II*, Phys. Rev. Lett., 96 (2006). 2, 100

[3] D. J. GROSS AND F. WILCZEK, *Asymptotically free gauge theories*, Phys. Rev., D8 (1973), p. 3633. 3

[4] H. D. POLITZER, *Asymptotic freedom: An approach to strong interactions*, Phys. Rept., 14 (1974), p. 129. 3

[5] S. L. GLASHOW, *Partial symmetries of weak interactions*, Nucl. Phys., 22 (1961). 3

[6] A. SALAM AND J. C. WARD, *Electromagnetic and weak interactions*, Phys. Lett., 13 (1964). 3

[7] S. WEINBERG, *A model of leptons*, Phys. Rev. Lett., 19 (1967), p. 1264. 3

[8] S. EIDELMAN ET AL., *Review of particle physics*, Physics Letters B, 592 (2004), p. 1. 4, 33

[9] P. W. HIGGS, *Broken symmetries and the masses of gauge bosons*, Phys. Rev. Lett., 13 (1964), p. 508. 4

[10] R. BARATE ET AL., *Search for the standard model Higgs boson at LEP*, Phys. Lett., B565 (2003), p. 61. 5

[11] THE LEP COLLABORATION, THE LEP ELECTROWEAK WORKING GROUP, THE SLD ELECTROWEAK AND HEAVY FLAVOR GROUPS, *A combination of preliminary electroweak measurements and constraints on the standard model*, Tech. Report CERN-PH-EP/2005-051, CERN, 2005. viii, 5, 6

[12] E. RICE ET AL., *Search for structure in $\sigma(e^+e^- \to hadrons)$ between $\sqrt{s} =10.34$ and 11.6 GeV*, Phys. Rev. Lett., 48 (1982), p. 906. 6

[13] F. ABE ET AL., *Observation of top quark production in $p\bar{p}$ collisions with the Collider Detector at Fermilab*, Phys. Rev. Lett., 74 (1995), p. 2626. 6

[14] S. ABACHI ET AL., *Observation of the top quark*, Phys. Rev. Lett., 74 (1995), p. 2632. 6

[15] M. CACCIARI ET AL., *The $t\bar{t}$ cross-section at 1.8 and 1.96 TeV: A study of the systematics due to parton densities and scale dependence*, J. High Energy Phys., 0404 (2004), p. 068. viii, xiii, 7, 8, 35, 37, 53, 74

[16] CDF COLLABORATION, *Combination of CDF top quark pair production cross section measurements up to 750 pb^{-1}*, Tech. Report CDF/PHYS/TOP/PUBLIC/8148, CDF Collaboration, 2006. viii, 7, 8

[17] M. KOBAYASHI AND T. MASKAWA, *CP violation in the renormalizable theory of weak interaction*, Prog. Theor. Phys., 49 (1973), p. 652. 7

[18] THE CDF COLLABORATION, THE DØ COLLABORATION AND TEVATRON ELECTROWEAK WORK-ING GROUP, *Combination of CDF and DØ results on the mass of the top quark*, Tech. Report FERMILAB-RM-2347-E, Fermilab, 2006. viii, 11, 12, 100

[19] F. ABE ET AL., *The CDF II detector: Technical design report*, Tech. Report FERMILAB-Pub-96/390-E, 1996. viii, 19, 22

[20] A. SILL ET AL., *SVX-II: CDF Run II silicon tracking projects*, Nucl. Instrum. Methods, A447 (2000), p. 1. 20

[21] C. S. HILL ET AL., *L00: Operational experience and performance of the CDF II silicon detector*, Nucl. Instrum. Methods, A530 (2004), p. 1. 21

[22] A. AFFOLDER ET AL., *ISL: Intermediate silicon layers detector for the CDF experiment*, Nucl. Instrum. Methods, A453 (2000), p. 84. 21

[23] T. AFFOLDER ET AL., *COT central outer tracker*, Nucl. Instrum. Methods, A526 (2004), p. 249. 22

[24] L. BALKA ET AL., *The CDF central electromagnetic calorimeter*, Nucl. Instrum. Methods, A267 (1988), p. 272. 24

[25] S. BERTOLUCCI ET AL., *The CDF central and endwall hadronic calorimeters*, Nucl. Instrum. Methods, A267 (1988), p. 301. 24

[26] M. ALBROW ET AL., *The CDF plug upgrade electromagnetic calorimeter: Test beam result*, Nucl. Instrum. Methods, A480 (2002), p. 524. 24

[27] G. APOLLINARI ET AL., *Shower maximum detector for the CDF plug upgrade calorimeter*, Nucl. Instrum. Methods, A412 (1998), p. 515. 24

[28] G. ASCOLI ET AL., *The CDF central muon detector*, Nucl. Instrum. Methods, A268 (1988), p. 33. 25

[29] D. ACOSTA ET AL., *Measurement of the $t\bar{t}$ production cross section in $p\bar{p}$ collisions at $\sqrt{s}$ = 1.96 TeV using dilepton events*, Phys. Rev. Lett., 93 (2004), p. 142001. 29

[30] ——, *Measurement of the forward-backward charge asymmetry from $W \rightarrow e\nu$ production in $p\bar{p}$ collisions at $\sqrt{s}$=1.96 TeV*, Phys. Rev. D, 71 (2005), p. 051104. 30

[31] F. ABE ET AL., *Topology of three-jet events in $p\bar{p}$ collisions at $\sqrt{s}$ = 1.8 TeV*, Phys. Rev. D, 45 (1992), p. 1448. 31

[32] A. BHATTI ET AL., *Determination of the jet energy scale at the Collider Detector at Fermilab*, Nucl. Instrum. Methods, A (To be published). 32

[33] T. SJOSTRAND ET AL., *High-energy-physics event generation with PYTHIA 6.1*, Computer Phys. Commun., 135 (2001), p. 238. ix, 32

[34] G. CORCELLA ET AL., *HERWIG 6: an event generator for hadron emission reactions with interfering gluons*, J. High Energy Phys., 01 (2001), p. 010. ix, 32, 36, 37

[35] M. L. MANGANO ET AL., *ALPGEN, a generator for hard multiparton processes in hadronic collisions*, J. High Energy Phys., 0307 (2003), p. 001. 35

[36] F. ABE ET AL., *Measurement of the top quark mass with the Collider Detector at Fermilab*, Phys. Rev. Lett., 82 (1999), p. 271. 38

[37] B. Abbot et al., *Measurement of the top quark mass using dilepton events*, Phys. Rev. Lett., 80 (1998), p. 2063. 38

[38] K. Kondo, *Dynamical likelihood method for reconstruction of events with missing momentum. I. Method and toy models*, J. Phys. Soc. Jpn., 57 (1988), p. 4126. 38

[39] G. Goldstein et al., *Observing top-quark production at the Fermilab Tevatron*, Phys. Rev. D, 47 (1993), p. 967. 38

[40] V. Abazov et al., *A precision measurement of the mass of the top quark*, Nature, 429 (2004), p. 638. 39

[41] F. Canelli, *Helicity of W bosons in single lepton $t\bar{t}$ events*, PhD thesis, University of Rochester, 2003. 39, 44

[42] J. Estrada, *Maximal Use of Kinematic Information for the Extraction of the Mass of the Top Quark in Single-Lepton $t\bar{t}$ events at DØ*, PhD thesis, University of Rochester, 2001. 39

[43] J. Pumplin et al., *New generation of parton distributions with uncertainties from global QCD analysis*, J. High Energy Phys., 007 (2002), p. 012. 40, 84

[44] G. Mahlon and S. Parke, *Maximizing spin correlations in top quark pair production at the Tevatron*, Phys. Lett. B, 411 (1997), p. 173. 52

[45] ———, *Improved spin basis for angular correlation studies in single top quark production at the Fermilab Tevatron*, Phys. Rev. D, 55 (1997), p. 7249. 52

[46] K. G. Chetyrkin et al., *Second order QCD corrections to $\Gamma(t \rightarrow Wb)$*, Phys. Rev. D, 60 (1999). 53

[47] C. Sturm, *Mémoire sur la résolution des équations numériques*, Bull. Sci. Math. Ferussac, 2 (1829), p. 419. 55

[48] G. P. Lepage, *A new algorithm for adaptive multidimensional integration*, Journal of Computational Physics, 27 (1978), p. 192. 58

[49] M. Galassi et al., *GNU Scientific Library Reference Manual (2nd Ed.)*, Network Theory Ltd., 2004. 58

[50] A. Pukhov et al., *CompHEP – a package for evaluation of Feynman diagrams and integration over multi-particle phase space*, Tech. Report INP MSU 98-41/542, Moscow State University, 1999. 64

[51] F. Maltoni and T. Stelzer, *Madevent: Automatic event generation with MadGraph*, J. High Energy Phys., 0302 (2003). 64

[52] A. Abulencia et al., *Top quark mass measurement using the template method in the lepton+jets channel at CDF*, Phys. Rev. D, 73 (2006), p. 32003. 82, 85

[53] A. D. Martin et al., *The α_s dependence of parton distributions*, Phys. Lett. B, 356 (1995), p. 89. 85

[54] A. Abulencia et al., *Measurement of the top quark mass using template methods on dilepton events in $p\bar{p}$ collisions at $\sqrt{s}=1.96$ TeV*, Phys. Rev. D, 73 (2006), p. 112006. 100

[55] CDF Collaboration, *Measurement of the top quark mass using the template method in the lepton plus jets channel with in situ $W \rightarrow jj$ calibration at CDF II*, Tech. Report CDF/PHYS/TOP/PUBLIC/8125, CDF Collaboration, 2006. 100

[56] ——, *Measurement of the top quark mass using the matrix element analysis technique in the lepton plus jets channel with in situ $W \to jj$ calibration*, Tech. Report CDF/PHYS/TOP/PUBLIC/8375, CDF Collaboration, 2006.   101

[57] D. Acosta et al., *Measurement of the $t\bar{t}$ production cross section in p[overline p] collisions at $\sqrt{s} = 1.96$ TeV using lepton + jets events with secondary vertex b -tagging*, Phys. Rev. D, 71 (2005), p. 052003.   101

[58] CDF Collaboration, *Measurement of the top quark mass using a matrix element method in a b-tagged sample*, Tech. Report CDF/PHYS/TOP/PUBLIC/8401, CDF Collaboration, 2006.   101

[59] The CDF Collaboration, The DØ Collaboration and Tevatron Electroweak Working Group, *Combination of CDF and DØ results on the mass of the top quark*, Tech. Report FERMILAB-RM-2355-E, Fermilab, 2006.   101

[60] LEP Electroweak Working Group, *http://lepewwg.web.cern.ch/LEPEWWG/*, 2006.   101